

FOG

Freiberg Online Geology

FOG is an electronic journal registered under ISSN 1434-7512



2011, VOL 30



Christin Müller

Department of Hydrogeology, Technische Universität Bergakademie Freiberg,
Gustav-Zeuner Str.12, 09599 Freiberg, Germany.
E-Mail: christin.mueller5@googlemail.com

Geothermal state of shallow submarine geothermal systems and isotopic signatures of Panarea, Aeolian Islands (Italy)

141 pages, 45 figures, 39 tables, 168 references

Acknowledgement

First of all, I want to thank my supervisors Prof. Broder Merkel, Dipl.-Ing. Gerald Barth, Dr. Francesco Italiano and Dipl.-Geoökol. Mandy Schipek for their great support during the preparation and the realization of the field investigations. Additionally, a special gratitude for all discussions and the invaluable feedback concerning the experimental work and also during the writing process.

Many thanks are addressed to Dr. Francesco Italiano and his colleagues Dr. Fausto Grassa, Marcello Liotta, Mauro Martelli, Mariano Tantillo, Nicola Romeo, Dr. Andrea Luca Rizzo and Dr. Fabio Vita for the kind and exciting mentoring during my stay at the Istituto Nazionale di Geofisica e Vulcanologia in Palermo. They really took care of me over the entire duration stay in Sicily and I felt very welcome. It was a great pleasure to participate in the field trip to Vulcano Island and the workshop after my laboratory analysis in Milazzo.

Furthermore, I thank Dr. Kay Knöller and Dr. Stephan Weise as well as the laboratory team with Petra Blümel, Sandra Zuecker-Gerstner, Wolfgang Städter and Martina Neuber for the realization of stable isotope analysis at the Helmholtz-Centre for Environmental Research in Halle / Saale. Thanks a lot for the very helpful discussions after my laboratory experiments.

I am grateful to Dr. N.-A. Kummer and Dipl.-Chem. H.-J. Peter for the competent help and support during my water and gas analysis in the laboratory of the Hydrogeology Section, TU Bergakademie Freiberg.

A very big thanks to the whole team of scientific diving at the TU Bergakademie Freiberg without their excellent assistance underwater and above, the collective preparation, the close cooperation and the rich conversations this project would not have been possible.

Finally, I want to thank Andreas Wahl for building the measuring sensors, Dr. Richard Gloaguen for his useful advices and ideas and also Katharina Hanetzog and Sandra Urbanik for inspiring dialogues.

Last but not least my deepest gratitude goes to my family and friends; especially, Sascha Russig, Ariane Schön and Judith Schreckenbach for continual support, motivation and encouragement.

TABLE OF CONTENTS

List of Figures.....	III
List of Tables.....	VII
Symbols and Abbreviations.....	IX
Abstract.....	XI
Zusammenfassung.....	XII
1 INTRODUCTION.....	1
1.1 Preamble.....	1
1.2 Objectives.....	3
1.3 State of research.....	4
1.3.1 Geothermal energy from the earth.....	4
1.3.2 Isotopic analysis.....	6
2 DESCRIPTION OF THE INVESTIGATION AREA.....	7
2.1 Geological and hydrothermal settings of Panarea.....	7
2.2 Maps of the investigation area.....	11
3 METHODOLOGY.....	16
3.1 Thermodynamic measurements.....	16
3.1.1 Heat flux.....	16
3.1.2 Temperature gradient.....	18
3.1.3 Thermal conductivity.....	20
3.1.4 Calibration of the sensors.....	22
3.2 Sampling Procedures.....	24
3.2.1 Water and gas sampling.....	24
3.2.2 Preparation and storage of the samples.....	27
3.3 On-site parameters.....	28
3.4 Laboratory analyses.....	31
3.4.1 Composition of the fluids.....	31
3.4.1.1 Ion chromatography (IC).....	31
3.4.1.2 Inductively Coupled Plasma - Mass Spectrometry (ICP-MS).....	32
3.4.1.3 Total inorganic carbon (TIC) / Alkalinity.....	32
3.4.2 Gas composition with gas chromatography.....	33
3.5 Isotopic Analyses.....	34
3.5.1 Isotopic composition of the fluids.....	34
3.5.1.1 Hydrogen and oxygen isotopic composition.....	34
3.5.1.2 Carbon isotopic composition.....	37
3.5.2 Isotopic composition of the gas.....	38
3.5.2.1 Carbon isotopic composition.....	38
3.5.2.2 Noble isotopic composition: helium, neon and argon.....	38
3.5.3 Sulfur isotopes in water and gas.....	42

4	RESULTS AND EVALUATION	43
4.1	Thermodynamic parameters	43
4.1.1	Heat flux.....	43
4.1.2	Temperature gradient	52
4.1.3	Thermal conductivity	57
4.1.4	Calibration of the sensors.....	61
4.2	Water and gas analyses.....	64
4.2.1	Chemical composition of the fluids	64
4.2.1.1	<i>On-site parameters.....</i>	<i>64</i>
4.2.1.2	<i>Main cations and anions (IC).....</i>	<i>66</i>
4.2.2	Chemical composition of the gas.....	70
4.2.3	Isotopic composition of the fluids	71
4.2.3.1	<i>Hydrogen and oxygen isotopic composition</i>	<i>71</i>
4.2.3.2	<i>Carbon isotopic composition.....</i>	<i>83</i>
4.2.4	Isotopic composition of the gas.....	87
4.2.4.1	<i>Carbon isotopic composition.....</i>	<i>87</i>
4.2.4.2	<i>Noble isotopic composition: helium, neon, argon.....</i>	<i>88</i>
4.2.5	Sulphur isotopes in fluids and gas	92
5	FINAL DISCUSSION AND CONCLUSION	96
	REFERENCES	99
	APPENDIX	113

List of Figures

- Figure 1-1: Map of the Southern Tyrrhenian Sea and Aeolian Islands. It illustrates the structural faults system in this area (TL: Tindari–Letojanni fault system, SA: Sisifo–Alicudi fault system; further information, Chapter 2.1) and also the chronology and location of eruptions and earthquakes that occurred in 2002 (Esposito et al., 2006). 2
- Figure 2-1: Simplified bathymetric chart which shows the location of Panarea islets, the occurring fumarolic fields and Fe-rich mineralization as well as the submerged emission vents. Additionally, the inferred crater rim and the location of the main gas emission in 2002 are shown. (Chiodini et al., 2006) 8
- Figure 2-2: Structural sketch of the Aeolian area and chronological evolution of the volcanism, fumaroles or seismic activity. The geochronological information characterizes the volcanic rocks from the subaerial (Is.) and submarine (Sub.) parts of the islands as well as seamounts (Smt.). Sources of these data are: Barberi et al. (1994), Beccaluva et al. (1982, 1985), Calanchi et al. (1995, 2002), Continisio et al. (1997), Crisci et al. (1991), De Astis et al. (1997a, 1997b), De Luca et al. (1997); Finetti and Del Ben (1986); Gillot (1987), Hornig-Kjarsgaard et al. (1993), Lanzafame and Bousquet (1997); Keller (1980), Manetti et al. (1995), Marani and Trua (2002), Pichler (1980), Santo and Clark (1994), Soloviev et al. (1990) (modified after Müller, 2011). 10
- Figure 2-3: Map in the below right shows the investigated sites (triangles) in the hydrothermal system east of Panarea Island. The shallow submarine area is surrounded by the islets of Dattilo, Panarelli, Lisca Bianca, Bottaro and Lisca Nera (Steinbrückner, 2009). In the colored map made with the MapSource® program the measured shifted diving locations are shown. The inaccuracy can be determined by the fixed point “Leuchtfueer”. The measured and the true location are charted in the map (red line). 14
- Figure 2-4: Bathymetric map showing the investigation area and the surrounding field to a water depth of 120 meters (blue). The diving spots are located between the islands Dattilo and Lisca Bianca in a water depth up to 30 meters. A detailed map is shown in top right. The numbers, the associated coordinates (in UTM WGS84, Zone 33S) and names of the dive locations are described in the table aside. 15
- Figure 3-1: Top: Necessary equipments for heat flux measurements including the measurement instrument from Ahlborn, AHLMEMO® 2590-3S; Bottom: Measurement instrument at the sea floor, “Point 26” 17
- Figure 3-2: Scheme of the temperature gradient sensor with four integrated thermo couples18
- Figure 3-3: Top: Temperature gradient sensor with water proof housed PCE T-390; Bottom: Temperature gradient sensor with PCE T-390 at the sea floor, “Area 26” 19
- Figure 3-4: Scheme of the thermal conductivity sensor 20
- Figure 3-5: Top: Necessary instruments for thermal conductivity measurements; Bottom: Thermal conductivity sensor at the sea floor, “Area 26” 21
- Figure 3-6: Experiment to calibrate the temperature gradient sensor in a cylinder filled with water (left) and sand (right). The sensor was recessed into the cylinders and the temperature progression was documented with the temperature logger PCE T-390... 23
- Figure 3-7: Experiment to calibrate the thermal conductivity sensor in saturated sand. Power supply ensured by a device from Statron GmbH (32 V / 16 A, type 3233.1). Temperature measurement with GMH 3350 (Greisinger electronic GmbH). 24

- Figure 3-8: Left: Instruments for water sampling. Not shown: three way valve and metal funnel; Right: Instruments for gas sampling. Two gas sampling tubes: from TUBAF with a septum (tube left) and from INGV without a septum (tube right). 26
- Figure 3-9: Gas sampling at a gas vent (fumarole) with a gas sampling tube and a metal funnel26
- Figure 3-10: High temperature vacuum-distillation apparatus with the marked used valves (red crosses) 36
- Figure 3-11: Top: Pre-cleaning steps for helium and neon isotope measurements. Bottom: Mass spectrometer Helix MCT and the detectors to register noble gas isotopes..... 40
- Figure 3-12: Pre-cleaning step of argon isotopes from other gases. 41
- Figure 3-13: Kjeldahl distillation procedure: On the left AVS, on the right CRS with Chrom III.42
- Figure 4-1: Schematic visualization of the regions where heat fluxes can be calculated based on measured temperature gradients, water and sediment surface temperatures. Temperature curves indicate the progression considering heat transfer caused by conduction and conduction/convection. Convection can be generated by hot water... 44
- Figure 4-2: Method to calculate the sediment surface temperature based on the temperature gradient measurements (here, "La Calcara"). Therefore a linear regression was conducted (example, no. 6). The blue-coloured trend line regards temperatures from all four thermo couples and results in a sediment surface temperature of 38.6 °C. The orange trend line attends the upper three thermo couples and causes a sediment surface temperature of 67.6 °C..... 48
- Figure 4-3: Heat flux measurements, "Area 26" 50
- Figure 4-4: Heat flux measurements, "La Calcara". Errors in measurement for breakpoint 'Flat field, no Posidonia, hematite deposition, cool water' (blue line). It is thermodynamically not possible to gauge negative heat fluxes because it is not possible to transport heat from cold to hot places (second law of thermodynamics)..... 51
- Figure 4-5: Measurement with the temperature gradient sensor in "Area 26". It shows that after a time period of app. 300 sec constant temperatures in all four thermo couples are achieved that typify the real temperature in the different sediment depths.52
- Figure 4-6: Temperature gradients at location „La Calcara” with the associated measured heat fluxes in W/m^2 54
- Figure 4-7: Temperature gradients at location "Area 26" with the associated measured heat fluxes in W/m^2 (Boiling point water at corresponding water pressure (~26 m) app. 140°C)55
- Figure 4-8: Top: Measurements with the thermal conductivity sensor made in "Bottaro West" (06.09.2010) and "Area 26" (07.09.2011). Bottom: Corresponding Ln(time)-temperature-diagram, shows the heating phase and the equation of the added trend line. Slope of the trend line is important to solve the equation [4.9] and to get the thermal conductivity. 58
- Figure 4-9: Calibration of the temperature gradient sensor to the temperature equilibrium in heated water (53 °C, top and 73 °C, bottom). Temperature equilibrium was achieved from all four TCs after a time period of app. 150 sec..... 61
- Figure 4-10: Results of the laboratory experiment to measure the temperature adjustment to the surrounding area for different temperatures (50 °C and 60 °C) during constant voltages and amperages. After a time period of 150 sec for 50 °C and 180 sec for 60 °C,

the temperature of the surrounded sand was in equilibrium (marked with dotted lines).	62
Figure 4-11: E_H/pH -diagram with upper and lower stability limits of water. Values of the samples compared to conditions of euxinic seawater, normal seawater and saline water (after Hölting & Coldeway, 2005).....	65
Figure 4-12: Contents of anions for each diving location from IC determinations at INGV and TUBAF including the calculated standard error.	67
Figure 4-13: Comparison of anions in samples from different diving location with standard concentrations of seawater after Brown et al. (1995).....	68
Figure 4-14: Absolute concentration of cations in water samples for each diving location. The mean values are plotted with the corresponding standard deviation.	68
Figure 4-15: Differences of sampling points minus standard concentrations of seawater after Brown et al. (1995).	69
Figure 4-16: Detailed visualization of the $\delta D/\delta^{18}O$ composition in sampled water from 2007, 2008 and 2010 which were analyzed at the UFZ and INGV. It illustrates the isotopic signature for each diving location as well as a comparison of 15 measurements between the labs (bigger plotted measuring values, highlighted in the legend). All UFZ measurement points are marked with a black border whereby the INGV reading points are not bordered.	74
Figure 4-17: Isotopic composition $\delta D/\delta^{18}O$ of sampled water in 2007, 2008 and 2010 which were analyzed in two laboratories (UFZ and INGV). Additionally, several interpretations of possible water sources based on measurements of fumarolic streams from Vulcano Island (Deep component after Capasso et al. (1997), Magmatic and geothermal component after Bolognesi & D'Amore (1993), "Andesitic" magmatic water after Giggenbach (1992) & Chiodini et al. (1995)) as well as the local meteoric water (precipitation from western Sicily after Liotta et al., 2008) and the shifted value for Mediterranean Sea water after Grassa et al. (2006).	75
Figure 4-18: Accepted sections to calculate a 3-component-mixture. 6 measuring points are located outside of the triangle and can not be used for the evaluation (probes from "La Calcara" and "Bottaro West"). All the other points can be described by percentual proportions of each water source.....	76
Figure 4-19: Ternary triangular-plot displayed for all diving locations. Water from "La Calcara" and "Bottaro West" plot outside the triangle.	77
Figure 4-20: Comparison of (D/O) - measurements arranged at the INGV and UFZ by visualisation of measuring differences (Table 4-8). Diamond-shaped rhombic points are measurements arranged in 2008. The rectangular points are measurements derived from examinations in 2010/2011. The maximum shifts of $\Delta \delta D_{VSMOW}(UFZ-INGV)$ and $\Delta \delta^{18}O_{VSMOW}(UFZ-INGV)$ are 8.2 ‰ and (comparatively low) 1.5 ‰, respectively.	80
Figure 4-21: Water samples from 2008, 2009 and 2010 analyzed for $\delta^{13}C_{DIC}$ at the INGV and the UFZ. Mean values and standard deviation for each diving location is illustrated separately. The quantity of measurements is given in brackets in the legend. All Panarea samples and the corresponding values are saved in Table A 20. Reference isotopic compositions are plotted on the left side. Data are from Fornaseri (1984), Faure (1986), Hoefs (1987) Favara et al. (1999), Inguaggiato et al. (2000) and Favara & Inguaggiato (2000).	86
Figure 4-22: Isotopic composition $\delta^{34}S$ and $\delta^{18}O$ of sulphate in water samples.	93
Figure 4-23: Isotopic composition $\delta^{34}S$ of sulphite in gas and water samples collected in 2006, 2007, 2009 and 2010 analyzed at the UFZ. Each diving location is shown	

separately, number of samples is displayed in brackets. For the location “Bottaro North” an outlier is displayed which is not considered in the calculated mean value..... 94

List of Tables

Table 1-1: Measured and calculated heat fluxes mentioned in different previous publications.	4
Table 1-2: Natural occurring ratios of stable isotopes after Hoefs (1997) that are of interest within this thesis. Ratio of the noble gases are determined for helium (Jordan, 1979), neon (Dicken, 1995) and argon (Faure, 1986a).	6
Table 3-1: Preparation and storage of water samples for further chemical analyses.....	27
Table 3-2: Solid material precipitated from gas and solid samples for different stable isotopic analyses at the UFZ (for measurements in April 2011).	28
Table 3-3: Measuring range, precision and EDL of the measured ions.	30
Table 3-4: Isotopic composition of the used standard waters based on SMOW.	37
Table 4-1: Type of convection according to the heat transfer coefficient (α) and the corresponding calculated sediment surface temperatures with constant water temperature based on the model for "Convection on horizontal surfaces"	47
Table 4-2: Overview of the measured and calculated heat fluxes whereby conduction is calculated by the heat flux equation [4.1].	49
Table 4-3: Measured temperatures with temperature gradient sensor. In some measurements the sensor could not recess completely into the sediment whereby the first thermo couple was not in the sediment but measured the water temperatures. These temperatures are marked grey in the table. Temperature gradients which were used for further calculations (4.1.1) are highlighted bold.	56
Table 4-4: Calculation of the thermal conductivity with the use of equation [4.9] based on the field measurements. A constant voltage of 2.6 V and a constant amperage of 24.25 A was applied.	59
Table 4-6: Results of the gas chromatography analyses at the INGV in 2010. The grey shaded field samples were used for further argon isotope analyses.	70
Table 4-7: Used reference lines and potential water sources which are shown in Figure 4-16.	72
Table 4-8: Selected results of the isotopic composition D/O in water which were determined at the INGV and UFZ (samples from 2008 and 2010).	79
Table 4-9: Results of the analyzed gas samples for stable isotopes ($\delta^{13}\text{C}_{\text{CH}_4}$, $\delta^{13}\text{C}_{\text{CO}_2}$, $\delta^{13}\text{C}_{\text{DIC}}$) at the INGV and UFZ in 2010 and 2011.	87
Table 4-10: Data on isotopic composition from helium and neon of collected gas samples. Highlighted samples show no typical thermal R/R _a values whereby a contamination with atmospheric air can be assumed (not attend in summary).	89
Table 4-11: Data on chemical and isotopic composition from argon of gas samples. Highlighted sample shows a contamination with atmospheric air.	89
Table 4-12: Important noble isotopic signatures in different reservoirs (SLCM - Subcontinental Lithospheric Mantle, OIB – Ocean Island Basalts) which are of interest for this thesis. The ratios are declared after ^a Clark et al. (1976), ^b Mamyrin & Tolstikhin (1984), ^c Allègre et al. (1987, 1995), ^d Gautheron & Moreira (2002), ^e Breddam & Kurz (2001), ^f Ozima & Podosek (2002), ^g Marty & Humbert (1997), ^h Dunai & Baur (1995), ⁱ Trieloff et al. (2000).	90
Table 4-13: Calculated mean values and standard deviations for each diving location. Corresponding samples were collected from 2006 to 2011. The number of probes is displayed in brackets.	93
Table 4-14: Measured bacteria mats for sulphur isotopes.	95

Symbols and Abbreviations

AD	-	Anno Domini
ANOVA	-	Analysis of variance
app.	-	Approximately
AVS	-	Acid volatile sulphur
CM	-	Christin Mueller (sampler)
Conc.	-	Concentration
CRDS	-	Cavity Ring-Down Spectroscopy
CRS	-	Chromium reducible sulphur
degC	-	Degree Celsius
DIC	-	Dissolved inorganic carbon
DSS	-	Deep seismic sounding
EC	-	Electrical conductivity [mS/cm]
EDL	-	Estimated detection limit
E_h	-	Redox potential [mV] (at 25 °C, referred to standard potential)
FID	-	Flame Ionization Detector
GIS	-	Geographic information system
GPS	-	Geographical positioning system
GRT	-	Geothermal Response Test
GST	-	Gas sampling tubes
HWL	-	Hot Wire Detector
IAEA	-	International Atomic Energy Agency
IC	-	Ion chromatography
ICP-MS	-	Inductive coupled plasma mass spectrometry
ICP-OES	-	Inductive coupled plasma optical emission spectrometry
IHFC	-	International Heat Flow Commission
INGV	-	Istituto Nazionale di Geofisica e Vulcanologia in Palermo
IRMS	-	Isotope-ratio mass spectrometer
ISE	-	Ion-sensitive electrode
IWTT	-	Institute for Thermal Engineering and Thermodynamics
K	-	Kelvin
L	-	Litre
Ln	-	Natural logarithm
LMWL	-	Local Meteoric Water Line
M	-	Molar
MMWL	-	Mediterranean Meteoric Water Line
ml	-	Millilitre
Mol-%	-	Mole fraction
MORB	-	Mid Ocean Ridge Basalts
MS	-	Mandy Schipek (sampler)
MSC	-	Messinian salinity crisis
μ l	-	Microlitre
mV	-	Millivolt
MWL	-	Meteoric water line
n	-	Sample size
n.d.	-	Not determined

OIB	-	Ocean Island basalts
PDB	-	Pee Dee Belemnite
ppm	-	Parts per million
ppb	-	Parts per billion
prep.	-	Preparation
QGIS	-	QuantumGIS
RFA	-	X-ray fluorescence
Sec	-	Second
SLCM	-	Subcontinental lithospheric mantle
SHEMAT	-	Simulator for Heat and Mass Transport
STDEV	-	Standard diversity
T	-	Temperature [°C]
TC	-	Thermo couple
TDIC	-	Total dissolved inorganic carbon
TCD	-	Thermal Conductivity Detector
TIC	-	Total inorganic carbon
TUBAF	-	Technische Universität Bergakademie Freiberg
UFZ	-	Helmholtz-Centre for Environmental Research in Halle / Saale
vtk	-	Visualization Toolkit
vs.	-	Versus
VSMOW	-	Vienna Standard Mean Ocean Water
WISTAU	-	Scientific diving group of the TUBAF
WLD	-	Heat Conductivity Detector
wt%	-	Percent by weight
WMWL	-	World Meteoric Water Line

Nomenclature of samples:

PAN	-	Panarea
BP	-	Black Point
HL	-	Hot Lake
P21	-	Point 21
A26	-	Area 26
A26N	-	Area26 North
BW	-	Bottaro West
BN	-	Bottaro North
HL(FumF) / FumF	-	Fumarolic Field

Abstract

Investigation of the geothermal state of the submarine, volcanic active, hydrothermal system east of Panarea Island (Aeolian Islands, southern Italy) was conducted in September 2010. Seven diving locations (“Bottaro North”, “Bottaro West”, “Point 21”, “Area 26”, “Black Point”, “Hot Lake” associated with the “Fumarolic Field” and “La Calcara”) are located in water depths between 8 and 30 meters sheltering submarine gas vents (fumaroles) and hot water exhalations which were analysed by scuba diving. Measurements of the temperature gradient, the thermal conductivity and the heat flux were proceeded on the soft sediment seafloor with modified and new custom-made measuring equipment. The second part of this work was the accomplishment of several geochemical (on-site parameters, photometry, IC, ICP-MS, TIC and GC) and isotopic analysis on collected water and gas samples. Thereby stable isotopes ($\delta^2\text{H}$, $\delta^{18}\text{O}$, $\delta^{13}\text{C}$, $\delta^{34}\text{S}$) and instable isotopes (He, Ne, Ar) were determined. Isotopic measurements were performed in different laboratories: the Istituto Nazionale di Geofisica e Vulcanologia (INGV) in Palermo and the Helmholtz-Centre for Environmental Research (UFZ) in Halle / Saale.

“Hot spots” with temperatures of more than 135 °C (“La Calcara”) were detected in a sediment depth of just 470 mm. Most of them were connected with upcoming hydrothermal water and gas. “Cool spots” with temperatures of around 21 °C (normal seawater temperature) were located close-by. Heat fluxes of more than 2500 W/m² were measured. To get reproducible data, careful work (avoiding currents caused by the motion of fins, for example) was necessary. Additionally, the measuring instruments needed sufficient time to adapt to the natural occurring conditions.

Apart from the thermodynamic characteristics, the diving location “La Calcara” is exciting for isotopic analysis. Heavy $\delta^{13}\text{C}$ values were recorded in water samples (20 ‰). Samples from this diving spot show ($\delta^2\text{H}/\delta^{18}\text{O}$)-values which assume significant shares of magmatic water (around 30 %). Within this thesis it was verified that the isotopic signature of helium (R/Ra between 4.11 and 4.39) is an evidence of a mixed gas originating from the crust and the mantle.

Zusammenfassung

Die Untersuchung der geothermischen Situation des submarinen, vulkanisch aktiven Hydrothermalsystems östlich von Panarea (Aeolische Inseln, Italien) wurde im September 2010 durch das Scientific Diving Center der TU Bergakademie Freiberg durchgeführt. Dabei wurden 7 Tauchgebiete („Bottaro North“, „Bottaro West“, „Point 21“, „Area 26“, „Black Point“, „Hot Lake“ mit „Fumarolic Field“ und „La Calcara“) in Wassertiefen zwischen 8 und 30 m gerätetaucherisch näher untersucht. Messungen des Temperaturgradienten, der Wärmeleitfähigkeit und des Wärmeflusses auf weichem Sedimentuntergrund wurden mit Hilfe von modifizierten und selbst entwickelten Messsonden durchgeführt. Der zweite Teil der Arbeit betrachtet die Aufnahme verschiedener geochemischer Kenngrößen (Vorort-Parameter, Photometrie, IC, ICP-MS, TIC und GC) sowie die Analyse von Isotopen an gesammelten Gas- und Wasserproben. Es wurden sowohl stabile Isotope ($\delta^2\text{H}$, $\delta^{18}\text{O}$, $\delta^{13}\text{C}$, $\delta^{34}\text{S}$) als auch instabile Isotope (Helium, Argon, Neon) untersucht. Die Messungen erfolgten am Istituto Nazionale di Geofisica e Vulcanologia (INGV) in Palermo sowie am Helmholtz-Zentrum für Umweltforschung (UFZ) in Halle / Saale.

„Hot spots“ mit Temperaturen von mehr als 135 °C („La Calcara“) konnten in Sedimenttiefen von 47 mm ausgemacht werden, welche in der Regel mit Gas- und Wasseraustritten verbunden waren. In der Nähe jener heißen Stellen waren in gleicher Sedimenttiefe Temperaturen von nur 21 °C zu verzeichnen (entspricht Temperatur des Meerwassers). Wärmeflüsse von mehr als 2500 W/m² wurden detektiert. Um exakte Messwerte zu erhalten, ist Unterwasser sorgfältiges Arbeiten nötig (Einhalten von Messzeiten, Verhindern von Aufwirbelungen des umgebenden Wassers durch Taucher etc.).

Nicht nur thermodynamische Untersuchungen des neuen Tauchspots „La Calcara“, auch Isotopenanalysen zeigten interessante Ergebnisse. Es konnten hohe $\delta^{13}\text{C}$ Werte in Wasserproben nachgewiesen werden (20 ‰). Datierungen des (D/O)-Gehalts zeigen erhöhte Aneile an magmatischen Wässern (ca. 30 ‰). Die Untersuchungen des Migrationsverhaltens und der Herkunft von Gasen mit Hilfe von instabilen Isotopenbestimmungen zeigten eine Isotopensignatur des Heliums (R/Ra zwischen 4.11 und 4.39), welche auf eine Gasmischung aus Mantel und Kruste schließen lässt.

1 INTRODUCTION

1.1 Preamble

Panarea, one of the Aeolian Islands is located in the Southern Tyrrhenian Sea approximately 50 kilometers north of Sicily and part of an active volcanic area. The islands are formed by the subduction of the African plate below the European plate and belong to the back-arc volcanic system (Dando et al., 1999). The appearance of marine gas and hydrothermal fluids is characteristic for this region. These gases can be originated from the mantle and the subducted slab or from the decomposition of carbonates in marine sediments close to the surface (Dando et al., 1999).

Continuous gas venting in this region has been repeatedly interrupted by short terms of intense gas discharge, since historical times. These disruptions are anticipant due to new magmatic inputs into the geothermal reservoir (Caliro et al. (2004), Caracausi et al. (2005)). The most recent hydrothermal crisis occurred between the 2nd and 3rd November in 2002. A sudden and major increase in the emission of gas and hydrothermal fluids next to the islets Bottaro and Lisca Bianca happened about 2 kilometers east of Panarea (Caliro et al., 2004).

A whitish plume of suspended sediment was caused by the submarine explosion and extended for several hectares. Seismic swarms of low intensity (magnitudes of 1.8) were associated with the hydrothermal phenomenon and initiated gas outburst in five other areas around Panarea Island (Caliro et al. (2004), Caracausi et al. (2005), Esposito et al. (2006)).

The gas venting was not a single event. In September 6th 2002 an earthquake with a magnitude of 5.6 in the southern Tyrrhenian Sea approximately 50 km north-easterly of Palermo was registered. Additionally, there was a strong eruption of Mount Etna on October 27th 2002 (Esposito et al., 2006). On December 28th 2002, one month after the gas venting near Panarea, Stromboli erupted. Only 2 days later the north-western flank of Stromboli collapsed and generated two minor tsunamis on a regional scale. A mass movement was the outcome of these tsunamis (Tinti et al., 2005) and engendered some destruction on the surrounding islands including Panarea. Figure 1-1 shows a map of the Aeolian Islands which includes the chronology and locations of eruptions and earthquakes that occurred in 2002.

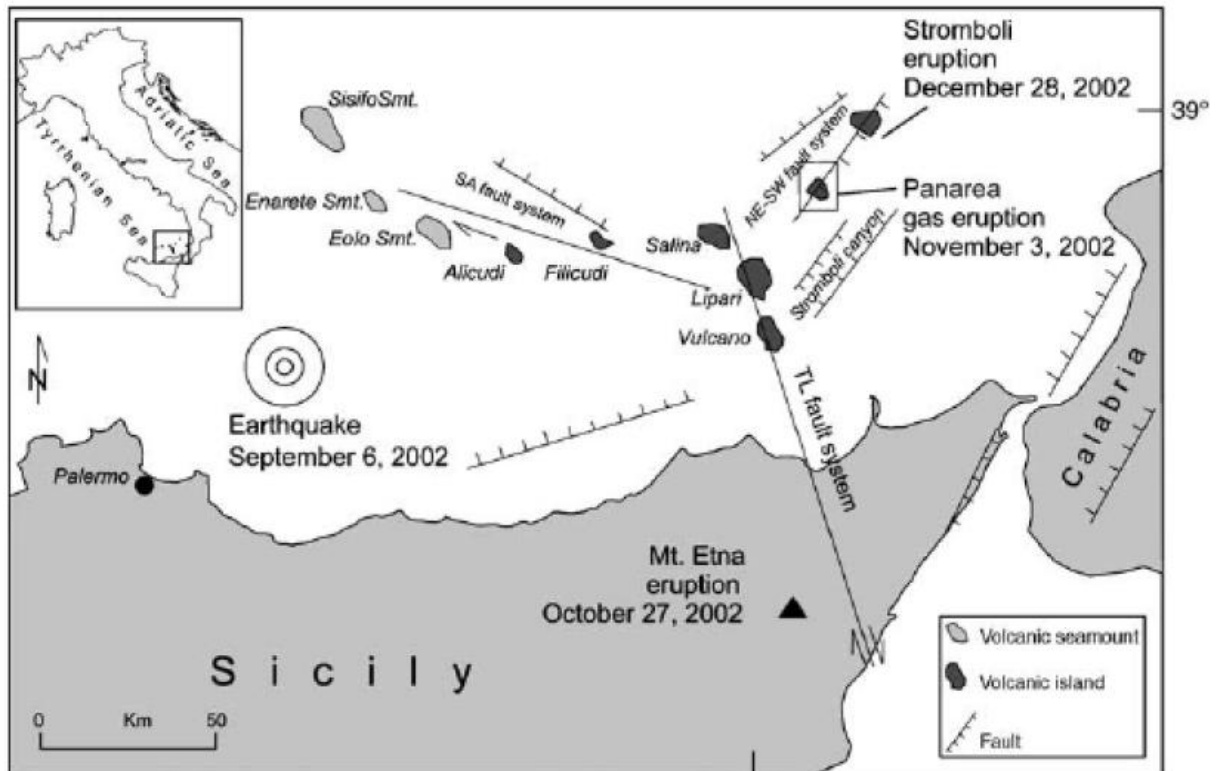


Figure 1-1: Map of the Southern Tyrrhenian Sea and Aeolian Islands. It illustrates the structural faults system in this area (TL: Tindari–Letojanni fault system, SA: Sisifo–Alicudi fault system; further information, Chapter 2.1) and also the chronology and location of eruptions and earthquakes that occurred in 2002 (Esposito et al., 2006).

The present-day gas emissions decreased to a state of low degassing compared to the situation in late 2002, but clearly remained higher than prior to the crises. The volcanic activity of Panarea before 2002 was distinguished by mild degassing of hydrothermal fluids. The isotopic signatures and chemical composition of gas samples from 2002 suggested that the gases originated from a hydrothermal or rather geothermal reservoir fed by magmatic fluids (Esposito et al., 2010). A model from Esposito et al. (2010) reveals that the intensity and distribution of the gases is strongly influenced by geophysical and geochemical variations within the system.

1.2 Objectives

The first aim of this thesis is the evaluation of a temperature gradient, thermal conductivity and heat flux measurements with the modified and new self-built measuring sensors. The second part is focused on the isotopic analysis of stable isotopes ($\delta^2\text{H}$, $\delta^{18}\text{O}$, $\delta^{13}\text{C}$, $\delta^{34}\text{S}_{\text{Sulphate}}$) in collected water samples. Stable isotopic composition were also determined in gas samples for $\delta^{13}\text{C}_{\text{CO}_2}$, $\delta^{34}\text{S}_{\text{H}_2\text{S}}$. Gas samples were additionally evaluated for instable isotopes like helium, neon and argon. Measurements were accomplished in two laboratories namely the INGV (in October 2010) and the UFZ (in April 2011). The institute in Italy is specialized in the determination of instable isotopes whereby the dispositions of sulfur and carbon isotopes were performed at the institute in Halle / Saale. Double measurements were arranged for hydrogen and oxygen isotopes. For the evaluation of the results, previous data has been used (Sieland, 2009). The analytical methods used for ($\delta^2\text{H}/\delta^{18}\text{O}$) - determination are different from each other. Therefore, a comparison of the measurements of both laboratories is expedient and part of the discussion.

1.3 State of research

1.3.1 Geothermal energy from the earth

From the interior of the earth, heat is transmitted to its surface mainly by three mechanisms: radiation, advection and conduction whereat conduction dominates in the earth's lithosphere (Clauser & Huenges, 1995). But there are exceptions. If the hydraulic permeability of crustal material is sufficiently high, convection can be an equally or even more efficient transfer mechanism (Etheridge et al. (1983), Torgersen (1990), Clauser (1992)). This is the case in sedimentary basins or in hydrothermal areas, for example.

Information about the geothermal budget can be gathered from boreholes. An expedition in August 2007 organized by the IGM-GEOMAR ("Shallow drilling of hydrothermal sites in the Tyrrhenian Sea" - PALINDRILL) collected cores to the depth of 5 m from the upper sediment layer close to the Island of Basiluzzo (Peterson & Monecke, 2009).

Table 1-1: Measured and calculated heat fluxes mentioned in different previous publications.

Measured and calculated heat flow	Heat flow [mW/m ²]
Pollack, Hurter & Johnson (1993)	\dot{Q}_{global} = 87 $\dot{Q}_{\text{continents}}$ = 67 \dot{Q}_{oceans} = 101
Spadini, Bertotti, Cloetingh (1995)	$\dot{Q}_{\text{Sardinian margin}}$ = 60 to 140 \dot{Q}_{oceans} = 20.8
Keppie, Currie, Warren (2009)	$\dot{Q}_{\text{continental}}$ = 55
GtV (2011) *	\dot{Q}_{global} = 65 $\dot{Q}_{\text{volcanic area}}$ = 217 – 434
IHFC (2011) **	$\dot{Q}_{\text{Aeolian Islands}}$ = 50 - 100

* source: GtV

** source: Heat flow map from the Mediterranean, Black and Red Sea's region published from the IHFC (Figure B 1).

The global rate of heat loss (equation [1.1]) across the surface of the Earth is generally defined as follows:

$$Q_{\text{global}} = Q_{\text{oceans}} + Q_{\text{continents}} \quad [1.1]$$

Pollack, Hurter & Johnson (1993) estimated a Q_{global} of $(4.42 \pm 1.0) \cdot 10^{13}$ W which is composed of $3.1 \cdot 10^{13}$ W heat loss across the oceanic crust and $1.32 \cdot 10^{13}$ W heat loss across the continental crust. Stein (1995) estimated 34 ± 12 % or $(1.1 \pm 0.4) \cdot 10^{13}$ W of ocean heat losses which are combined with hydrothermal flow. The average global specific heat flow of $\dot{q} = 87$ mW/m² which was published from Pollack, Hurter & Johnson (1993) (Table 1-1) was determined in a global recording. Therefore, 24774 observations at 20201 locations were made, thereof 10337 continental and 9864 marine surveillances. The average heat flow on the continents was determined to be lower than in the oceans. Reasons might be the different thicknesses and densities. Most of the heat flow data shown in Table 1-1 were calculated using Fourier's law of heat conduction. Temperature gradients were measured in the field and thermal conductivities were measured in the laboratory. Results from the International Heat Flow Commission (IHFC) are based on the Bullard method or thermal depth method (personal communication with Prof. Will Gosnold, IHFC) shown in Figure B 1. This method is used to calculate heat flow from borehole data when a significant variance of thermal conductivity occurs (caused by different geological units) within the depth range of temperature measurements (Pribnow, Kinoshita & Stein, 2000). Further information can be found in Bullard (1939) and Jessop (1990). For the Aeolian Islands the map prognosticates a heat flow between 50 and 100 mW/m². It is obvious that volcanic active regions show a higher heat flow than inactive regions. But the characterization of the investigation area by using this map is too imprecise.

During the last years' SDC field trips to Panarea, temperature measurements and a regular gauging from some interesting and special spots were performed. Leidig & Barth (2009) monitored the highest temperatures at "Black Point" (134 °C). Furthermore, temperatures on the gravel-field of this site varied between 25 °C and 93 °C and even more at some fumaroles.

1.3.2 Isotopic analysis

Isotopic differences are shown as a ratio between samples and standard in per mil (‰). The general equation [1.2] is performed in the following for the example $^{13}\text{C}/^{12}\text{C}$ -ratio.

$$\delta^{13}\text{C} = \left(\frac{{}^{13}\text{C}/{}^{12}\text{C}_{\text{Probe}} - {}^{13}\text{C}/{}^{12}\text{C}_{\text{Standard}}}{{}^{13}\text{C}/{}^{12}\text{C}_{\text{Standard}}} \right) \cdot 1000 \quad [1.2]$$

The natural occurring ratios of stable and instable isotopes which are measured within this thesis are shown in Table 1-2.

Table 1-2: Natural occurring ratios of stable isotopes after Hoefs (1997) that are of interest within this thesis. Ratio of the noble gases are determined for helium (Jordan, 1979), neon (Dicken, 1995) and argon (Faure, 1986a).

Element	Isotope	Natural abundance (%)	Isotope	Natural abundance (%)	Standard
Hydrogen	^1H	99.98	^2H	0.02	V-SMOW
Carbon	^{12}C	98.89	^{13}C	1.11	V-PDB
Oxygen	^{16}O	99.76	^{18}O	0.02	V-SMOW
Sulphur	^{32}S	95.02	^{34}S	4.21	V-CDT
Helium	^4He	99.99987	^3He	$1.37 \cdot 10^{-4}$	
Argon	^{40}Ar	99.6	^{36}Ar	0.337	
			^{38}Ar	0.063	
Neon	^{20}Ne	90.48	^{21}Ne	0.27	
			^{22}Ne	9.25	

The stable isotopic composition of water and solutes indicate, for instance, groundwater quality, geochemical evolution, recharge processes interaction between rock and water as well as the origin of salinity and contamination processes (Clark & Fritz, 1997).

The properties of noble gases can be explained with the general atomic structure. Because of the “full” outer shell of variance electrons, the gases show very low chemical reactivity and underlie no biological processes. Noble gases are thus an effective natural tracer for studies of the degassing processes in the mantle because of their inert property to other molecules. The isotopic composition of the molecules is appropriated just by physical processes (Pilz, 2008). They can give an answer about the origin of the gases and are a useful tool for monitoring by recording changes in the distribution of the isotopic composition.

2 DESCRIPTION OF THE INVESTIGATION AREA

2.1 Geological and hydrothermal settings of Panarea

The Aeolian Archipelago and the associated volcanic islets form a ring-shaped disposition around the Marsili basin and Marsili seamount. The approximately 200 km long volcanic chain with the seven major islands is separating the Marsili basin from the uplifting continental crust in the east called the Calabrian Arc and the continental slope of northern Sicily in the west (Calanchi et al. (1995), Pepe et al. (2000), Petersen & Monecke (2009)). The constellations are indicated in Figure 2-2.

Panarea Island is an emergent part of a submarine strato-volcano which is approximately 1600 m high and has an extension of about 18 km (Gabbianelli et al. (1993), Gamberi et al. (1997), Favalli et al. (2005)). The investigation area is located approximately 2.5 km to the east of Panarea Island with an elliptic dimension of 2.3 km² and a maximum water depth of about 30 meters (Esposito et al., 2006). A detailed map is shown in Figure 2-3. It is surrounded by the islets Datillo and Panarelli in the west, Lisca Bianca in the east and Bottaro as well as Lisca Nera south-eastern.

Panarea Island is mostly made up of andesitic to dacitic and rhyolite rocks, lava domes, volcanic plugs and coulees interbedded with pyroclastic material (Esposito et al., 2010). The volcanic rocks belong to calc-alkaline, high-K calcalkaline, shoshonitic and alkaline potassic associations (Favallim et al. (2005), Chiodini et al. (2006)). The islets in the east (Lisca Nera and Bottaro) are showing weathered and bleached rocks resulted by fumarolic activity in the past (Pichler, 1989). The emerging lava fractions in this area are characterized by a variable degree of hydrothermal alteration which strongly changes their mechanical properties (Cas et al., 2007).

The lava domes are dated between 149 ± 5 and 127 ± 1.5 ka (Calanchi et al. (1999), Lucchi et al. (2007)). The youngest age of the Panarea volcano system was appropriated at 20 ± 2 ka (Dolfi et al., 2007).

Hydrothermal discharge and shallow-water gas venting are recent in a 2.3 km² large area between the islets of Dattilo, Panarelli, Lisca Bianca, Bottaro, and Lisca Nera, in a water

depth less than 30 m (Gabbianelli et al. (1990), Calanchi et al. (1999), Esposito et al. (2006)). The regions are charted in Figure 2-1.

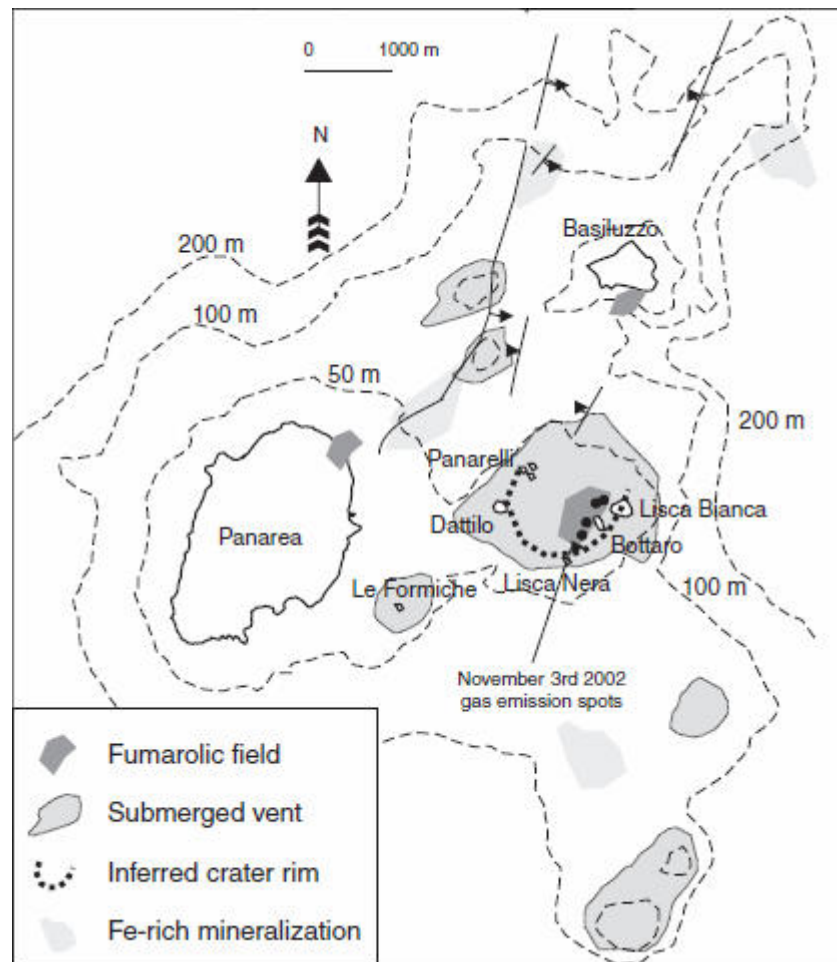


Figure 2-1: Simplified bathymetric chart which shows the location of Panarea islets, the occurring fumarolic fields and Fe-rich mineralization as well as the submerged emission vents. Additionally, the inferred crater rim and the location of the main gas emission in 2002 are shown. (Chiodini et al., 2006)

The Aeolian Islands are characterized by three main structural and volcanological fault systems (Locardi and Nappi (1979), Rossi et al. (1987), Manetti et al. (1989), Gabbianelli et al. (1990), Neri et al. (1991) (1996), Mazzuoli et al. (1995), Calanchi et al. (1995), Lanzafame & Bousquet (1997), Ventura (1995), Ventura & Vilaro (1999), Tibaldi (2001), Bonaccorso (2002)) which are also shown and highlighted in Figure 2-2.

- The western sector with the WNW-ESE striking fault system (SA stands for “Sisifo-Alicudi”) (De Astis, Ventura & Vilaro, 2003). It ranges from the Glauco seamount to

the Alicudi and Filicudi Islands. In this sector, the volcanism developed between 1.3 Myr and 3040 kyr (Beccaluva et al. (1982 and 1985), Santo & Clark (1994)).

- The central sector with the NNW-SSE striking fault system (TL stands for (“Tindari-Letojanni”) which includes the islands of Salina, Lipari and Vulcano (Barberi et al., 1994). The volcanism in this sector started at approximately 0.4 Myr after Beccaluva et al. (1985) and it is still active at Lipari (580 AD) and Vulcano (1888–90 AD). The last eruption at Salina happened at 13 kyr (Keller, 1980) and fumaroles and hot springs exist at several sites. The area is characterized by shallow seismic activities (Gamberi et al., 1997).

- The eastern sector with the NNE-SSW to NE-SW striking fault system extends from Panarea and Stromboli Islands to the Alcione and Palinuro seamounts (Volpi et al., 1997). The volcanism in this sector started at about 0.8 Myr and it is still active at Stromboli. In contrast, the submarine zone of Panarea and the eastern seamounts are characterized by fumaroles and very shallow seismicity (Soloviev et al., 1990).

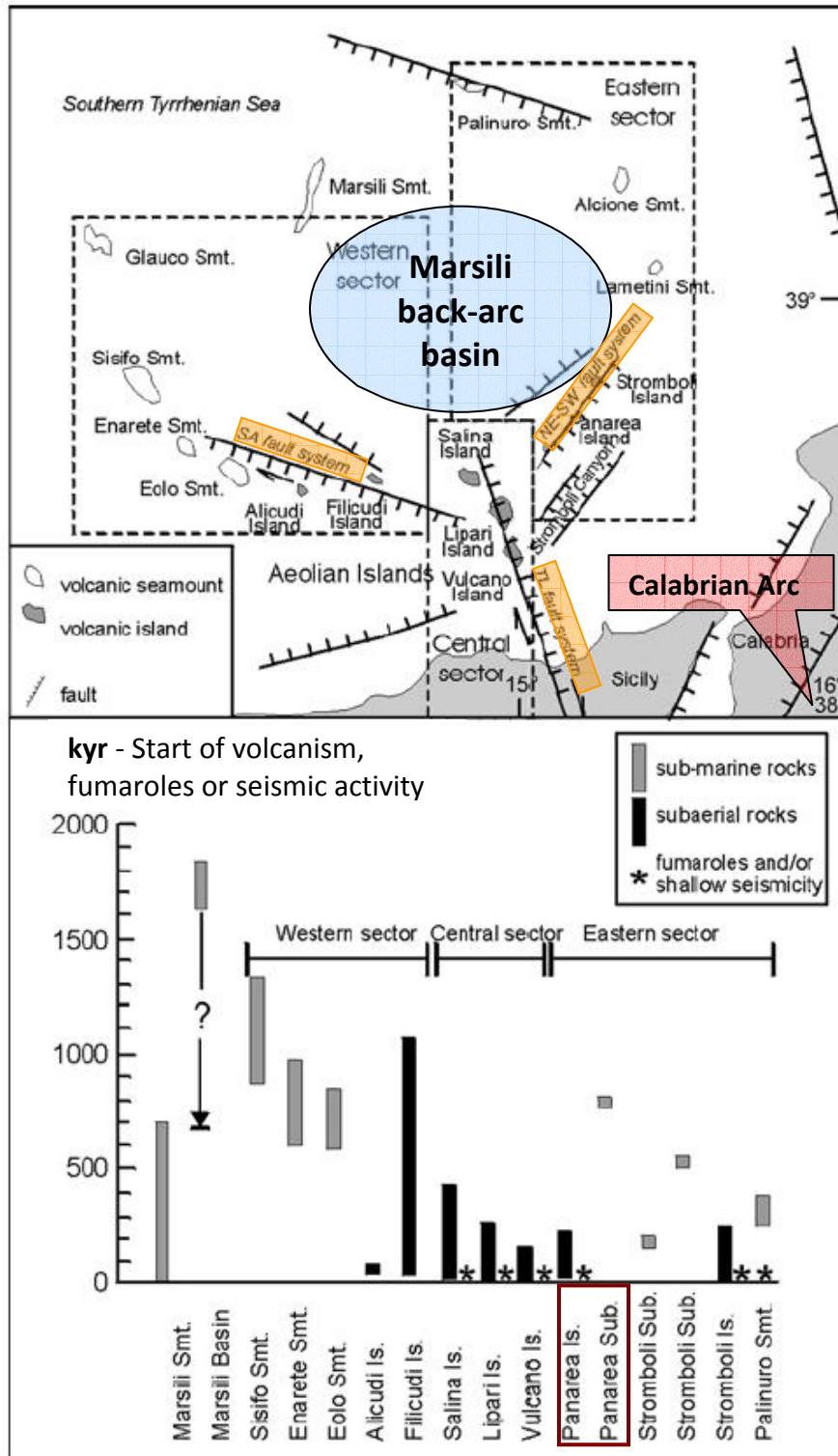


Figure 2-2: Structural sketch of the Aeolian area and chronological evolution of the volcanism, fumaroles or seismic activity. The geochronological information characterizes the volcanic rocks from the subaerial (Is.) and submarine (Sub.) parts of the islands as well as seamounts (Smt.). Sources of these data are: Barberi et al. (1994), Beccaluva et al. (1982, 1985), Calanchi et al. (1995, 2002), Continisio et al. (1997), Crisci et al. (1991), De Astis et al. (1997a, 1997b), De Luca et al. (1997); Finetti and Del Ben (1986); Gillot (1987), Hornig-Kjarsgaard et al. (1993), Lanzafame and Bousquet (1997); Keller (1980), Manetti et al. (1995), Marani and Trua (2002), Pichler (1980), Santo and Clark (1994), Soloviev et al. (1990) (modified after Müller, 2011).

2.2 Maps of the investigation area

Most of the investigation sites are located approximately 2.5 km easterly off the coast of Panarea Island between several islets (Dattilo, Lisca Bianca, Bottaro and Lisca Nera.). These islets are presumed to be remnants of a crater rim which encloses a submarine platform (Gugliandolo et al., 2006). The plateau has a dimension of about 4 km² with water depths up to 30 m (Italiano & Nuccio, 1991). During the field campaign in August 2010 seven different locations were explored. These diving locations are called “Bottaro North” (BN), “Bottaro West” (BW), “Point 21” (P21), “Hot Lake” (HL) with the “Fumarolic Field” (Fum F), “Area 26” (A26), “Black Point” (BP), “La Calcara”. The last mentioned spot is a new location which is located very close to Panarea Island (approximately 200 m from the coast) shown in Figure 2-3 and Figure 2-4. Temperature measurements in “La Calcara” yielded the previously highest temperatures measured in a sediment depth of 500 mm (Section 4.1.2) that were measured in the scope of previous monitoring campaigns to Panarea (made by the SDC Freiberg). More information about the other diving locations can be looked up at Hamel (2010), Sieland (2009), Steinbrückner (2009), and Roland (2007).

Based on the collaboration with the INGV a bathymetric map with a accuracy of 1 meter per pixel was available for interpretation and evaluation. It displays all diving locations apart from “La Calcara” and Panarea Island itself.

In the following results of the delineation using DGM and GPS readings of all diving locations are presented. Different GIS programs were used:

MapSource® (Version 2.02)

QuantumGIS (QGIS) (Version 1.5.0 and 1.6.0)

Geomatica® (Version 10)

Another tool to verify coordinates of certain locations was Google™ earth (version 6.0 Beta).

In Italy different coordinate- and reference-systems are used (selection is shown in Table A 4). So, it was necessary to harmonize the available data. Different GIS programs were used visualizing the measured diving spots on top of the bathymetric map and check the correctness of the exposure.

The coordinates of the diving spots and the checkpoints were taken with a Garmin handheld GPS (Type GPSmap 276c) by means of Universal Transverse Mercator (UTM) with World Geodetic System 84 (WGS-84). All coordinates of the diving spots and check points are shown in Table A 2 including the coordinates from 2007 and 2008.

➤ Results with MapSource®

MapSource® is a commercial software program included with the Garmin GPS hardware which contains detailed electronic nautical charts for several offshore regions and as well the Aeolian Islands. Unfortunately MapSource® does not display the coordinates of the diving spots and checkpoints on the correct position (Figure 2-3). The points are displaced approximately 229 m in 140° northwest direction. This discrepancy was proven with the fixed point “Leuchtfeuer”, also shown in Figure 2-3. The coordinates of this site was read MapSource® and was measured with the GPS. The shift between the MapSource® point “Leuchtfeuer” and the true position can be measured with a straight edge function. Obviously the MapSource® map of this area has a biased georeference.

➤ Results with QGIS (verification with Geomatica® and Google™ earth)

All points of the diving spots and reference points were loaded in the Open Source program QGIS together with the bathymetric map. To get a better information of the sea bottom (3D effect) the method “hillshading” was performed which calculates from a DEM (elevation) the slope and aspect of each cell, then simulates the sun’s position in the sky and gives a reflectance value to each cell (QGIS userguide ‘Tethys’). The map is modified to a pseudo map to display the differences in the water depth with a higher contrast.

In this case the bathymetric map (Figure 2-4) and the GPS coordinates of the diving spots fits rather well. No displacement of the measurement points was observed. This can be easily checked on the diving location “Bottaro West” (BW). Caliro et al. (2004), Caracausi et al. (2005) and Esposito et al. (2006) characterize a typical ellipsoidal crater which has a dimension of 35 x 20 m and a depth of 8 m resulting by the submarine explosion in 2002 (further information, Chapter 1.1). The plotted GPS point of BW exactly fits in the geological area that is distinctive for this diving spot.

To verify this assumption the UTM coordinates with WGS-84 (33S) of the diving spots were used in two other programs, Geomatica® and Google™ and the spots were displayed at the same, correct position.

It can be concluded that the coordinate system and reference system of the used bathymetric maps is the same that is used during the measurements of the dive spots with the Garmin measurement instrument (UTM with WGS-84, 33S). To verify the reference points surveyed on Panarea, an additional terrestrial map from the island would be necessary. One possibility is to overlay GDEMs (Global Digital Elevation Map Model) that can be downloaded on the websites from NASA or the Japanese Ground Data Systems. But the resolution is only one pixel per 30 meters which is too low to characterize details of the investigation area. Unfortunately, it was not possible to obtain a map of Panarea with a better resolution respectively scale.

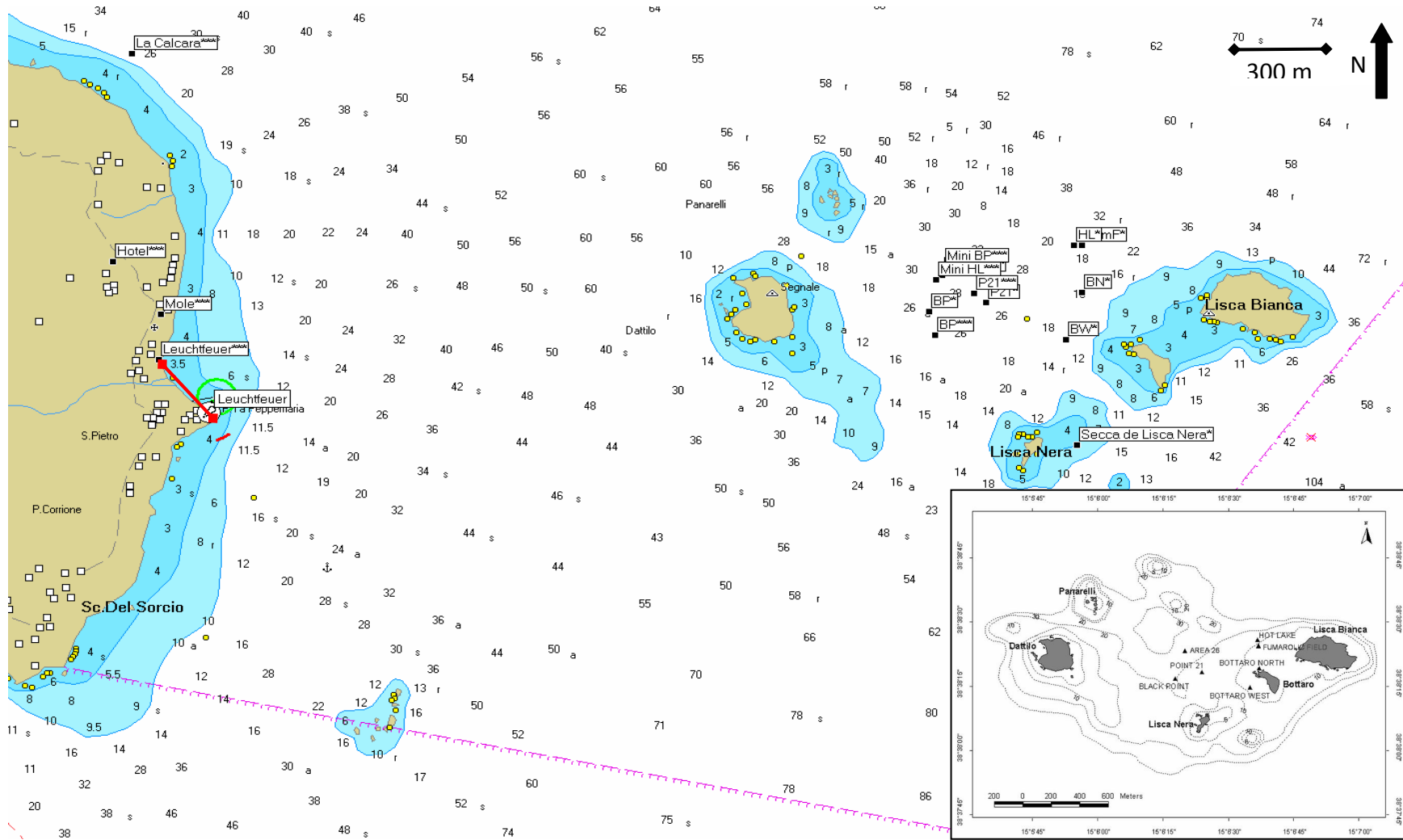


Figure 2-3: Map in the below right shows the investigated sites (triangles) in the hydrothermal system east of Panarea Island. The shallow submarine area is surrounded by the islets of Dattilo, Panarelli, Lisca Bianca, Bottaro and Lisca Nera (Steinbrückner, 2009). In the colored map made with the MapSource® program the measured shifted diving locations are shown. The inaccuracy can be determined by the fixed point “Leuchtfeuer”. The measured and the true location are charted in the map (red line).

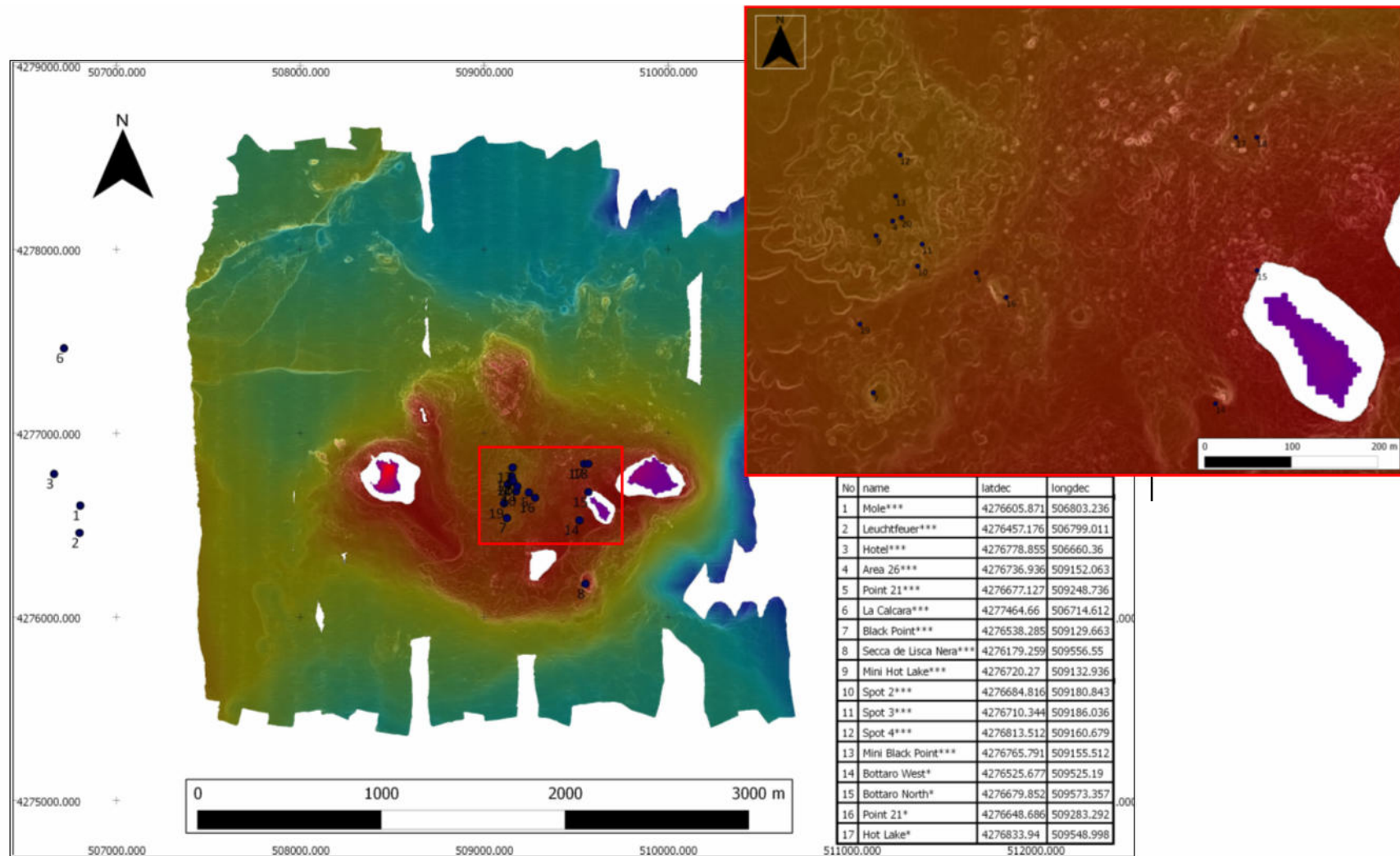


Figure 2-4: Bathymetric map showing the investigation area and the surrounding field to a water depth of 120 meters (blue). The diving spots are located between the islands Datillo and Lisca Bianca in a water depth up to 30 meters. A detailed map is shown in top right. The numbers, the associated coordinates (in UTM WGS84, Zone 33S) and names of the dive locations are described in the table aside. (coordinates: * modified from Rohland (2007); ** modified from WISTAU (2008), *** modified from WISTAU (2010))

3 METHODOLOGY

3.1 Thermodynamic measurements

3.1.1 Heat flux

The heat flux measurements underwater were implemented by a heat flux plate (HFP) from Ahlborn (FQ 90118) with a dimension of 120 * 120 * 1.5 mm. The heat flux plate consists of meandering thermo couples which are embedded in a carrier material (epoxy resin). When heat flux with a definite thickness is occurring through the plate, a temperature gradient will be generated that is proportional to the density of the heat flux. The sensor delivers signals are displayed in milli-volt range. The measured voltages have to be multiply with a device constant (equation [3.1]) to calculate the heat flux density. (Koschke et al., 2009) This constant c is given by the compensation protocol with a value of 9.65 W/m²mV determined by a one-plate-facility.

$$\dot{q} = c \cdot U \quad [3.1]$$

whereas: \dot{q} = Heat flux density [W/m²]
 c = Device constant [W/m²mV]
 U = Measured voltage [mV]

Figure 3-1 shows the needed tools for a heat flux measurement used in the field. To make successful measurements the plate has to cover the sediment completely to maintain a good contact of the plate over the whole surface.



Figure 3-1: Top: Necessary equipments for heat flux measurements including the measurement instrument from Ahlborn, AHLMEMO® 2590-3S; Bottom: Measurement instrument at the sea floor, "Point 26"

The plate was adapted for the use underwater because it is normally used to measure the heat flux of building materials. It was encapsulated with bitumen to protect the sensitive instrument against the aggressive sea water. The edges of the plate were treated with epoxy resin and stiffen by thin plastic stabs. The measurement device used is an Ahlborn ALMEMO® 2590 which can log the heat flux density. The data can be uploaded as a txt-file with the software AMR Control 5.13. The device is housed water proof in an acryl-glass container which allows the underwater handling of the most important features of the device.

3.1.2 Temperature gradient

The temperature gradient sensor was developed to measure the temperature gradient at sites with a sufficient sediment thickness. The temperature gradient is determined as the quotient of the temperature difference in known depth to the interval. Theoretically such readings can be done by means of one thermo-element stabbed into different depth of the sea bottom sediments. But underwater it is difficult to get accurate readings of the penetrated depths. Therefore a sensor was designed which can measure the temperature in different depth simultaneously with the help of four thermo couples (Type “K”) integrated in definite intervals in the lance (Figure 3-2). The thermo couples stem from the same charge with the same thermo electrical properties which were tested in the laboratories of the Institute of Thermal Engineering, TUBAF (Calibration, Chapter 3.1.4).

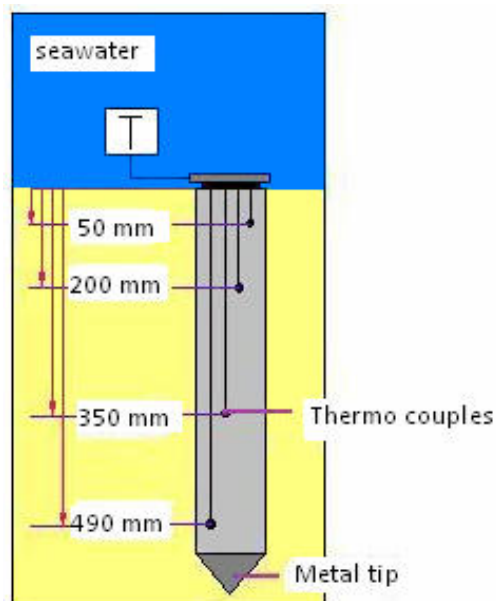


Figure 3-2: Scheme of the temperature gradient sensor with four integrated thermo couples

The outer shell of the probe is made of a special material called Tufor (10G/40) that has similar thermal conductivity than sediment-water mixtures (approximately $0.42 \text{ W}/(\text{m}^*\text{K})$). Slots were milled into the probe with a diameter of 10 mm to the respective depth to host the thermo couples. The temperature is read with a water proof housed PCE T-390 that has the possibility to measure the temperature of four thermo couples simultaneously and to save the data on a secure digital memory card (SD-card), as an excel-file.

Temperatures are taken in depth of 50, 200, 350 and 490 mm referring to the distances of the integrated thermo couples in the lance. It is important for the measurement that the sensor is completely recessed into the sediment (Figure 3-3). If this is not possible because of an insufficient sediment thickness the remaining length of the sensor has to be documented for subsequent corrections.

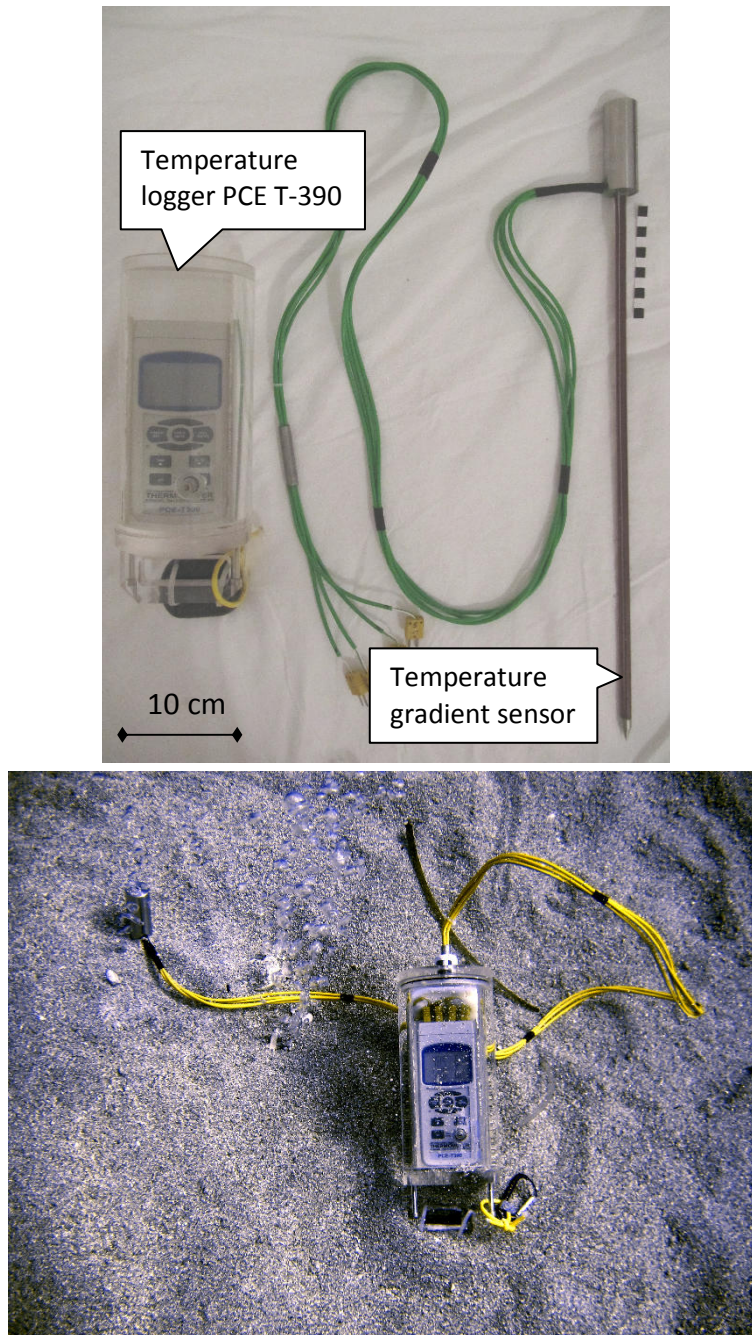


Figure 3-3: Top: Temperature gradient sensor with water proof housed PCE T-390; Bottom: Temperature gradient sensor with PCE T-390 at the sea floor, "Area 26"

3.1.3 Thermal conductivity

The thermal conductivity sensor consists of one thermo couple surrounded by a heating element (total length of 1.24 m and diameter of 0.05 mm, consists of CrFeAl 135, Berghütten® GmbH). These two units are applied and bonded by a ceramic rod. The principle measuring method is based on a non-stationary approach and called heated-filament technique. The thermal conductivity is based on heat transfer caused by conduction.

Further information can be found in Carslaw & Jaeger (1959). This process is standardized according to DIN EN 993-14.

A scheme of the configuration is shown in Figure 3-4. The power supply is managed with a 50 m long cable to a battery placed on the boat during the measurement (Figure 3-5, top). To measure the heat conductivity of the sediment, it is necessary to recess the whole length of the sensor into the sediment as seen in Figure 3-5. Subsequently the power is switched on and the heating element warms up. With the connected temperature logger PCE T-390 the temperature increasing is monitored.

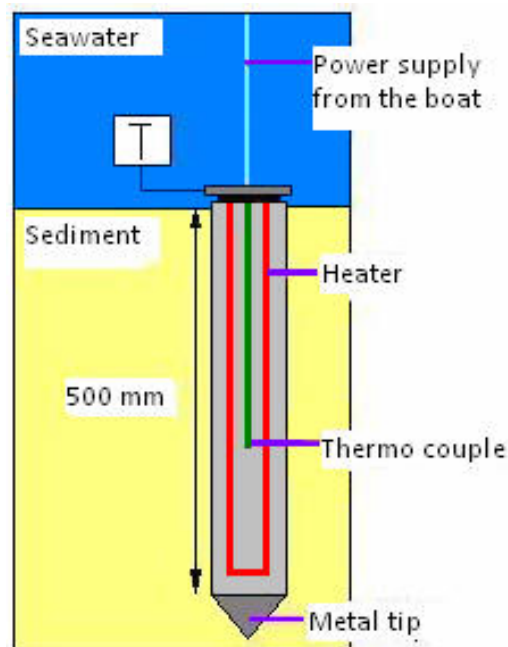


Figure 3-4: Scheme of the thermal conductivity sensor

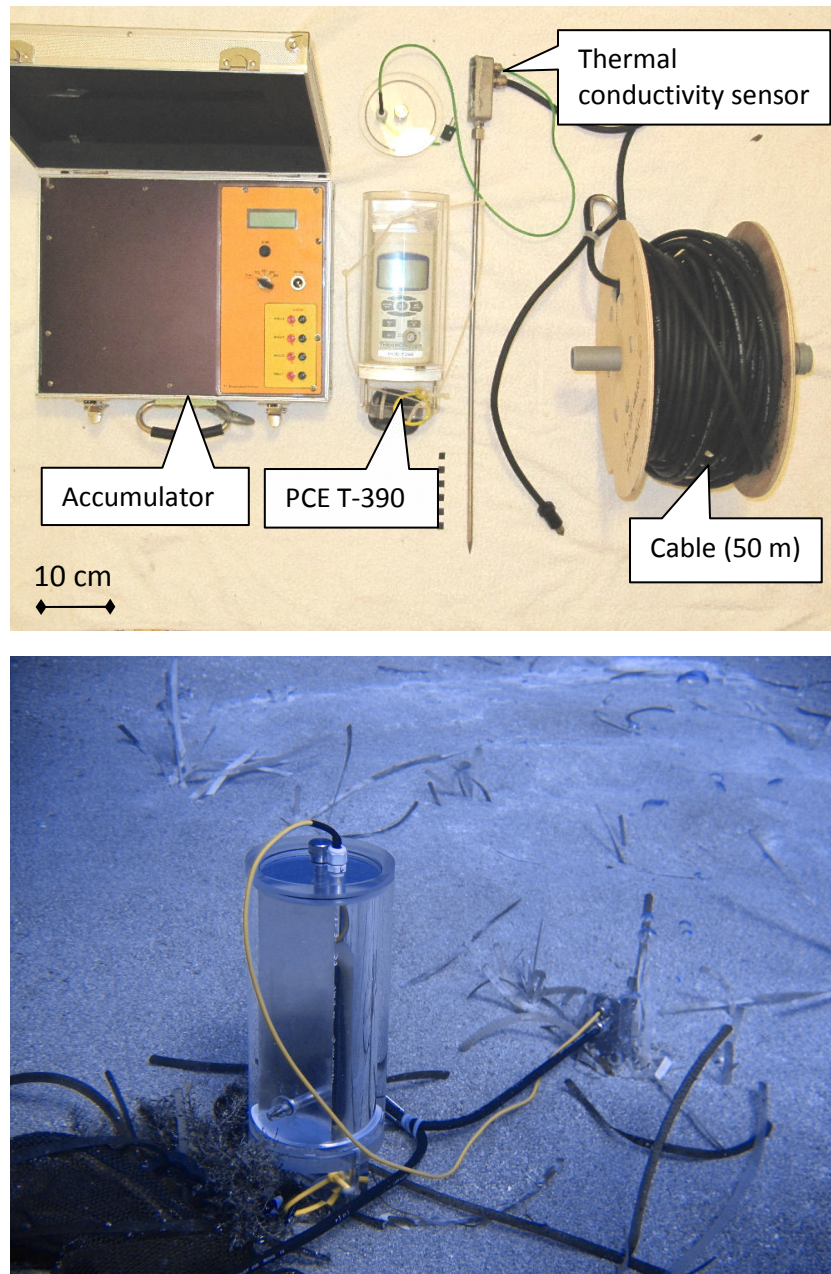


Figure 3-5: Top: Necessary instruments for thermal conductivity measurements; Bottom: Thermal conductivity sensor at the sea floor, "Area 26"

During one dive it is possible to measure the heat conductivity on two places; each heating phase should take 5 minutes to get significant data. The battery gives constant power for approximately 10 minutes. Voltage and amperage can be supervised and should be documented during the measurement by a person on the boat. If a sudden voltage drop happened, the power has to be turned off immediately. For a smoothly measurement it is helpful to navigate the boat very close to the measurement point because of the limiting length of the cable.

3.1.4 Calibration of the sensors

➤ Heat flux plate

The calibration of the plate was made by AHLBORN using a one-plate gadget and a mean temperature of 23 °C as well as a heat flux density of approximately 100 W/m², as prescribed by the protocol. Therefore the sensor was embedded between two foam rubber plates. It documents that the heat flux plate delivers a value of 9.65 W/m² when a thermoelectrical potential of 1 mV is applied. This number is saved in the measurement instrument and used in further measurements.

➤ Temperature gradient sensor

The calibration of the temperature gradient sensor was made before and after the field work in Panarea at the Institute of Thermal Engineering, TUBAF.

In the first experiment the sensor was put into water which was heated up to different temperatures with the help of a thermostat MLW (VEB Testing instruments) to temperatures of 25 °C, 50 °C and 70 °C. To get constant conditions a pump was circulating the water. All thermo couples were checked how fast they adapted to the temperature and whether showing the same temperature.

In a second experiment, the sensor was put into a cylinder filled with saturated sand. For further calculations, we used the lower three thermo couples (2, 3 and 4) because the sensor could not insert completely into the sediment (first TC remained out of the sediment). The installation for the two experiments is shown in Figure 3-6.

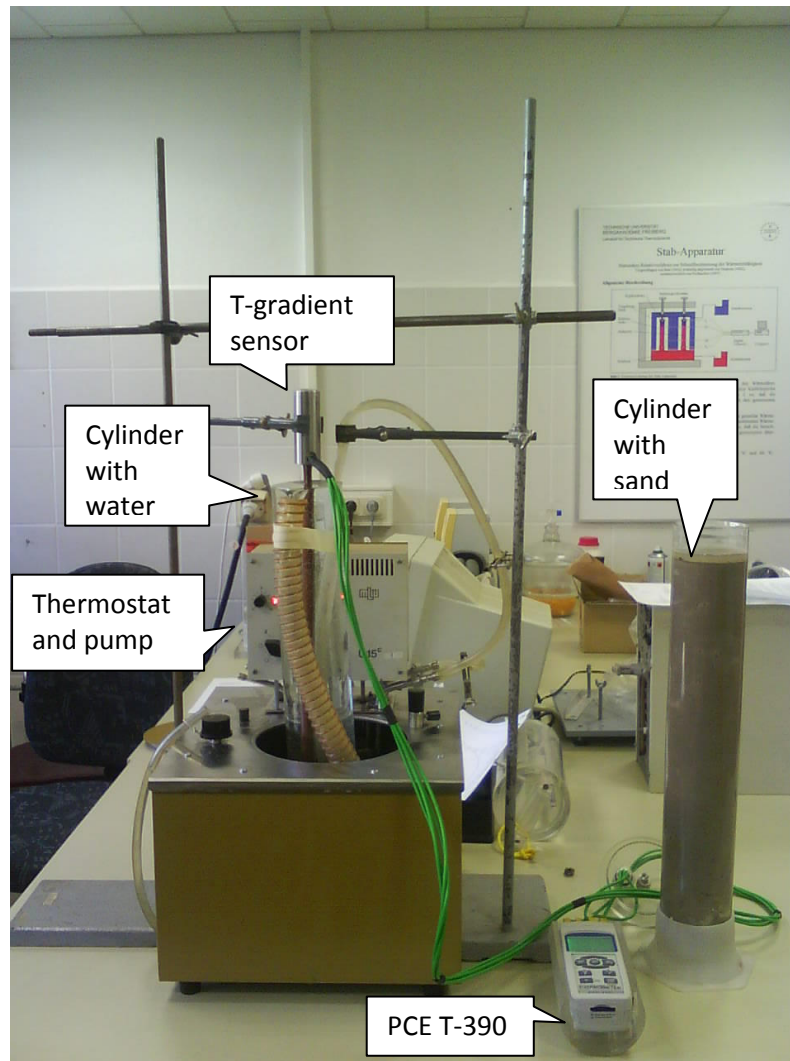


Figure 3-6: Experiment to calibrate the temperature gradient sensor in a cylinder filled with water (left) and sand (right). The sensor was recessed into the cylinders and the temperature progression was documented with the temperature logger PCE T-390.

➤ Thermal conductivity sensor

Laboratory experiments to calibrate the sensor were made at the Institute of Thermal Engineering at the TUBAF contemporary before the field work in Panarea and after that.

In a first experiment before the field measurements at Panarea the temperature adjustments of the sensor were investigated for different temperatures (50 °C and 65 °C) maintaining a constant voltage of 12 V and a constant amperage of 1.27 A. In a second experiment current flux and temperatures for different voltages, 24 V and 48 V were measured. The aim was to quantify the potential loss of current flux. The reason is the increasing resistance by temperature rise. The measuring set up can be seen in Figure 3-7.

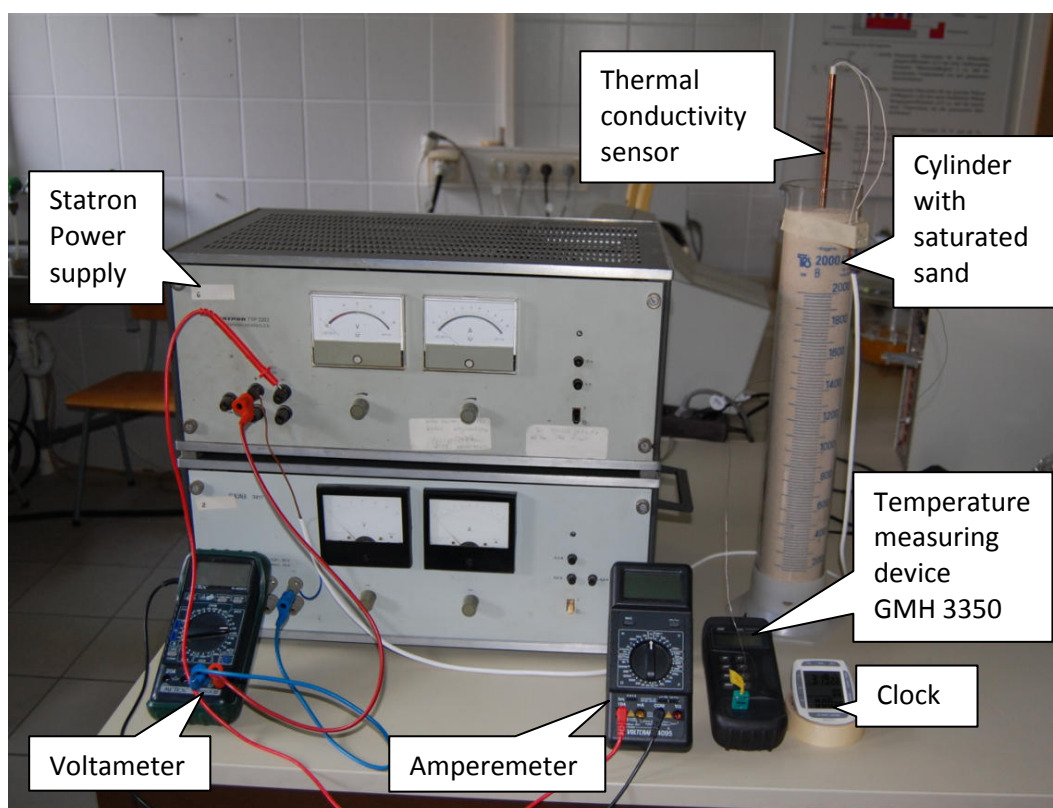


Figure 3-7: Experiment to calibrate the thermal conductivity sensor in saturated sand. Power supply ensured by a device from Statron GmbH (32 V / 16 A, type 3233.1). Temperature measurement with GMH 3350 (Greisinger electronic GmbH).

3.2 Sampling Procedures

3.2.1 Water and gas sampling

Hydrothermal water and gases were sampled for geochemical analyses at the INGV, TUBAF and the UFZ. To get an uncontaminated sample it is important to clean the container before samples are filled into bottles or tubes. The functionality of the instruments were checked before the use underwater. Valves of the gas samples tubes have to work smoothly. Otherwise the gas sample may get contaminated with atmospheric air.

Materials needed for both sampling procedures are shown in Figure 3-8. The filling of a gas sampling tube underwater is also illustrated in Figure 3-9. In the following are described instruments and steps for a successful gas and water procedure are described.

➤ Water sampling

Used materials:

- 2 Pyrex bottles (borosilicate)
- Teflon (PTFE)-tube with 3-way valve made from PE and PP
- PE syringe (100 ml)
- Rubber tube to connect syringe with Pyrex bottle
- Stainless metal funnel

Work steps:

1. Fill Pyrex bottles with sea water
2. Put metal funnel over a gas vent and connect Pyrex bottle with metal funnel
3. Evacuate sea water from Pyrex bottle by filling with gas from the vent
4. Put Teflon tube in the sediment where the thermal water discharge is located
5. Connect syringe and teflon tube with the three way valve
6. Purge Teflon tube-syringe-system with thermal water (3 times)
7. Connect Pyrex bottle with purged teflon tube-syringe-system
8. Inject water in the Pyrex bottle with the syringe (2 refills of the syringe to completely fill one bottle)
9. Close filled Pyrex bottle and fill the second bottle with the same procedure

➤ Dry gas sampling

Used materials:

- 3 gas sampling tubes
- stainless metal funnel

Work steps:

1. Fill gas sampling tubes with sea water before the dive
2. Put metal funnel over an appropriate gas vent (fumarole)
3. Connecting of the gas sampling tubes with the metal funnel
4. Flushing with gas for approximately 1 minute
5. Close gas sampling tubes (first outlet valve then inlet valve)

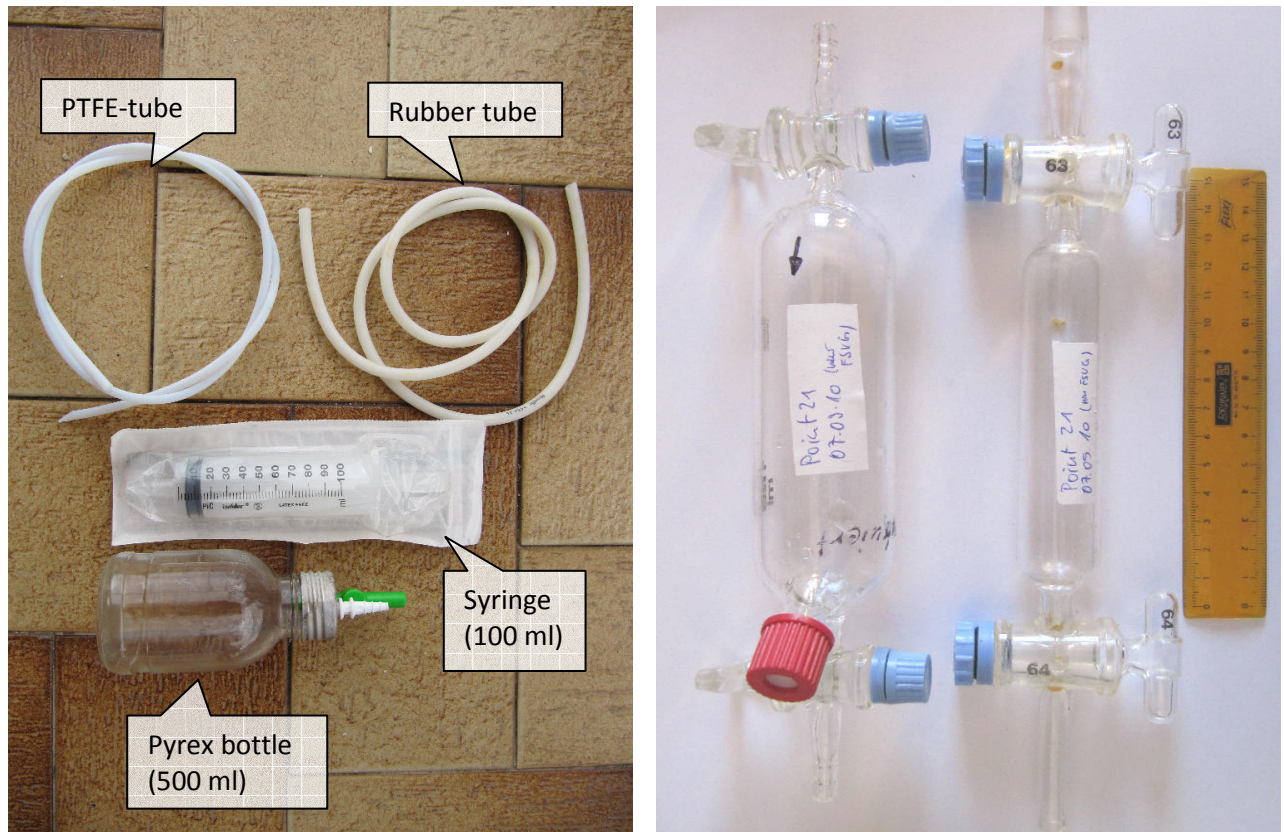


Figure 3-8: Left: Instruments for water sampling. Not shown: three way valve and metal funnel; Right: Instruments for gas sampling. Two gas sampling tubes: from TUBAF with a septum (tube left) and from INGV without a septum (tube right).

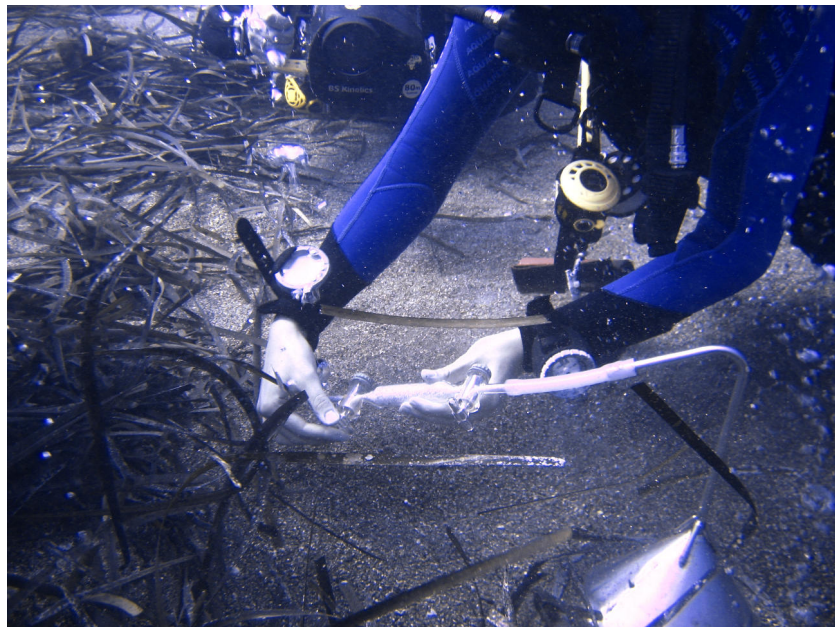


Figure 3-9: Gas sampling at a gas vent (fumarole) with a gas sampling tube and a metal funnel

3.2.2 Preparation and storage of the samples

Gas sampling tubes were stored after the sampling in metal case provided by INGV. The probes were stored dark and protected against vibrations during the transport to the laboratories of INGV in Palermo.

The water samples on the other hand were stored in the fridge after decanting in PE bottles. 2 bottles were filled with unprepared water sample (one reserve) one filtered and a third bottles with filtered water and subsequently acidification. The filtration was made with 0.2 µm cellulose acetate filters. 20 µl of ultra pure nitric acid (65 % HNO₃) was used to acidify the samples (pH<2). An overview of the preparation and storage for different chemical analyses are shown in Table 3-1.

Table 3-1: Preparation and storage of water samples for further chemical analyses.

Analysis	Preparation	Storage
On-site parameters	No preparation	Immediate determination
Isotopic analyses	No preparation	50 ml PE bottles
Photometry	Filtration	Immediate determination
IC	Anions	Filtration
	Cations	Filtration, acidification
ICP-MS	Filtration, acidification	50 ml PE bottles

The advantages to precipitate the dissolved hydrogen sulphide (H₂S) and carbon dioxide (CO₂) fractions in gas and water samples are on one hand the fixation of the existing isotope compositions (avoid volatilization of lighter isotopes) and on the other hand the easier transportation of the solid fraction. The analyses do not need to be done instantly.

The fixation of sulphide in gas samples for δ³⁴S analyses was arranged with a mixture of 450 ml 0.208 M ultrapure NaOH and 50 ml 0.156 M ammonia zinc acetate solution in a washing bottle through which the gas was pumped by means of a filter frit with a rate of approximately 300 ml gas per minute. Precipitated zinc sulphide (ZnS) was given time to settle and the filtered and air dried. The precipitation of gaseous CO₂ for δ¹³C analyses was accomplished by using a 0.57 M BaCl₂ solution in the washing bottle through precipitation of BaCO₃.

To precipitate the existing sulfur components (sulphide and sulphate) in water 50 ml of the ammonia zinc acetate solution was added to 1 L of sample to form ZnS precipitate. After 24 hours, supernatant water was withdrawn and the remain ZnS filtered and dried. The supernatant water was used to precipitate BaSO₄ by adding HCl to ensure a pH value of 4 (to avoid BaCO₃ precipitation) and then 10 ml of 0.57 M BaCl₂ solution. Precipitate was filtered after 24 hours and air-dried.

Further informations are given in Robert Sieland (2009). Table 3-2 shows the precipitated fractions and the appropriated isotopic analyses which were made with these solid materials at the UFZ in April 2011. The specified probes were collected during the expeditions in 2009 and 2010.

Table 3-2: Solid material precipitated from gas and solid samples for different stable isotopic analyses at the UFZ (for measurements in April 2011).

Origin	Chemical type of precipitation	Isotopic analyses (number of samples)
Gas (2009/2010)	BaCO ₃	$\delta^{13}\text{C}_{\text{DIC}}$ (6)
	ZnS	$\delta^{34}\text{S}_{\text{sulphide}}$ (13)
Water (2009/2010)	BaSO ₄	$\delta^{34}\text{S}_{\text{sulphate}}$ and $\delta^{18}\text{O}_{\text{sulphate}}$ (17)
	ZnS	$\delta^{34}\text{S}_{\text{sulphide}}$ (17)

All solid materials shown in Table 3-2 and all water samples were analyzed at the UFZ in April 2011 for the different isotopic contents.

3.3 On-site parameters

The immediately determinations of the on-site parameters pH-value (pH), electrical conductivity (EC), temperature (T), oxygen content and redox potential (E_h) were made in the field laboratory on Panarea using unfiltered sample. All parameters were taken in a Polyethylene beaker which was covered by a plastic film to avoid contact with ambient air.

➤ Specific electrical conductivity

The specific electrical conductivity (EC) of the water samples was determined with a WinLab Data Line Conductivity-Meter from WINDAUS LABORTECHNIK and a WTW TetraCon 325

electrode. This device recalculates the EC automatically to a value of 25 °C (linear temperature correction of 2 % per 1 K). The measuring instrument was checked by measuring the electrical conductivity of a standard solution (0.5 M KCl).

➤ pH and water temperature

The pH and water temperature were taken with the pH-meter HQ40d multi HACH 05-2009. The electrodes consist of inner electrolytes, 3 M KCl (HQ40d). Two-point calibration of the pH probe was performed with pH 4 and pH 9. After finishing the field experiments the accuracy of the pH-meters was re-checked.

➤ Dissolved oxygen content

The dissolved oxygen content was determined with the optical sensor LDO HQ40 02-2008. There is no need for a calibration because the sensors contain a LED which officiate as internal standard for the calibration of the whole optical system.

➤ Redox potential

The redox potential was determined using a WinLab Data Line pH-Meter from WINDAUS LABORTECHNIK Meinsberg Redox EMC 33-L (11-2007) and an Ag/AgCl electrode from PCE with a 3 mol/L KCl solution. Initially, the measuring device was checked on functionality using a redox standard solution.

In general the measuring procedure was performed as fast as possible after sampling. Thereby, it was tried to avoid as much as possible contact with the atmosphere. The measurements were carried out in a titration vessel. The holes in the cap were sealed with parafilm. The readings (E_m) were corrected for temperature with equation [3.2].

$$E_{o(25^{\circ}\text{C})} = E_m - 0.198 \cdot (T - 25^{\circ}\text{C}) \quad [3.2]$$

whereas: $E_{o(25^{\circ}\text{C})}$ = Standard redox potential based on 25 °C [mV]

E_m = Measured redox potential [mV]

T = Temperature [°C]

Afterwards, the redox potential ($E_{o25^{\circ}\text{C}}$) was converted to the potential of a standard hydrogen electrode (E_h) by a correction factor of 207 mV (Hölting & Coldeway, 2005). For

better comparability of the results the rH-value was calculated which is independent from pH conditions (equation [3.4]). It is defined as the negative common logarithm of the partial pressure from hydrogen which a platinum-electrode should charge to perform an equal reduction effect (Höiting & Coldeway, 2005). Before the determination of the E_N value have to accomplished with equation [3.3].

$$E_N = 2.3 \cdot \frac{R \cdot T}{F} \quad [3.3]$$

whereas: R = ideal gas constant, 8.314 J/(mol*K)
 T = absolute temperature [K]
 F = Faraday-constant, 96.484 * 10³ J/(V*mol)

$$rH = 2 \cdot \frac{E_h}{E_N} + 2 \cdot pH \quad [3.4]$$

whereas: rH = Redox capacity of a system, $rH = -lg(p_{H_2})$
 E_h = Redox potential at 25°C referred to standard hydrogen potential [mV]
 E_N = Nernst voltage [mV]
 pH = pH-value

➤ Photometry of ammonium (NH₄⁺), sulphide (S²⁻) and nitrite (NO₂⁻)

The amount of ammonium (NH₄⁺), sulphide (S²⁻) and nitrite (NO₂⁻) were determined using a DR/890 portable Colorimeter (HACH®). Therefore filtered water (200 nm) was used. Table 3-3 shows the precision obtained for each ion as well as the range of concentration and the estimated detection level (EDL).

Table 3-3: Measuring range, precision and EDL of the measured ions.

Ion	Classification after HACH®	Range [mg/L]	Precision [mg/L]	EDL [mg/L]
Sulphide	8131	0 to 0.07	± 0.02	0.01
Nitrite	8507	0 to 0.35 (NO ₂ -N)	± 0.001	0.005
Ammonia	8155	0 to 0.5 (NH ₃ -N)	± 0.02	0.02

Results were corrected for seawater according to Rohland (2007). The equations for each ion are given in Table A 6.

3.4 Laboratory analyses

The analysis of water and gas samples was performed in three different laboratories. The first measurements were made at the INGV in Palermo in September 2010 regarding stable and noble isotopes with mass spectrometry, main gas contents with gas chromatography (GC) and main ions in water with ion chromatography (IC). Further analyses (ICP-MS, GC and IC) were accomplished in the Hydrogeology laboratories of TUBAF during November and December. In April 2011 stable isotopes in water and gas samples were determined at the UFZ Halle / Saale.

3.4.1 Composition of the fluids

3.4.1.1 Ion chromatography (IC)

IC was used to determine the major concentration of cations and anions in the water samples in the laboratory of Hydrogeology, TUBAF and the laboratory at the INGV in Palermo.

Analyses at the INGV in Palermo

A DIONEX ICS-1100 RFIC was used to determine anions and cations separately (Cl^- , Br^- , SO_4^{2-} and Li^+ , Na^+ , K^+ , Mg^{2+} , Ca^{2+}). Every day 6 standards were run for quality control. 200 μl of filtered sample were prepared whereat 25 μl were actually injected. Each measurement need approximately 16 minutes. Because of the high salinity, samples had to be diluted before the analyses (dilution factor of 500 for cations and anions). The diluted samples for cation measurements were acidified before injection.

Analyses at the TUBAF

Cations (Na^+ , K^+ , Mg^{2+} , Mn^{2+} , Li^+ , Ca^{2+}) were determined with a Metrohm 872 Extension Modul. For the anion analyses (Cl^- , Br^- , SO_4^{2-} and F^-) a Metrohm 881 Compact IC pro was used. Different dilutions were prepared and analyzed to obtain a higher accuracy of the

results. Dilution factors of 51, 251 and 501 for samples from Hot Lake were arranged for anion measurements. For cation analyses dilution factors of 11, 21, 51, 100, 251 and 501, depending on the salinity were applied. Samples were acidified with 20 μl of 1M HNO_3 before the measurement.

3.4.1.2 Inductively Coupled Plasma - Mass Spectrometry (ICP-MS)

Trace element analysis was performed by the ICP-MS (X Series 2 from Thermo Scientific) in the laboratory of Hydrogeology, TUBAF. All samples (filtered and acidified) were diluted with a factor of 21 except the samples from “Hot Lake” which have a high salinity and were diluted with a factor of 41. Furthermore samples from the location “La Calcara” were measured with a further dilution factor of 101.

10 μl of each sample was spiked with an internal standard of 100 μl . The internal standard consists of 65 % HNO_3 (suprapur) and contains 5 mg/L of Germanium (Ge) and 1 ml/L of Rhodium (Rh) and Rhenium (Re). Quantification was executed by a standard calibration curve for each element. Most elements were measured in normal mode (argon as carrier gas), however, some elements (S, P, Ni, Al, Fe, Ge, Rh etc.) were measured in collision mode utilizing a collision gas consisting of 93 % He and 7 % H_2 .

3.4.1.3 Total inorganic carbon (TIC) / Alkalinity

Analyses at the INGV in Palermo

Alkalinity of water samples was determined by titration with HCl (0.1 mol/L, 0.1 N, MERCK Chemicals). Sample volume was 10 ml (As-it-is sample, not filtered or acidified). Methyl orange was used as indicator which appears orange in acidic conditions and yellow in alkali conditions. The color change happens between pH 3.1 and 4.4. Before the experiment the color change point was checked with tap water.

3.4.2 Gas composition with gas chromatography

Analyses at the INGV in Palermo

A Clarus 500 Gas Chromatograph by Perkin Elmer was used. The first step is evacuating the GC with a pump to a pressure below 4 mbar. Argon was used as carrier gas with a 4 m long column (60/80 CarboxenTM 1000). Two bake-out were applied: 65 °C for 16.5 minutes and 150 °C for 6 minutes. Gas sampling tubes were directly attached with the GC. A small amount of gas is removed without the need of a septum. After the measurement the tubes can be used for further analyses (isotope composition).

The instrument houses 3 detectors, a Hot Wire Detector (HWL) and a Thermal Conductivity Detector (TCD) which are working together and a Flame Ionisation Detector (FID). The HWL and TCD are useful for universal detection but with low detection limit (accuracy of 5 ppm).

The FID detector is suitable for carbon analysis (CO, CH₄) with an accuracy of 0.1 ppm.

For the interpretation two chromatograms are available. Four reference gases with known concentrations are used for calibration which were analyzed at the beginning of each day.

To determine the concentrations the peak area were read from the chromatograms except for O₂ where the height of the peak was used. Components that can be analyzed are He, H₂, CO and CH₄ in ppm as well as O₂, N₂ and CO₂ in mol-%.

Analyses at the TUBAF

The TRAACE GC ULTRA by Thermo Scientific houses a Heat Conductivity Detector (HCD) which is specialized on carbon dioxide and oxygen detection and a FID that is used for methane registration.

At the beginning of the measurement three standards with the following mixtures were run for calibration:

- Mix of 1:20 (1000 µl in the head space)
- Mix of 1:40 (500 µl in the head space)
- Mix of 1:80 (250 µl in the head space)

200 µl of sample were injected. One measurement took 8.25 minutes in total. The first 2 minutes the oven heated up to a temperature of 100 °C. Afterwards the temperature further increased to a value of 200 °C (ramp 16 °C/min).

The duration of the measurement for the standards was a bit shorter, in total 3.25 minutes. The first 2 minutes obtained a temperature of 100 °C. Accordingly temperature was increased to 120 °C (ramp 16 °C/min).

3.5 Isotopic Analyses

The analyses of the isotopic composition from water and gas samples were arranged at the INGV in September 2010 as well as at the UFZ in April 2011. At the INGV stable carbon isotopes ($\delta^{13}\text{C}_{\text{CH}_4}$ and $\delta^{13}\text{C}_{\text{CO}_2}$) and noble gas isotopes (He, Ne and Ar) from gas which were sampled in gas sampling tubes (Figure 3-8) were determined. Additionally, the hydrogen ($\delta^2\text{H} / \delta\text{D}$) and oxygen ($\delta^{18}\text{O}$) isotopic signature from water samples was measured. In the UFZ laboratories ($\delta\text{D}/\delta^{18}\text{O}$)-ratio from water samples as well as $\delta^{13}\text{C}_{\text{DIC}}$ from BaCO_3 were analyzed. The isotopic determination from sulfur in water was analyzed from precipitated ZnS and BaSO_4 . Sulfur and carbon isotopic signature was also determined from gas (precipitated ZnS and BaCO_3 ; production of precipitates is explained in Section 3.2.2). In the following the different methods used for the isotopic determination at the INGV and the UFZ are explained. The descriptions are subdivided in isotopic composition of water and gas.

3.5.1 *Isotopic composition of the fluids*

3.5.1.1 *Hydrogen and oxygen isotopic composition*

Analyses at the INGV in Palermo

Measurement of hydrogen and oxygen isotopes at the INGV in Palermo was arranged separately. Facts of the different methods are given below.

➤ $\delta^{18}\text{O}$ in CO_2 (Analytical Precision (AP) 2003 MS)

The preparation of the samples is preceded automatically with the help of a Liquid Handler. An amount of 1 ml of each sample was injected into glass vials. Then the head space was replaced with a gas consisting of 6 % carbon dioxide and pure helium. The gas flow amounted 20 to 25 mL/min which was controlled with a PE 1000 Electronic Flowmeter. After 24 hours the helium and carbon dioxide was equilibrated in the head space (Epstein & Mayeda, 1953) and the analysis of the isotopic signature of the gaseous CO_2 was arranged with the "AP2003 MS". It is an indirect measurement of the oxygen isotopic ratio. Each sample is analyzed three times (control purpose) and a mean value is calculated. The isotopic values are reproduced in δ -notation (per mil units [‰] vs. VSMOW international standard) with an error source of ± 0.1 ‰.

➤ $\delta^2\text{H}$ in H_2O (TC/EA and Finnigan Delta Plus XP MS)

The water samples were filled in 5.9 ml glass vials and sealed with a cap with an integrated septum. An auto sampler took 0.8 μl of the sample and injected the fluid into a carbon reactor (TC/EA from Thermo Finnigan) with temperatures between 1350 °C and 1450 °C. The sample was evaporated and injected in a constant helium gas stream with high vacuum of 10^{-6} bar. This step of analysis is based on a pyrolysis process. Because of the reducing environment and the high abundance of carbon, all oxygen reacts to CO and hydrogen converts to H_2 . In the following step a GC-column separates H_2 from CO and other gases of concern produced during pyrolysis process. The isotopic composition is then measured with a Finnigan Delta Plus XP MS. Each sample was measured 5 times. The measurement inaccuracy is specified with a value of ± 0.5 ‰. This results in a mean value of 5 runs which are displayed in conventional δ -notation (in per mil units (‰) VSMOW, international standard).

Analyses at the UFZ Halle / Saale

Saline samples for stable isotope analysis were treated with a high temperature vacuum-distillation at UFZ Halle / Saale. The equipment used is displayed in Figure 3-10.

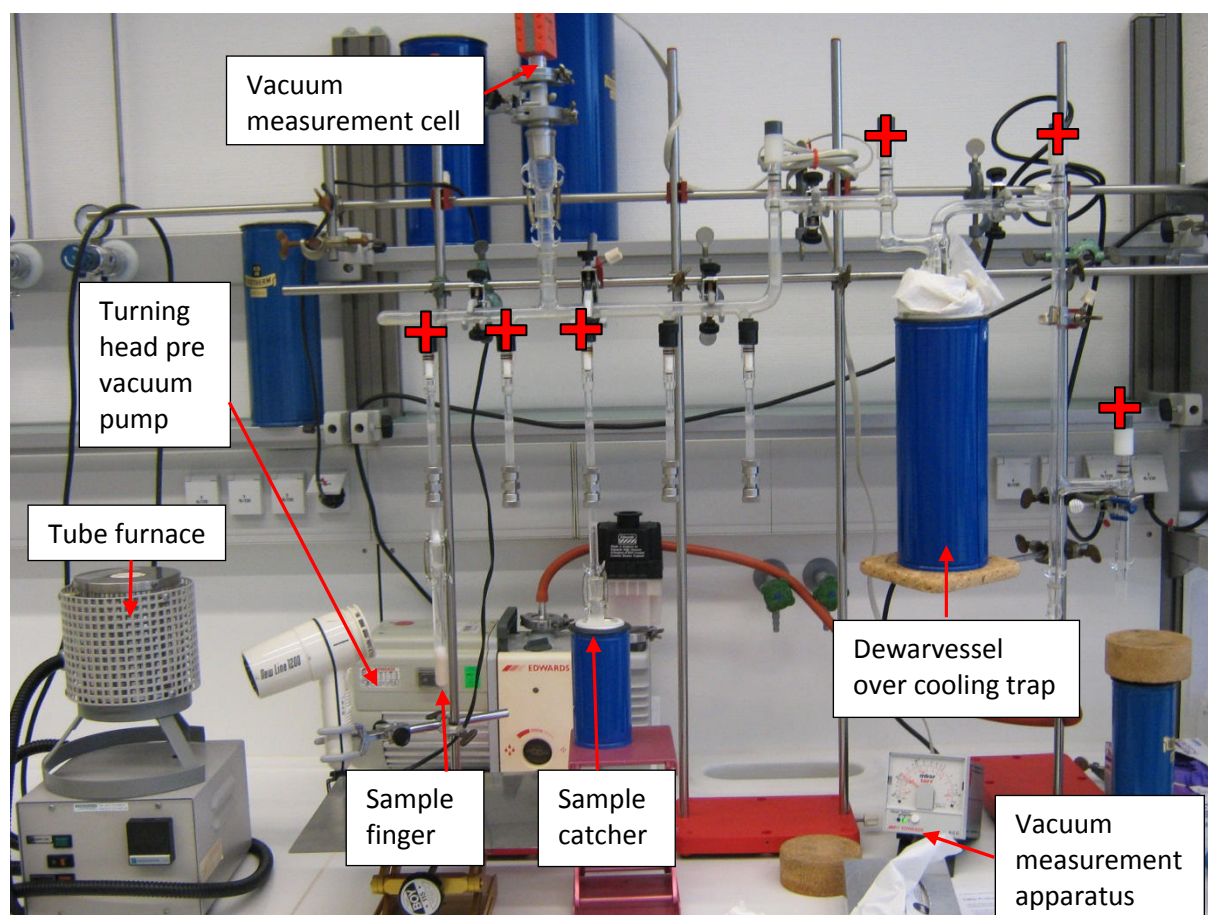


Figure 3-10: High temperature vacuum-distillation apparatus with the marked used valves (red crosses)

The vacuum-distillation apparatus works under a pressure of 10^{-2} bar that is checked continuously with a vacuum measurement cell during the whole procedure. The sample is filled into a sample finger together with quartz sand and quartz wool and heated with a tube furnace. The vapour is caught in the sample catcher which is cooled by a Dewar vessel.

The isotopic composition ($\delta^{18}\text{O}$ and $\delta^2\text{H}$) of the distillate samples were measured with a laser based "Picarro L1102-I" (CRDES: Cavity Ring-Down Spectroscopy) principle. The instrument reads the absorption of laser light caused by the vaporised water sample.

Three reference water standards called PES (water from polar ice, serial number: 16.07.07/64), HAD (distillate water from the UFZ, serial number: 18.07.07/64) and MAST (Mid-Atlantic ocean water, serial number: 17.07.07/47) are used for the measurement to ensure a high accuracy. Further information about the isotopic contents of the reference waters can be found in Table 3-4. At the beginning of each sample batch the isotopic composition from all three reference waters were determined in duplicates. Then each

sample is measured six times whereby the last three measurements are used for further calculations (to avoid memory effects). Only 1 µl of water sample is needed for one measurement. Tolerable variances are assessed for δD with 1.5 ‰ and for δ¹⁸O with 0.4 ‰.

Table 3-4: Isotopic composition of the used standard waters based on SMOW.

Reference water	Isotopic contents (VSMOW) [‰]		
PEST	δD	= - 328.9	(± 1.0)
	δ ¹⁸ O	= - 40.94	(± 0.1)
HAD	δD	= - 59.9	(± 1.0)
	δ ¹⁸ O	= - 9.67	(± 0.1)
MAST	δD	= 1.1	(± 1.0)
	δ ¹⁸ O	= 3.01	(± 0.1)

Measured waters with a high salinity are often determined outside the calibration. Until now there do not exist standard waters given by the IAEA for that kind of problem.

3.5.1.2 Carbon isotopic composition

Analyses at the UFZ Halle / Saale

The analysis of the δ¹³C_{DIC} from water is made over a gas bench by adding phosphoric acid and subsequently measuring the generated CO₂ in the head space. The acid results a low pH (between 0.5 and 1 after Capasso et al., 2005) and the dissolution of all carbon species into the gaseous status. About 0.2 to 0.3 ml of H₃PO₄ is filled in Exetainers® which were cleaned with helium gas before the use. The system is cleaned again with helium before the samples are added. After a time period of two hours all existing carbon consisting in the samples is vaporized to CO₂ into the head space. Afterwards the isotopic ratio of carbon can be measured with a mass spectrometer (Delta V Plus Isotope Ratio MS). Each sample was prepared in duplicates. Standards (KH-2, BaCO₃ N and IAEA CO9) were used for calibration. The results are displayed as TIC versus PDB international standard.

3.5.2 Isotopic composition of the gas

3.5.2.1 Carbon isotopic composition

Analyses at the INGV in Palermo

The instrument used was a Finnigan Trace gas chromatograph (Thermo Scientific). The analysis of 50 µl of one gas sample took approximately 7 minutes. The oven was heated to 50 °C. The column (Rt®-QPLOT™ from RESTEK Chromatography Products) had a length of 30 m and a diameter of 0.32 mm. To detect $\delta^{13}\text{C}$ of methane a column with a length of 60 m and a diameter of 0.32 mm (from RESTEK Chromatography Products) was utilized. Before the analysis of $\delta^{13}\text{C}_{\text{CO}_2}$ the amount of CO_2 was decreased because concentrations between 90 and 99 % are too high. Therefore samples were diluted to a CO_2 concentration of approximately 4 %.

Analyses at the UFZ Halle / Saale

The analysis of $\delta^{13}\text{C}_{\text{DIC}}$ from the precipitate BaCO_3 (production, Section 3.2.2) was made over a gas bench by adding phosphoric acid and subsequently measuring of the CO_2 in the head space. Therefore an amount between 0.4 and 0.6 mg of dry homogeneous BaCO_3 (depending on the reaction with HCl) was filled in Exetainers®. Then the tubes were cleaned with helium, subsequently phosphoric acid was added and after a time period of two hours the head space was analyzed for $\delta^{13}\text{C}_{\text{DIC}}$. The method is similar to the handling with water samples already mentioned in Section 3.5.1.2.

3.5.2.2 Noble isotopic composition: helium, neon and argon

The analysis of noble gases is an extensive process and instruments with a high precision and sensitivity are necessary. Pre process steps in stainless steel ultrahigh-vacuum lines are required to separate the noble gases from other gases. Detectors with a high precision are necessary. In the laboratories at the INGV it is possible to measure the concentration of helium, neon, and argon isotopes in gas samples via mass spectrometer. The principle method is explained below.

The noble gases can be separated from other gases under very low temperatures. Helium starts to condensate at a temperature of 40 K. Neon starts to condensate from the gaseous to the liquid status at a temperature lower than 85 K. In the laboratories at the INGV, reactive species were adsorbed in Zr-Al- getter pumps. Noble gases (argon, helium and neon) were separated by charcoal traps which were cooled to a temperature of 77 °C with the help of liquid nitrogen. (Nuccio et al., 2008) Helium and neon were concentrated in a further charcoal trap with a cryogenic pump at a temperature of 12 °C (neon and argon are in a liquid aggregate status). Then the initiation of helium and neon isotopes was carried out via a mass spectrometer (Helix MCT). With the help of a temperature sensor the release of different noble gas species was controlled. Helium was admitted at 40 °C and neon at a temperature of 85 °C.

Helium and neon isotopes were measured with two different detectors. The AXF detector registered the concentration of ^4He and ^{22}Ne in the gas. The other detector was specialized on the measuring of ^3He , ^{21}Ne and ^{22}Ne isotopes that occurred in very small amounts. The second detector was working with a higher accuracy than the AXF detector. The concentration was determined using peak height. The analysis of noble gases started with the measurement of the neon isotope baseline. Then the detection of neon isotopes followed. After a cleaning run the baseline of helium was registered and the helium isotope determination succeeded. Figure 3-11 shows parts of the apparatus in the laboratory.



Figure 3-11: Top: Pre-cleaning steps for helium and neon isotope measurements. Bottom: Mass spectrometer Helix MCT and the detectors to register noble gas isotopes.

Argon gas could not be handled with the same pre cleaning steps that were used for the other two noble gases. The reason is the condensation of argon on nitrogen. But it could be solved by heating the system to a temperature of 20 °C (room temperature). Thus, the $^{39}\text{Ar}/^{40}\text{Ar}$ isotopes that were previously adsorbed on the charcoal traps could then be analysed with a multi-collector mass spectrometer (Argus by Thermo Scientific). Figure 3-12 shows the pre cleaning step of argon from other gases in the laboratory.



Figure 3-12: Pre-cleaning step of argon isotopes from other gases.

Results were shown in concentration versus time diagrams. The point of interest was the intersection point with the ordinate (time 0), because of the neutralisation of the gas in the magnet during the measurement. Electrons cumulated and neutralised the gas during this time. So the searched initial concentration was decreasing after time.

For further calculation of the concentrations it was necessary that the amount of injected gas sample was known. The injected amounts of each gas sample for helium and neon isotopic analysis is listed in Table A 3. Concentrations in each sample were then calculated in ppm for helium, neon, and argon.

Analytical source of error in air standard are in general below 1 % for helium isotopes and below 0.1 % for argon isotopes (Nuccio et al., 2008).

3.5.3 Sulfur isotopes in water and gas

The determination of the $\delta^{34}\text{S}$ isotopic composition at the UFZ was performed with an Isotope-ratio mass spectrometer system (IRMS) in a continuous flow. The instrument used was a DeltaS from Thermo Finnigan. The standard deviation for multiple readings is about 0.3 ‰. A detailed description about the principle laboratory methods can be found in Robert Sieland (2009). Figure 3-13 displays the distillation procedure, the preparation step before the analytical analysis. The preparation of Acid Volatile Sulphur (AVS) is shown on the left picture, where a precipitation in zinc-acetate solution is created. The Chromium reducible sulphur (CRS) process is illustrated, on the right image which was used to prepare the sulfur isotopic measurements of bio samples.



Figure 3-13: Kjeldahl distillation procedure: On the left AVS, on the right CRS with Chrom III.

4 RESULTS AND EVALUATION

4.1 Thermodynamic parameters

Most of the thermodynamic measurements were taken at “La Calcara” and “Area 26”. The measuring points were selected especially on hot spots which are in most cases visible by white bacteria mats. Each point was measured simultaneously with the heat flux plate and the temperature gradient sensor. The thermal conductivity sensor could be used for two runs only because of a defect of the device which could not be fixed.

4.1.1 *Heat flux*

The first measured heat fluxes are shown in Figure 4-3 and Figure 4-4. After a time period of approximately 400 seconds a constant heat flux was established. An overview of all monitored heat fluxes (and the corresponding calculated heat fluxes) can be seen in Table 4-2. Besides measuring the heat fluxes, it is also possible to calculate the heat flow based on the temperature gradient in the sediment resulting from conduction and convection. A schematic visualization of this approach is shown in Figure 4-1. Calculations for two cases (natural convection on horizontal surfaces and conduction in sediment) and ways of interpretation and comparing with the measured heat fluxes are described in the following paragraphs.

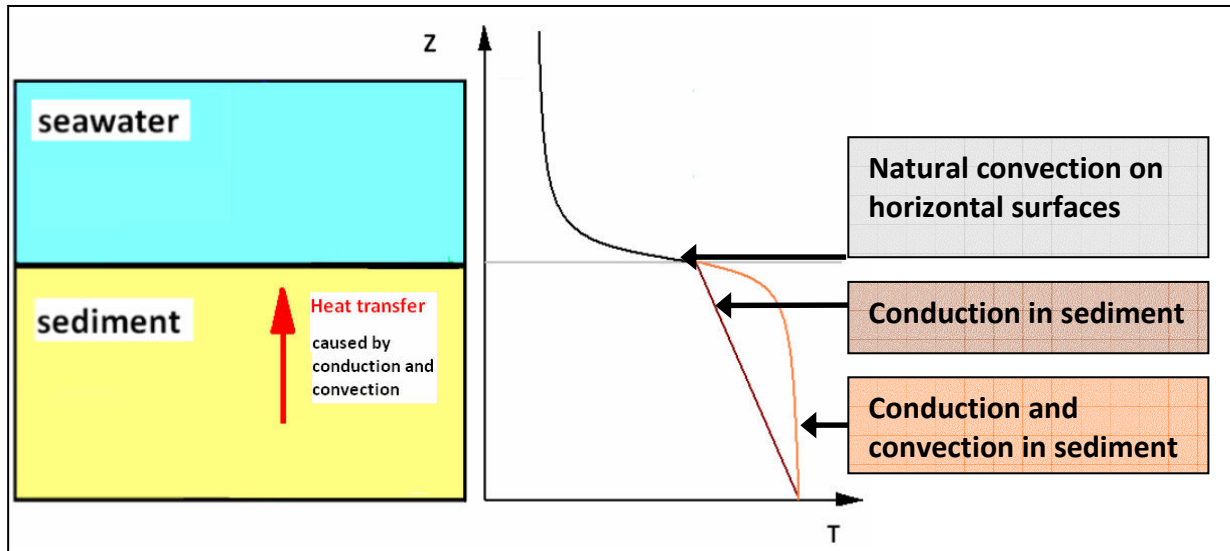


Figure 4-1: Schematic visualization of the regions where heat fluxes can be calculated based on measured temperature gradients, water and sediment surface temperatures. Temperature curves indicate the progression considering heat transfer caused by conduction and conduction/convection. Convection can be generated by hot water.

A) Conduction in the sediment

The determination of heat fluxes in sediment resulting by conduction can be easily calculated with the help of the heat flux equation [4.1] after Fourier.

$$\dot{q} = \lambda_{\text{sediment}} \cdot \frac{\Delta T}{\Delta z} \quad [4.1]$$

whereas: \dot{q} = Heat flux density [W/m²]

$\lambda_{\text{sediment}}$ = Thermal conductivity in the sediment [W/(m*K)], here 1.1 W/(m*K)

ΔT = Temperature difference between the thermo couples [K]

Δz = Altitude differences between the thermo couples which were used for the calculation [m]

The heat conductivity λ which is a material constant has to be determined. In the following calculation, a λ of 1.1 W/(m*K) for saturated sand was used based on literature specifications. This value is multiplied with the calculated geothermal gradient taken from the temperature differences between the thermo couples (Table 4-3 in Section 4.1.2). In some cases the measured temperature gradients show a linear progression whereby recordings especially taken in “La Calcara” (no. 1, 5, 6) feature a parabolic trend. Some temperatures from the upper thermo couple (sediment depth of 50 mm) recorded strong variances compared to the other three related temperatures. Possible reasons are described

in Section 4.1.2. Nevertheless, a precise temperature gradient can not be defined. However, the following calculations are made with all recorded temperatures recorded of each thermo couple which was inserted into the sediment. Therefore, temperature differences between the thermo couples are used. In one location (“La Calcara”, no. 5) it was not possible to recess the sensor completely into the sediment. This was taken into account during the calculations of the temperature and altitude differences. The temperature gradients used at this point are shown in Table 4-3 (TC1-TC4, bold). The results of the conduction calculation are summarized in Table 4-2.

If assumed temperature gradients are higher than the real occurring temperature gradients then the calculated conductive heat transport is overestimated and vice versa.

The calculations performed with the heat flux equation [4.1] take conduction into consideration but do not mind heat transfer caused by convection. In contrast to the calculated results, the measured heat fluxes are influenced by particle and mass flow rates resulted from upwelling hydrothermal waters in some locations. That is the reason for the much higher monitored heat fluxes compared to the calculated conductive heat fluxes.

B) Convection towards horizontal surfaces

The determination of heat convection towards horizontal surfaces is a complex calculation. Therefore, a model was created by Gerald Barth. The first step calculates the thermophysical properties for pure water (density, specific heat capacity, heat conductivity, kinematic viscosity, thermal diffusivity, Prandtl number and expansion coefficient) based on the measured water temperature (in general 21 °C (temperature between 0 and 100 °C). The second step calculates the Rayleigh number (Ra) (corresponding formula shown in [4.2]) based on the Grashof number (Gr) multiplied with the Prandtl number (Pr). These numbers are calculated based on chemical data for the specific water temperature (equations [4.3] and [4.4]).

$$Ra = Gr Pr = \frac{g \beta}{\nu a} (T_{\text{sediment surface}} - T_{\text{water}}) x^3 \quad [4.2]$$

$$Gr = \frac{\beta g \Delta T x^3}{\nu^2} \quad [4.3]$$

$$Pr = \frac{\nu}{a} \quad [4.4]$$

whereas: Ra = Rayleigh number
 Gr = Grashof number
 Pr = Prandtl number
 g = Acceleration due to gravity (9.81 m/s²)
 β = Thermal expansion coefficient [1/K]
 $(T_{\text{sediment surface}} - T_{\text{water}})$ = Difference between surface and water temperature
 ν = Kinematic viscosity [m²/s]
 a = Thermal diffusivity [m²/s]
 x = Characteristic length based on the dimension of the heat flux plate, here 0.03

Based on the value of the Rayleigh number (ranging from 10⁴ to 10⁷ and 10⁷ to 10¹¹, respectively) the Nusselt number can be calculated (formula [4.5] and [4.6]). The formula for the Nusselt number leads to the heat transfer coefficient (α). The last step is the evaluation of the heat flux with equation [4.7] that integrates α and the temperature difference between water and the sediment surface.

$$Nu = \frac{\alpha * s}{\lambda_{\text{Water}}} = 0.54 Ra_s^{1/4} \quad \text{for} \quad 10^4 < Ra_s < 10^7 \quad [4.5]$$

$$Nu = \frac{\alpha * s}{\lambda_{\text{Water}}} = 0.15 Ra_s^{1/3} \quad \text{for} \quad 10^7 < Ra_s < 10^{11} \quad [4.6]$$

whereas: Nu = Nusselt number
 α = Heat transfer coefficient [W/(m²/K)]
 s = area(plate)/perimeter(plate) = 30 mm
 λ_{Water} = Thermal conductivity of the fluid [W/(m*K)]

$$\dot{q} = \alpha (T_{\text{sediment surface}} - T_{\text{water}}) \quad [4.7]$$

It is possible to estimate the calculated convection into natural or forced convection depending on the amount of the heat transfer coefficient (α). Forced convection is the moving of a fluid resulting by pressure differences. The flow of particles is stimulated by external impacts. In contrast, natural convection is the flux of a liquid because of a temperature gradient. On a macroscopic scale the fluid can be accepted in a static condition.

The heat transfer coefficient can give an estimation of natural and forced convection occurrence. Its spectrum is shown in Table 4-1. If α exceeded $800 \text{ W}/(\text{m}^2\text{K})$, the occurring of forced convection can be assumed.

Table 4-1: Type of convection according to the heat transfer coefficient (α) and the corresponding calculated sediment surface temperatures with constant water temperature based on the model for “Convection on horizontal surfaces”.

Fluid and state of movement	α [$\text{W}/(\text{m}^2\text{K})$]	T_{water} [$^{\circ}\text{C}$]	T_{surface} [$^{\circ}\text{C}$]
Water in natural convection	200 ... 800*	21	> 21 to 68
Water in forced convection	600 ... 10 000*	21	> 45 to 93 300

* source: Script: Grundlagen der Wärme- und Stoffübertragung, TU Bergakademie Freiberg – 2006/09/27, appendix, p.131

With a water temperature of 21°C and a sediment surface temperature between 45°C and 68°C we assume a mixture between natural and forced convection. For higher temperatures than 68°C we suppose a domination of forced convection. For sediment surface temperatures between $> 21^{\circ}\text{C}$ and 45°C we assume natural convection. These temperature ranges are assumptions to provide an idea about the occurring of natural and forced convection.

The calculation's major problem is the exact determination of the sediment surface temperature with measured heat fluxes and temperature gradients. The temperature gradient sensor was deployed in various depths. The first thermo couple below the sediment surface was normally situated in the depth of 50 mm. With the help of the resulting temperature graphs as shown in Figure 4-6 and Figure 4-7, it is possible to estimate the temperature on the sediment surface by linear regression. In Figure 4-2 a trend line of the resulting surface temperature is exemplarily added to the temperature measurement curve (parabolic) of “La Calcara”, number 6. The variability of the recorded values illustrates the difficulty to assume the real sediment surface temperature.

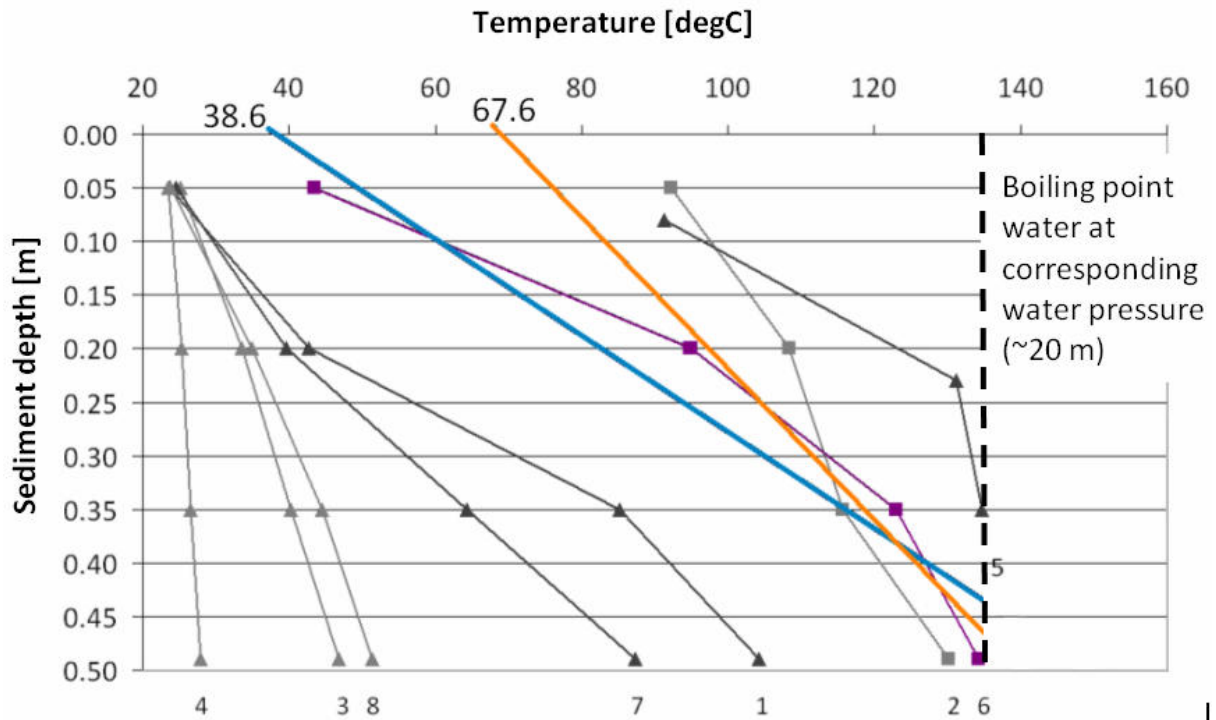


Figure 4-2: Method to calculate the sediment surface temperature based on the temperature gradient measurements (here, “La Calcara”). Therefore a linear regression was conducted (example, no. 6). The blue-coloured trend line regards temperatures from all four thermo couples and results in a sediment surface temperature of 38.6 °C. The orange trend line attends the upper three thermo couples and causes a sediment surface temperature of 67.6 °C.

Condition for heat transport from the earth’s interior to its surface is a decreasing sediment temperature to the surface and a colder water temperature compared to the deposited material. Otherwise a heat transport from the deep to the surface is not possible (second law of thermodynamics, Figure 4-1).

For future investigations it is important that a detailed documentation about the appearance of the sediment surface (planar or hilly) as well as of the vegetation and stones is given. A photo documentation can be useful.

Table 4-2: Overview of the measured and calculated heat fluxes whereby conduction is calculated by the heat flux equation [4.1].

No.	Location	measured \dot{q} [W/m ²]	Conduction: calculated \dot{q} [W/m ²]
1	P21	470	- *
1	BP	94**	- *
1	Area 26	1250	32
2	Area 26	800	6
3	Area 26	1010	100
4	Area 26	1050	27
5	Area 26	670	39
1	La Calcara	105	202
2	La Calcara	2500**	95
3	La Calcara	1440	54
4	La Calcara	20	11
5	La Calcara	365	165
6	La Calcara	165	227
7	La Calcara	108	157
8	La Calcara	30	69

* No temperature gradient sensor measurements available

** Overrange; increasing not finished

*** Sediment surface temperature lower than water temperature of 21 °C

Results of the measured heat fluxes and corresponding calculated heat fluxes are illustrated in Table 4-2. Calculated conductive heat transfer (range between 6 and 225 W/m²) show much lower values compared to the measured heat fluxes which alternate between 30 and more than 2500 W/m². It can be assumed that the occurring measured heat fluxes are a combination between a heat transfer caused by conduction as well as forced and natural convection.

For future studies it is important that the measuring sensors (heat flux plate and temperature gradient sensor) are recording exactly the same point because the hydrothermal system (upwelling hot gases and fluids) influence the measurement dramatically. Only then measured and calculated heat fluxes are better comparable.

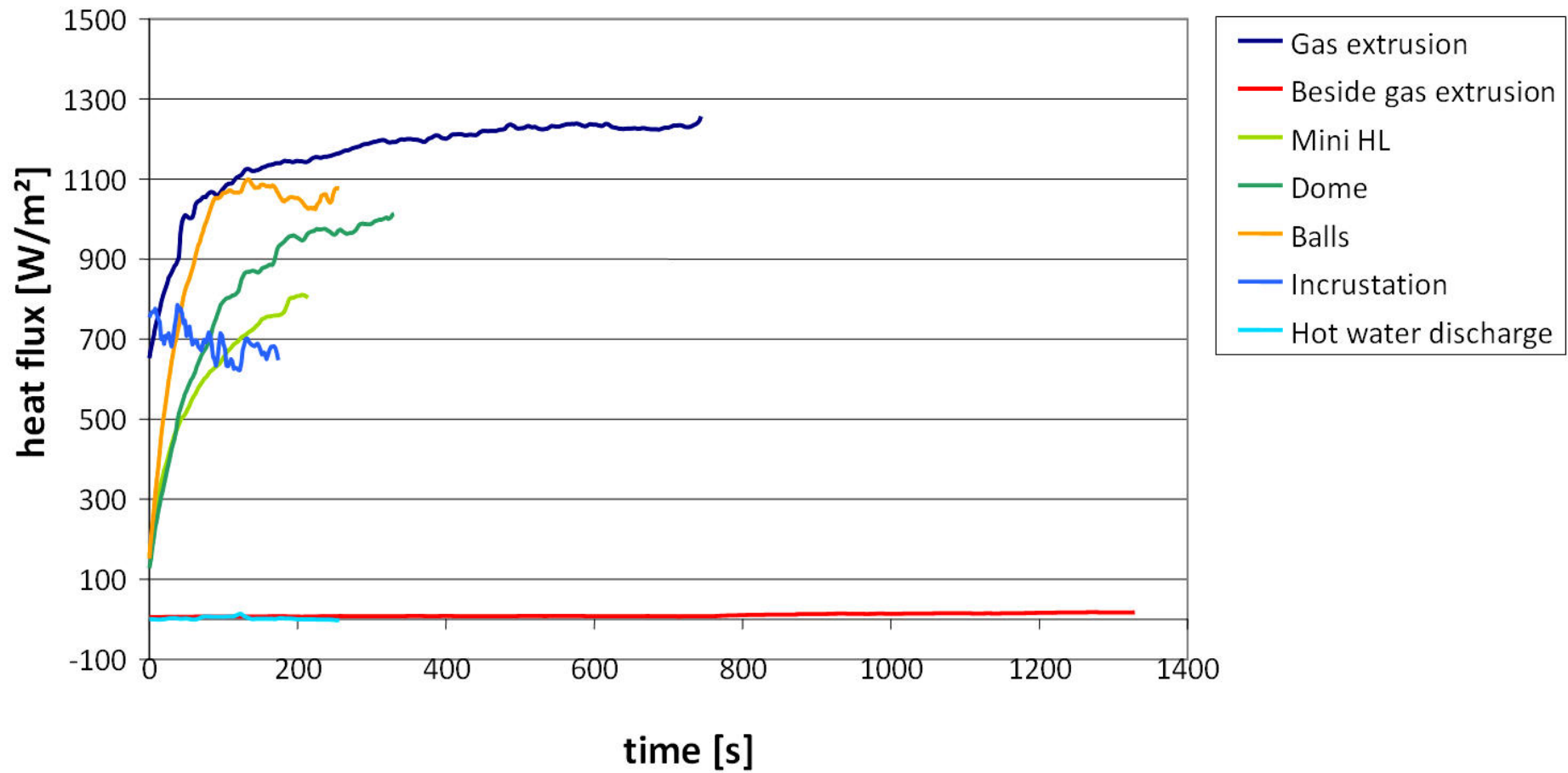


Figure 4-3: Heat flux measurements, "Area 26"

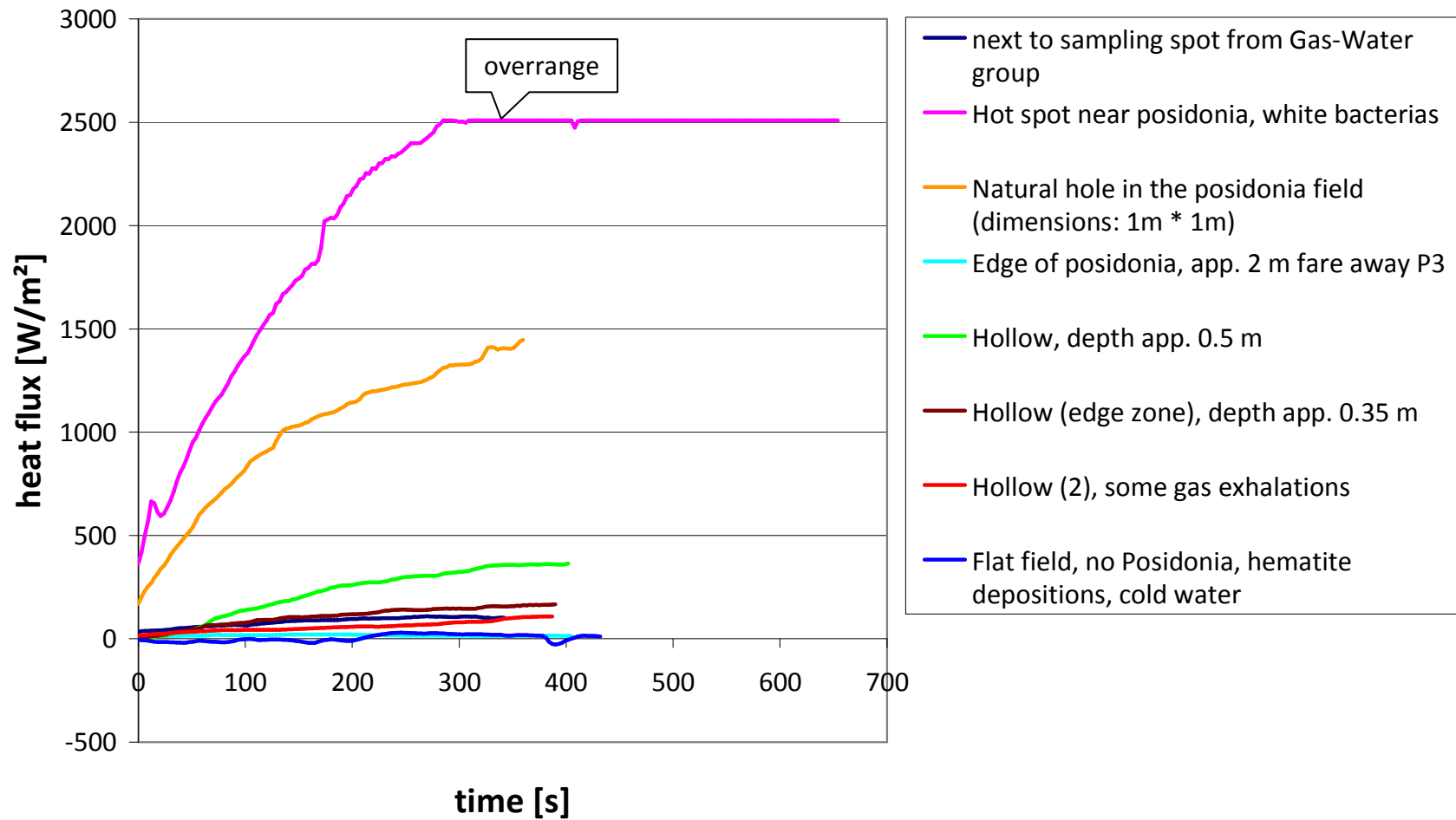


Figure 4-4: Heat flux measurements, “La Calcara”. Errors in measurement for breakpoint ‘Flat field, no Posidonia, hematite deposition, cool water’ (blue line). It is thermodynamically not possible to gauge negative heat fluxes because it is no possible to transport heat from cold to hot places (second law of thermodynamics).

4.1.2 Temperature gradient

First measurements with the temperature gradient sensor show that after a duration of 300 seconds the sensor has adapted to the temperatures of the environment. After this time period the real temperatures of the sediment can be read on the temperature logger PCE T-390 for the different depths. When these temperatures are achieved, the measurement can be stopped and a new measurement at another point is possible. Figure 4-5 shows exemplary a temperature progression with an end temperature gradient of 24.9 K/m after this time period. The temperature gradient can be calculated using equation [4.8].

$$\text{Gradient } T = \frac{\Delta T}{\Delta z} \quad [4.8]$$

whereas: *Gradient T = Geothermal temperature gradient [K/m]*
 ΔT = Temperature difference between the deepest and lowest TC to the sediment surface (normally TC1 and TC4) [K]
 Δz = Sediment depth [m], here: Δz (TC1-TC4) = 0.42 m; Δz (TC2-TC4) = 0.27 m

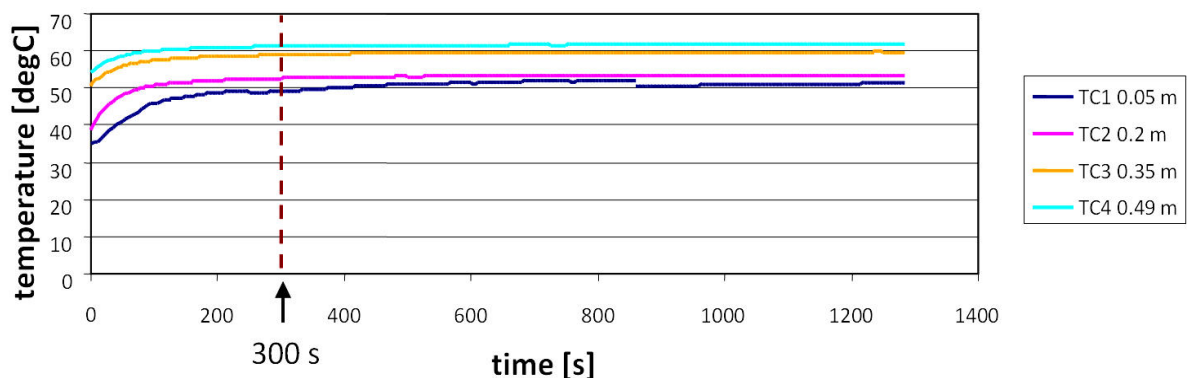


Figure 4-5: Measurement with the temperature gradient sensor in “Area 26”. It shows that after a time period of app. 300 sec constant temperatures in all four thermo couples are achieved that typify the real temperature in the different sediment depths.

A series of measurements were made at the locations “La Calcara” and “Area 26”. The temperature gradients are plotted in ΔT - Δz -diagrams, seen in Figure 4-6 and Figure 4-7. The corresponding calculations of the temperature gradient are recorded in Table 4-3. In this process, the temperatures which are highlighted in grey are not implicated in the calculations (TC1). The reason is a not sufficiently thick sediment layer so that the sensor

could not plunged completely into the sediment. Another reason could be the high influence of the surrounding seawater which falsifies the temperature measurements close to the sediment surface. This impact was increased by forced convection caused by divers in the vicinity.

The curve progressions of Figure 4-6 and Figure 4-7 give an imagination of the occurrence of conduction and convection. If the curves are relatively linear which means that the temperature increases with increasing sediment depth. Then it can be assumed that heat fluxes results from conduction. If the curve shows an exponential progression of the temperature with increasing sediment depth (up to a boundary value) it can be assumed that convection occurs. Measurements made in "La Calcara" (curves 1, 2, 5 and 6) show the influence of convection. Measurements made at cooler spots (curves 3, 4, 7 and 8) indicate a temperature gradient that is only supposably generated by conduction.

To get a solid evidence of the temperature gradient for these locations it would be necessary to read temperatures in deeper depths as well because the sensor used reads the temperature gradient in the first half a meter and the influence of forced convections (divers and current) might be high. However, in most places of the submarine caldera of Panarea the thickness of the sediment at the sea bottom is even less than 0.5 meter.

Some recordings for example "Area 26" no. 1, 3, 4, 7 and 8 and "La Calcara" no. 3 and 5 indicate a high influence of the surrounding medium water which falsifies the temperature measurements close to the sediment surface (TC 1). This impact can be increased by forced convections caused by divers or water currents.

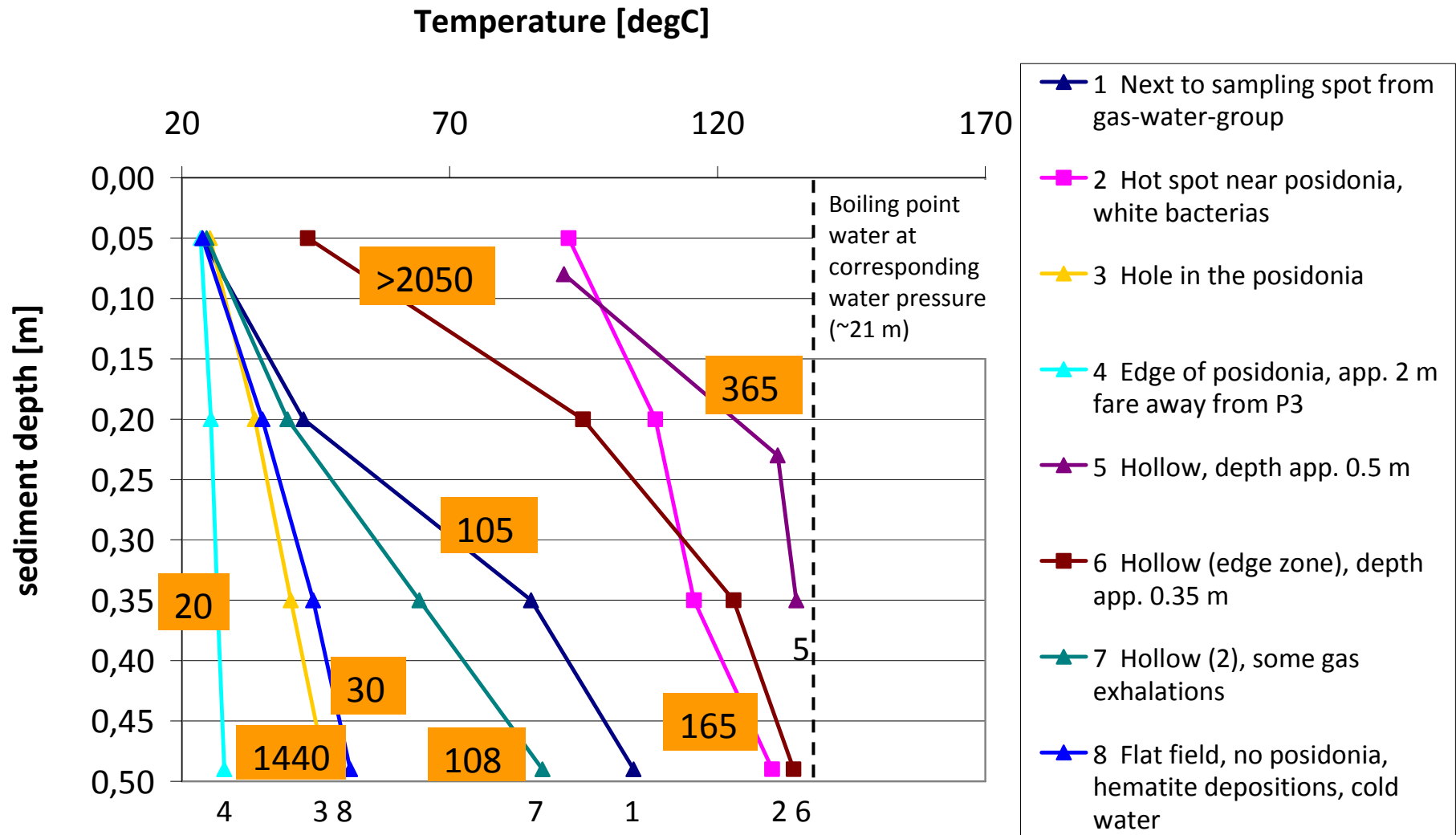


Figure 4-6: Temperature gradients at location „La Calcara” with the associated measured heat fluxes in W/m²

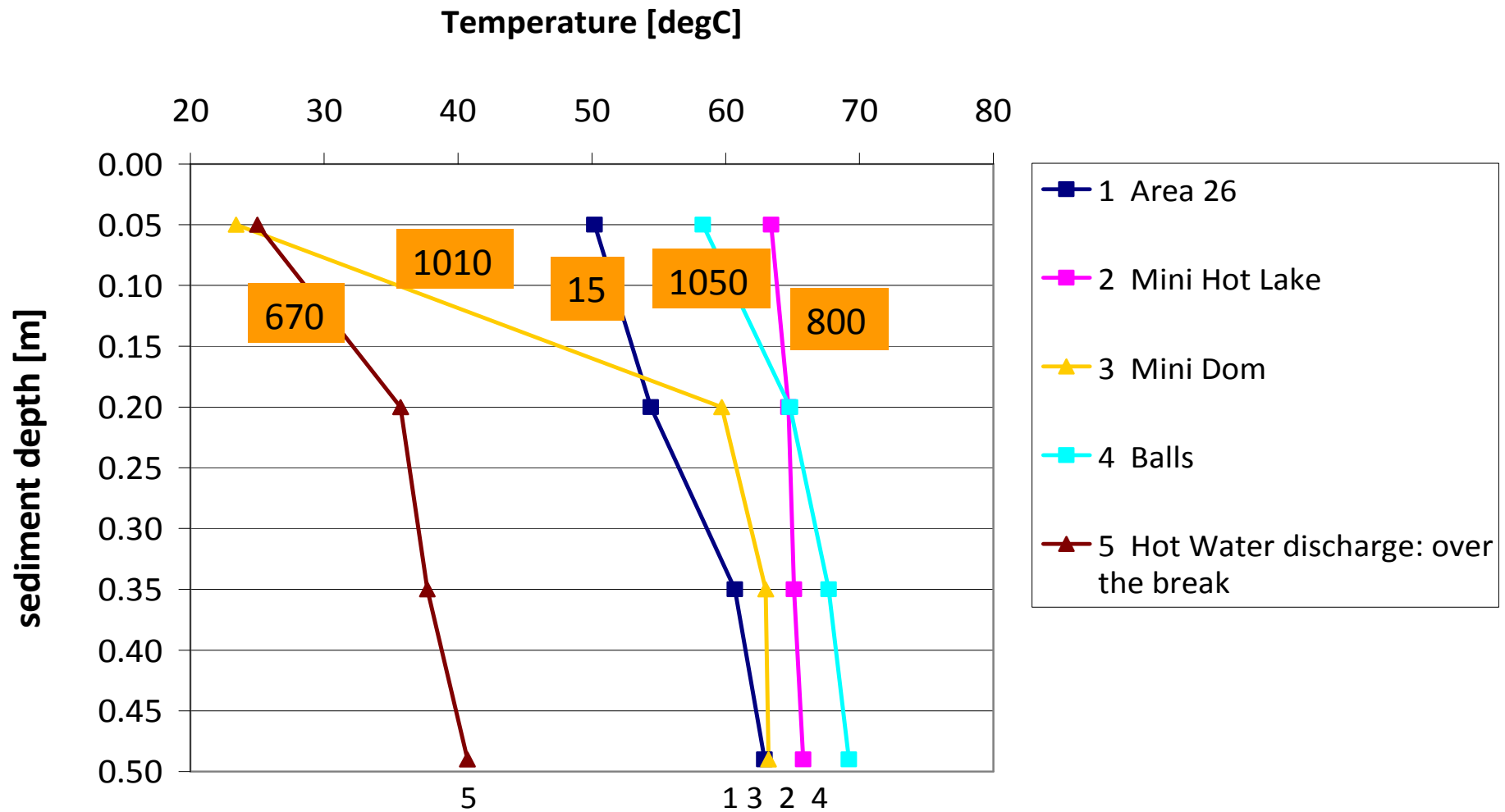


Figure 4-7: Temperature gradients at location "Area 26" with the associated measured heat fluxes in W/m² (Boiling point water at corresponding water pressure (~26 m) app. 140°C)

Table 4-3: Measured temperatures with temperature gradient sensor. In some measurements the sensor could not recess completely into the sediment whereby the first thermo couple was not in the sediment but measured the water temperatures. These temperatures are marked grey in the table. Temperature gradients which were used for further calculations (4.1.1) are highlighted bold.

No.	Location	Location description	TC 1	TC 2	TC 3	TC 4	gradient $\Delta T/\Delta z$ [K/m] between		
							TC1-TC4	TC2-TC4	TC3-TC4
1	Area 26	Area 26	50.2	54.4	60.7	62.9	28.9	29.3	15.7
2	Area 26	Mini Hot Lake	63.4	64.7	65.1	65.8	5.5	3.8	5.0
3	Area 26	Mini Dom	23.4	59.7	63.0	63.2	90.5	12.1	1.4
4	Area 26	Balls	58.3	64.8	67.7	69.2	24.8	15.2	10.7
5	Area 26	Hot Water discharge: over the break	25.0	35.7	37.7	40.7	35.7	17.2	21.4
6	Area 26	Hot Water discharge: horizontal measurement*	23.1	24.5	35.9	38.3	34.5	47.6	17.1
1	La Calcara	Near sampling spot from Gas-Water group	23.7	42.7	85.2	104.3	183.2	212.4	136.4
2	La Calcara	Hot spot near Posidonia, write Bacteria	92.2	108.4	115.6	130.2	86.4	75.2	104.3
3	La Calcara	Natural hole in the Posidonia	25.2	33.6	40.3	46.8	49.1	45.5	46.4
4	La Calcara	Edge of Posidonia, app. 2 m away from Point 3, hematite deposition	23.5	25.4	26.6	27.9	10.0	8.6	9.3
5	La Calcara	Hollow, depth app. 0.5 meters	21.5	91.3	131.2	134.7	257.3	149.7	25.0
6	La Calcara	Hollow (edge zone), depth app. 0.35 meters	43.5	94.9	123	134.2	206.1	135.5	80.0
7	La Calcara	Hollow (2): some gas exhalations, flat	24.6	39.7	64.3	87.3	142.5	164.1	164.3
8	La Calcara	Flat field, no Posidonia, hematite depositions, cold water	23.8	35	44.5	51.4	62.7	56.6	49.3

* Not displayed in the Figure 4-6 because the sensor was used horizontally and many divers around: therefore high water circulation and bad accuracy

4.1.3 Thermal conductivity

During the expedition in 2010 the thermal conductivity sensor was used for three measurement series, two in “Bottaro West” and one in “Area 26”. Throughout the use of the thermal conductivity sensor the heat-up phase and the cool-down phase was monitored (Figure 4-8, top). The heater was activated for five minutes which was found to be sufficient during calibration experiments (3.1.4). A constant voltage of 2.6 V and a constant amperage of 24.25 A was applied and documented during the whole measurements. After these time period the heater was turned off and the temperature in the sensor decreased very fast.

For further calculations it is important to evaluate the temperature increasing during the heat-up phase in the t - θ -diagram (Figure 4-8, bottom). The increase relates to the heat conductivity λ . For further conclusions laboratory experiments and numerical models are needed.

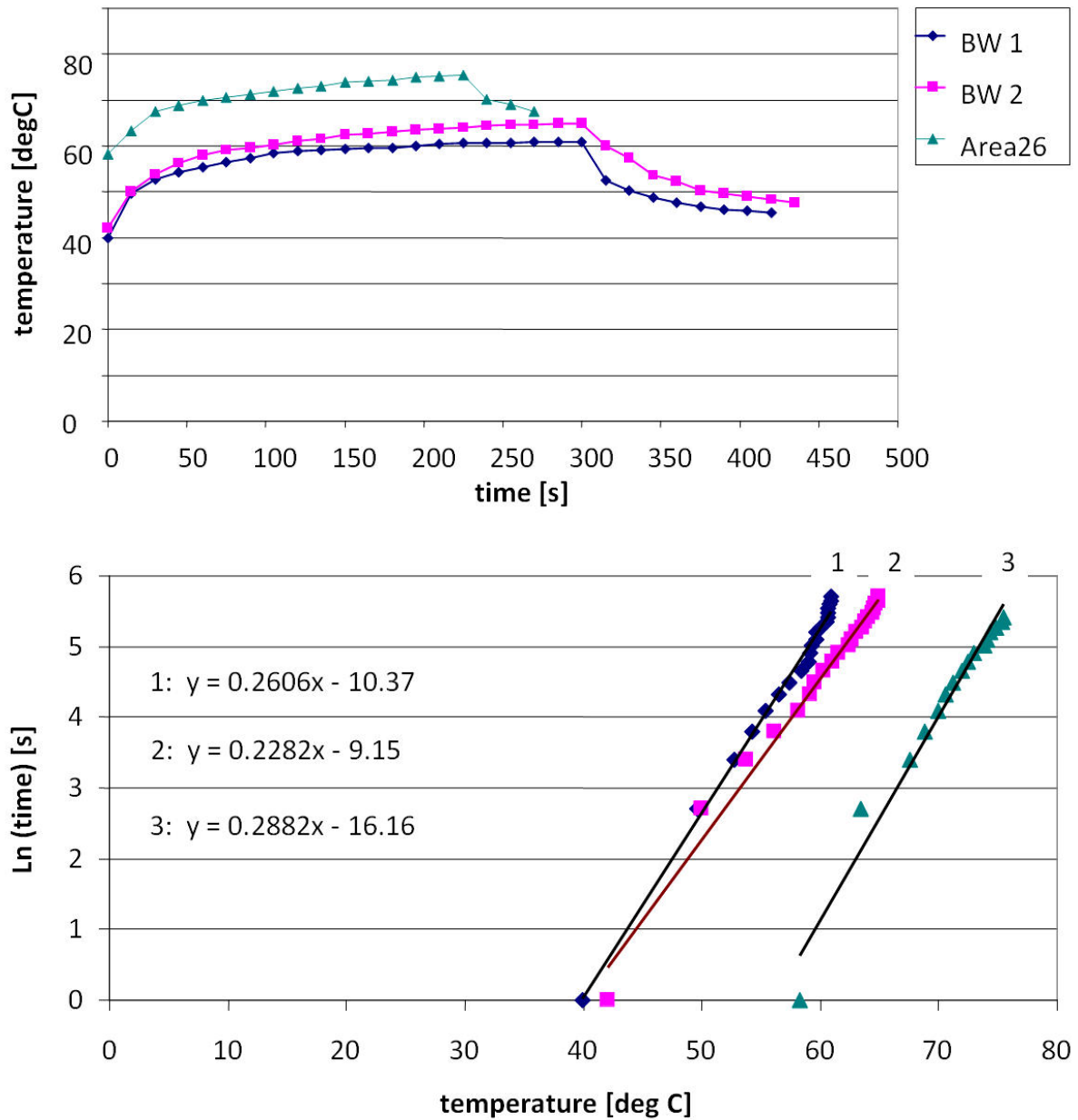


Figure 4-8: Top: Measurements with the thermal conductivity sensor made in “Bottaro West” (06.09.2010) and “Area 26” (07.09.2011). Bottom: Corresponding Ln(time)-temperature-diagram, shows the heating phase and the equation of the added trend line. Slope of the trend line is important to solve the equation [4.9] and to get the thermal conductivity.

The increasing temperature of the heating element during the heating phase depends on the thermal conductivity of the surrounding material. Because of the known applied heating power (P) which is the product of voltage and amperage and the temperature increasing during a defined time period, the thermal conductivity can be determined (equation [4.9]).

For further calculations it is assumed that the diameter of the heating element is very small and thus negligible. Additionally assumptions are isotropic sediments, an infinite extension of the surrounding sand, sufficiently long time periods, constant temperatures at the beginning of the measurements ($T(t=0) = T_0 = \text{const.}$) and temperature independently from thermophysical properties (Wulf, 2009). Under these assumptions the calculation of the thermal conductivity can be arranged with equation [4.9] that can be found in the VDI code (4640-2).

A calculation example of the first measurement made in “Bottaro West” (BW 1) is presented here. Table 4-4 gives an overview of the resulted thermal conductivities from the field measurements.

$$\lambda = \frac{\ln\left(\frac{t_2}{t_1}\right)}{T_2 - T_1} \cdot \frac{P}{4 \pi L} \quad [4.9]$$

whereas: λ = Heat conductivity [W/(m*K)]
 $\ln(t_2/t_1)$ = natural logarithm of the quotient from the time intervals
 $T_2 - T_1$ = Temperature difference [K], here: $r \rightarrow \infty$, $T = T_0 = \text{konst.}$
 P = Heating power, $P = U \cdot I$ [V · A]
 L = Length of the heating filament which recessed into the sediment, here: 1.24 m

$$\lambda = 0.2606 \cdot \frac{1}{\text{K}} \cdot \frac{2.6 \text{ V} \cdot 24.25 \text{ A}}{4 \pi \cdot 1.24 \text{ m}}$$

$$\lambda = 1.054 \frac{\text{W}}{\text{m K}}$$

Table 4-4: Calculation of the thermal conductivity with the use of equation [4.9] based on the field measurements. A constant voltage of 2.6 V and a constant amperage of 24.25 A was applied.

Location	Ln (t_2/t_1)	λ [W/(m*K)]
BW 1	0.2606	1.054
BW 2	0.2282	0.923
Area 26	0.2882	1.167

Effect of errors during the field measurements can be seen in the logarithmic progression in Figure 4-8. Measuring points outside the trend line indicate error factors (for example diameter of the heating element, temperature variations, anisotropic sand etc.). Nonetheless the measured thermal conductivity during the three field experiments which are shown in Table 4-4 yielded a mean λ -value of 1.048 W/(m*K). Laboratory experiments with the thermal conductivity sensor in saturated sand (Cerabeads) appropriated a thermal conductivity of 1.086 W/(m*K) (Urbanik, 2011). Results from the field and the laboratory experiments show no significant variations which indicate a good accuracy of the measuring device. In VDI-“Wärmeatlas”, results from Kirscher (1934) are shown thermal conductivities depending on different porosities for different moisture contents (Figure B 2). The results indicate that increasing porosity causes a strong increasing of thermal conductivity. Additionally, the thermal conductivity increases with increasing water concentrations because gases have a lower λ related to water (Hopmans & Dane (1986), Sundberg (1988)). The total porosity of mid-grained sand can be estimated with 45 % (Chuhan et al., 2002). Therefore in saturated conditions a thermal conductivity of approximately 2.2 W/(m*K) can be assumed which is twice as high than results from the field and the laboratory. Thus it is obvious that the porosity of the sediment has a high influence on the thermal conductivity (Großmann (1993), Smits et al. (2010)).

To make more detailed conclusions about the thermal conductivity in the investigation area representative sand samples for future laboratory experiments have to be taken. Therefore particle size analyses and more thermal conductivity measurements should be performed. Other parameters that might be interesting and should be recognized in future assignments are pressure and temperature changes (Krischer (1934), Halisch & Tietze (2005), Sundberg (1988)).

4.1.4 Calibration of the sensors

➤ Temperature gradient sensor

The outcome of the experiment show that after a time period of approximately 150 seconds all four thermo couples adapted to the surrounded heated water temperature (Figure 4-9).

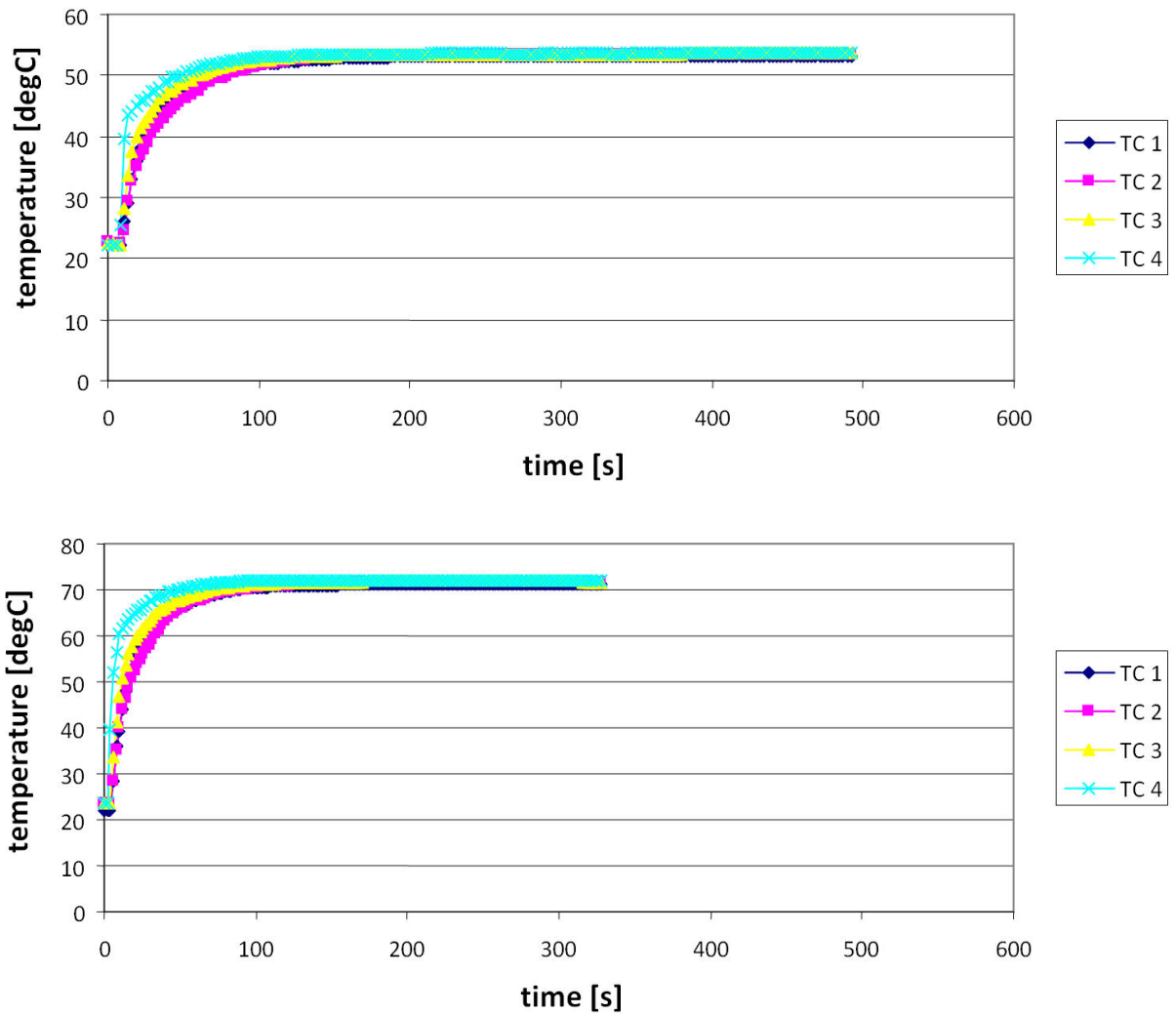


Figure 4-9: Calibration of the temperature gradient sensor to the temperature equilibrium in heated water (53 °C, top and 73 °C, bottom). Temperature equilibrium was achieved from all four TCs after a time period of app. 150 sec.

Additionally, it is obvious that no significant time differences for temperature equilibrium between the hotter and colder water temperature could be achieved.

Calibrations of the temperature gradient sensor before and after the field experiments determined that no differences in the accuracy of measurement occurred. So, it can be assumed that the measured temperatures during the expedition show the real temperature values in the different depths.

➤ Thermal conductivity sensor

Results of the first experiment where temperature adjustments for 50 °C and 65 °C during a constant voltage of 12 V and a constant amperage of 1.27 A were tested are shown in Figure 4-10.

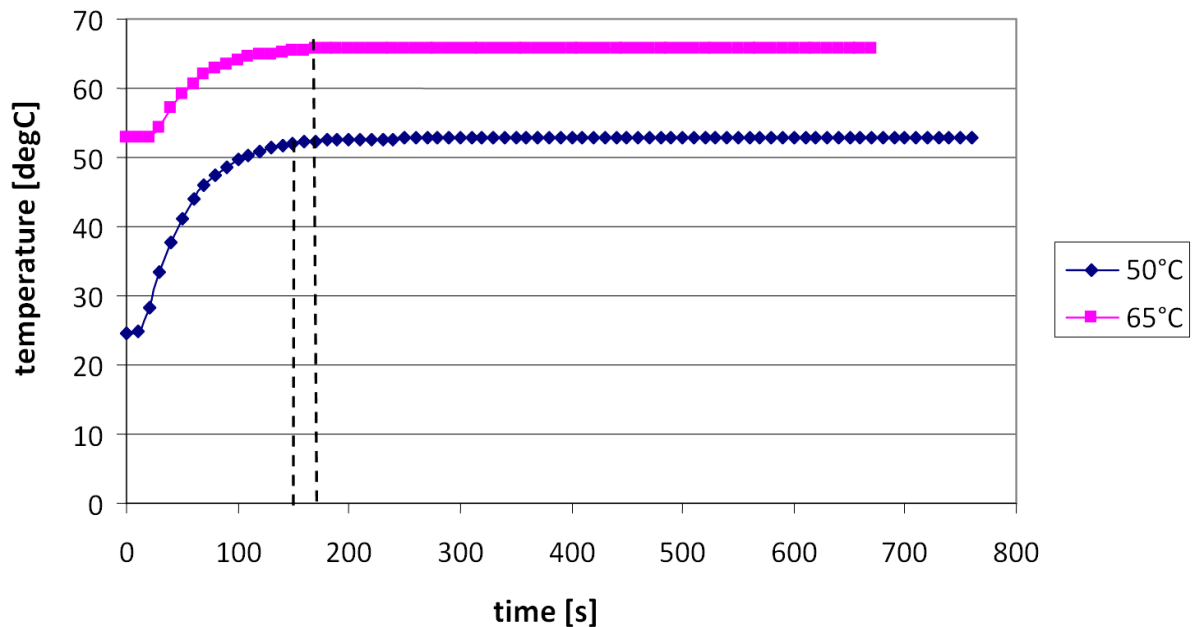


Figure 4-10: Results of the laboratory experiment to measure the temperature adjustment to the surrounding area for different temperatures (50 °C and 60 °C) during constant voltages and amperages. After a time period of 150 sec for 50 °C and 180 sec for 60 °C, the temperature of the surrounded sand was in equilibrium (marked with dotted lines).

After a time period of 180 seconds (for 60 °C) has the surrounded sand adjusted to the increasing temperature resulting by the heated thermal conductivity sensor. The rechargeable batteries for the power supply of the sensor can be used for maximal 10 minutes. Then a recharge is necessary. Therefore two measurements with a maximum of 5 minutes during one dive can be performed.

During the second experiment the temperatures were monitored for a constant current of 2.54 A at 24 V and a constant current of 4.98 A at 48 V. The results show no measurable amperage loss. One reason is the used CrFeAl-conductor which shows a low resistor increasing with respect to the temperature. A temperature of 200 °C results a resistor R of 0.1 Ω (specification of the manufacturer). A simple calculation equation [4.10] determines a electric resistance through the used 100 m long Cu-cable of only 0.595 Ω. The low voltage loss can be accepted.

$$R = \frac{L}{\frac{1}{\rho} \cdot q} \quad [4.10]$$

whereas: $R = \text{Electric resistance } [\Omega]$
 $L = \text{Length } [m]$
 $\rho = \text{Specific resistance } [\Omega]$
 $q = \text{Cross-section } [m^2]$

$$R = \frac{100 \text{ m}}{\frac{56 \text{ m}}{\Omega \text{ mm}^2} \cdot 3 \text{ mm}^2} = 0.595 \Omega$$

The calibrations illustrate the importance of a continuously documentation of the voltage on the boat during the measurements because voltage losses evidence a necessary discharging of the battery.

4.2 Water and gas analyses

4.2.1 Chemical composition of the fluids

4.2.1.1 On-site parameters

All measured on-site parameters in 2010 which include pH value, specific electrical conductivity, redox potential, dissolved oxygen, temperature as well as the photometric determination of sulphide, nitrate and ammonium are shown in Table A 5.

The **pH values** range between 2.4 measured in “Black Point” up to 5.3 in “Bottaro North”. In general all determined pH are significantly below normal seawater pH (8.2 ± 0.1 after Millero, 2006).

The **specific electrical conductivity** shows the highest values in samples from “Hot Lake” with values around 98 mS/cm. The diving location Fumarolic field just next to the HL produce values up to 70 mS/cm. Probes collected in “Black Point” ranges between 71 and 76 mS/cm. Additionally, the diving area “La Calcara” shows increased EC value with 56 mS/cm. Gugliandolo et al. (2006) present a local specific electrical conductivity with 54 mS/cm. Samples from “Bottaro North”, “Bottaro West”, “Point 21” and “Area 26” range between 54 and 57 mS/cm indicating the high contents of seawater in the collected samples.

The determined measuring readings correspond with measurements taken in 2008 (Sieland, 2009).

The content of **dissolved oxygen** ranges between 0.39 and 7.84 mg/L whereby the lowest and highest values were determined in a single diving location, “Point 21”. Mixing of hydrothermal water with ambient seawater seems to be at this location a more important factor than at other locations.

The **redox potential** was calculated into rH value for a better comparison. The rH range was between 5.2 and 13.7 whereby the highest value was determined for “Point 21” and the lowest value for samples from “Black Point”. The second highest rH with 9.20 occurred in a probe collected in “La Calcara”. For all waters from all diving location reducing or partly

strongly reducing conditions can be stated. Normal seawater from the surface reveals a rH value of approximately 34 with a pH value of 8.2 (Merkel & Planer-Friedrich, 2002). In Figure 4-11, the results of pH and redox potentials are displayed in a E_H /pH-diagram. All samples are plotting in the vicinity to euxinic seawater. It indicates anaerobic conditions or reduced oxygen levels.

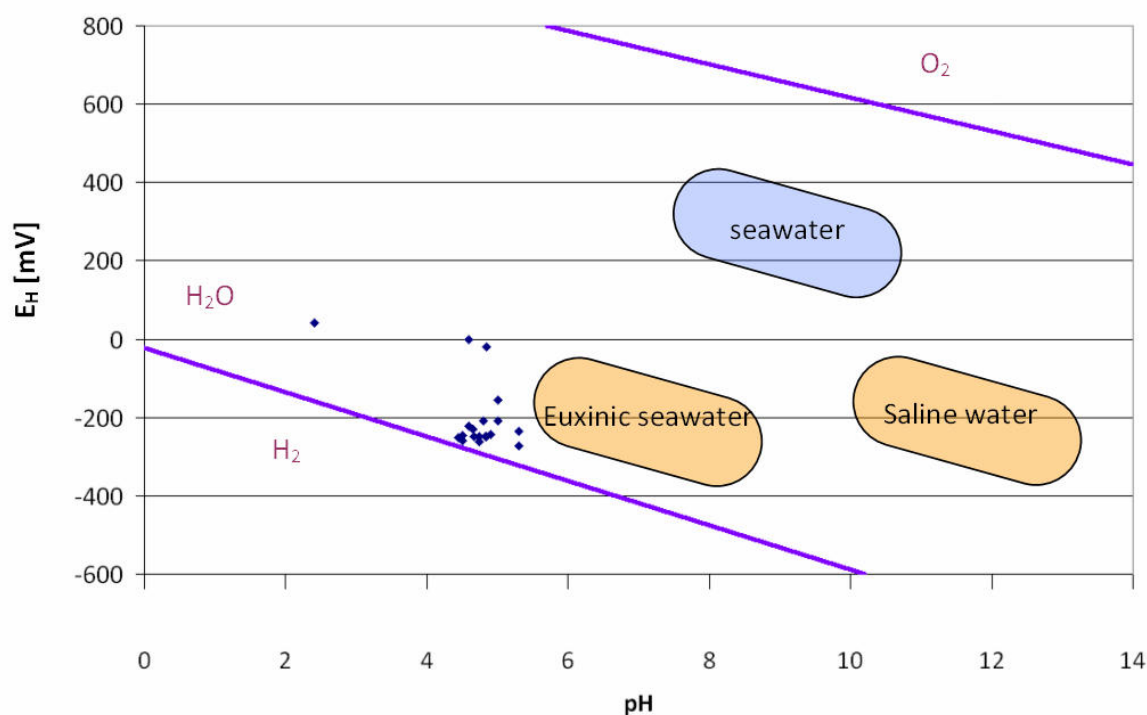


Figure 4-11: E_H /pH-diagram with upper and lower stability limits of water. Values of the samples compared to conditions of euxinic seawater, normal seawater and saline water (after Hölting & Coldeway, 2005).

Ammonium (NH_4^+), sulphide (S^{2-}) and nitrite (NO_2^-) concentrations were fitted with a calibration seawater standard solution calculating possible errors including all interference occurrences (Table A 6). Sulphide and nitrite were determined not for all water samples but at least one probe per diving location.

The concentration of sulphide ranges in a wide spread. Samples from “Point 21” display values higher than 60 mg/L but also concentrations just as low as 0.09 mg/L. High contents were as well found at “Hot Lake”, “La Calcara” and “Bottaro West”. Samples from “Black Point”, “Area 26” and “Bottaro West” and also one sample from “Hot Lake” show contents lower than 0.2 mg/L.

Nitrite was detected only in very low concentrations for all diving locations. The values range between 0.005 and 0.051 mg/L. The highest value was detected in a sample from "Hot Lake". Also "Black Point" show a slightly higher value compared to the other diving locations with 0.048 mg/L.

The contents of ammonium vary between less than 0.01 and 32.5 mg/L. The highest values were determined for "Hot Lake" and "Area 26". Probes from the "Fumarolic Field" also shows higher amounts of ammonium of about 15 mg/L compared to contents from "Bottaro West", "Bottaro North", "Black Point" or "Point 21" which range between 1 and 5 mg/L. The diving location "La Calcara" presents slightly higher contents with 11 mg/L of ammonium.

The variances in the different parameter are strongly depended on the amount of emitted hydro- and geothermal waters. An estimation of the composition of the sampled fluids is given in Section 4.2.3.1. The highest influences of other water than seawater was determined for the locations "Hot Lake", "Black Point" and "La Calcara". These results correspond with the measured On-site parameters which show for these locations the highest deviations to normal values.

4.2.1.2 Main cations and anions (IC)

In total, 24 water samples were investigated in Freiberg and 11 in Palermo in 2010. Absolute contents of each ion for all diving locations are plotted in Figure 4-12 and Figure 4-14. It has to be considered that some ion contents are multiplied with a factor to allow the illustration of all ions in one diagram. A separately exposure of each ion is arranged in Figure B 3 for anion and Figure B 4 respectively Figure B 5 for cation concentrations. For a better comparison the standard contents in seawater after Brown et al. (1995) are also displayed. These normal concentrations in ocean water are shown in Table A 1. Finally ion contents in relation to normal seawater contents after Brown et al. (1995) are illustrated in Figure 4-13 (anions) and Figure 4-15 (cations). So, the absolute enrichment or depletion in relation to oceanic water is demonstrated.

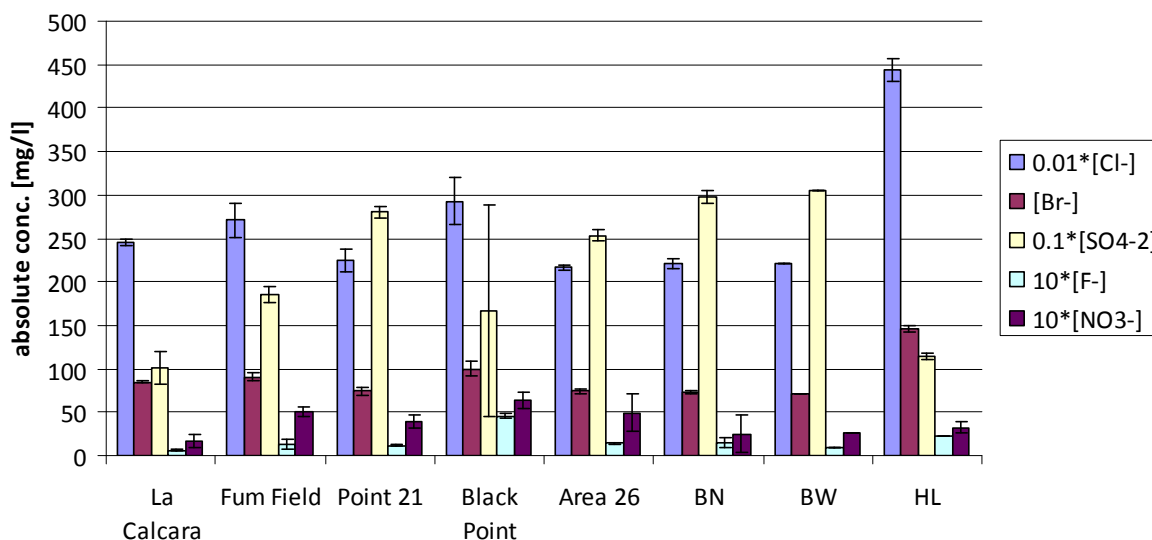


Figure 4-12: Contents of anions for each diving location from IC determinations at INGV and TUBAF including the calculated standard error.

In Figure 4-12 the contents of NO_3^- and F^- are multiplied with a factor of 10. Cl^- and SO_4^{2-} are plotted with a multiplication factor of 0.01 to fit the scale. High differences between two samples from “Black Point” results a high standard error caused by high variations within the sampling spots. Only one sample were taken at “Bottaro North”.

The comparison with normal seawater concentrations in Figure 4-13 indicates a general enrichment in chloride for all diving locations. The highest values were determined for “Hot Lake” where a total concentration about 44.4 g/L are occurring whereby the normal chloride content in seawater is around 19.5 g/L. A general fortification is also reached for bromide where the highest enrichment is also determined for “Hot Lake” with about 145 mg/L, twice as high then concentration in seawater (67 mg/L). Sulphate is slightly enriched in nearly all diving locations excepted “La Calcara” and “Hot Lake” in comparison to normal seawater (1360 mg/L). The highest concentrations are reached in “Bottaro North” with a total concentration of 2980 mg/L, an enrichment of about 1600 mg/L. Fluoride contents are also higher in most of the diving spots (exception “La Calcara” and “Bottaro West”) than in normal oceanic water. The highest concentration were found for “Black Point” with a total concentration of 6.4 mg/L, an enrichment of 3.3 mg/L compared to normal seawater concentrations. The comparison of NO_3^- contents are not shown in Figure 4-13 because of the quick reaction of NH_4^+ to nitrite and further to nitrate with the presence of oxygen.

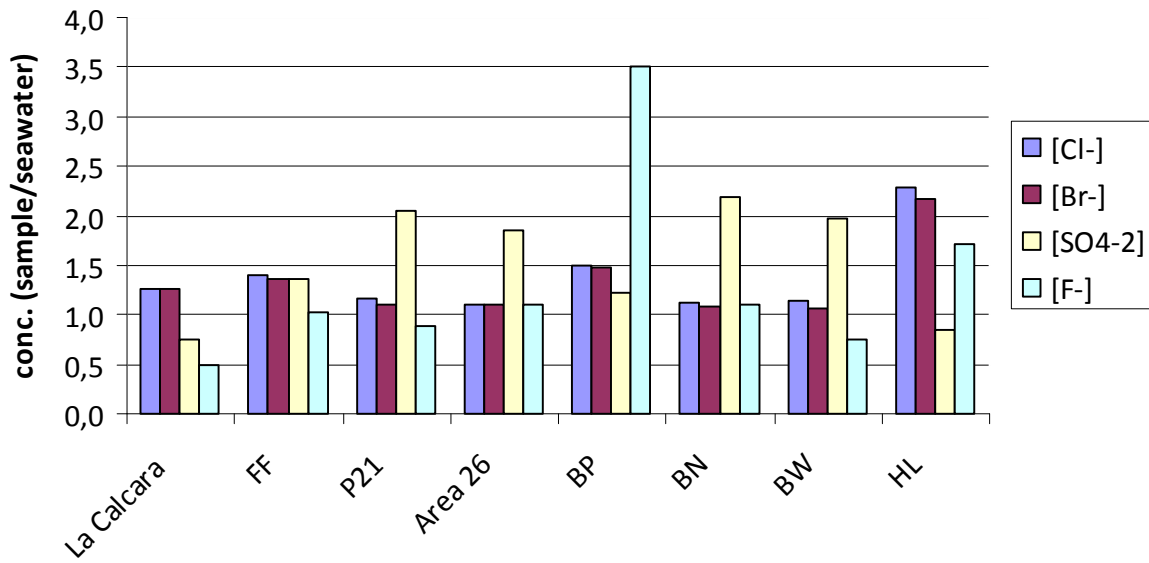


Figure 4-13: Comparison of anions in samples from different diving location with standard concentrations of seawater after Brown et al. (1995).

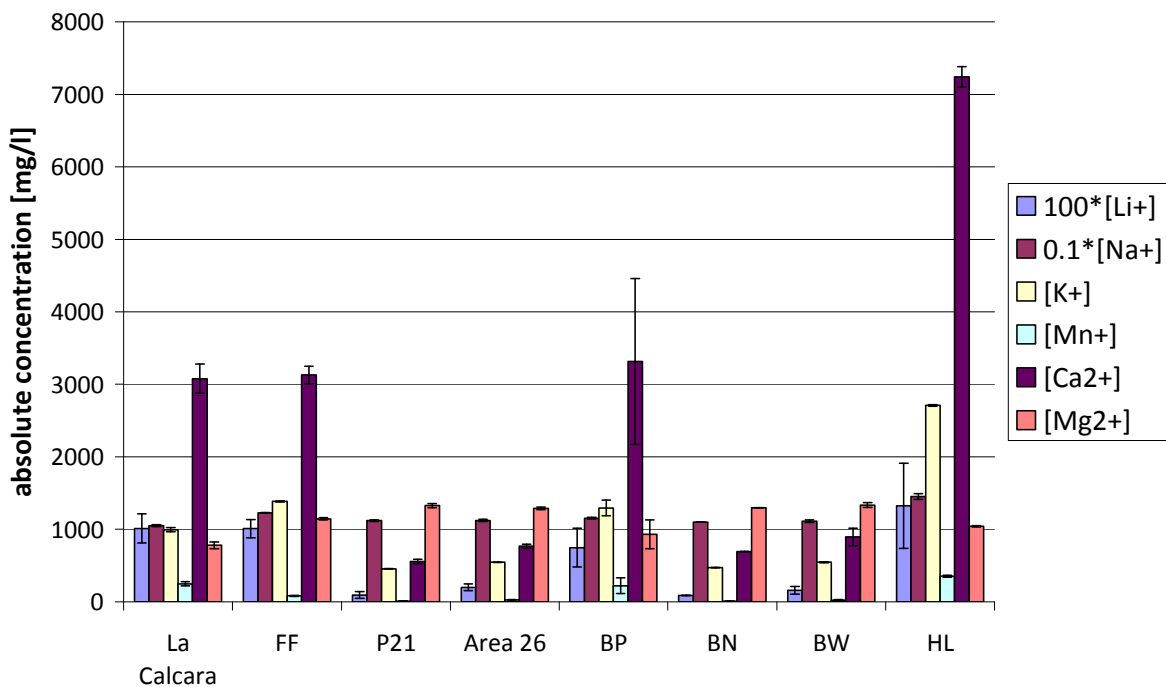


Figure 4-14: Absolute concentration of cations in water samples for each diving location. The mean values are plotted with the corresponding standard deviation.

Figure 4-14 shows the contents of lithium multiplied with a factor of 100. The high concentrations of sodium are plotted with a multiplication factor of 0.1. High calcium

concentrations were determined for different samples collected in “Black Point”. Also bigger variances occurred for manganese measured for “Hot Lake” probes. Additionally, manganese concentrations were only determined at the TUBAF laboratories.

The comparison with normal seawater concentrations in Figure 4-15 indicates a general enrichment in potassium, calcium, manganese, lithium, and sodium. In contrast magnesium occurs in lower concentrations especially in “La Calcara”, “Black Point”, “Hot Lake” and the “Fumarolic Field”. The highest anomalies compared to normal concentrations in seawater occurred in “Hot Lake” where manganese, calcium, sodium, and potassium are high enriched. High enrichments in lithium, manganese and calcium were also reached in samples from “Black Point”, “La Calcara”, and the “Fumarolic Field”.

The concentration of lithium was determined with ICP-MS which resulted a higher accuracy than IC.

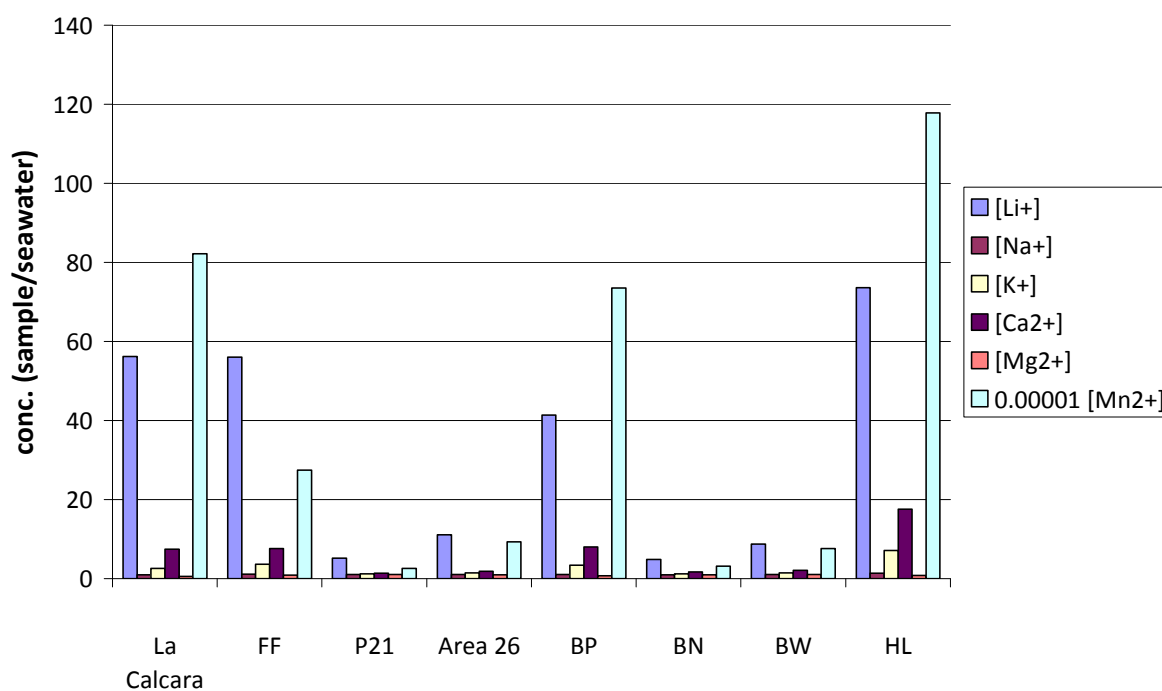


Figure 4-15: Differences of sampling points minus standard concentrations of seawater after Brown et al. (1995).

4.2.2 Chemical composition of the gas

Analyses at the INGV in Palermo

Results of the gas chromatography analyses arranged at the INGV are shown in Table 4-5 which indicate that samples were not contaminated with atmospheric air and thus used for further argon isotope analyses (Section 4.2.3.2).

Table 4-5: Results of the gas chromatography analyses at the INGV in 2010. The grey shaded field samples were used for further argon isotope analyses.

Location	He [ppm]	H ₂ [ppm]	O ₂ [%]	N ₂ [%]	CO [ppm]	CH ₄ [ppm]	CO ₂ [%]
Area26	14	-	0.028	0.36	0.8	401	95.76
BN	5	-	0.038	0.44	0.2	1	98.11
La Calcara	7	1446	7.46	23.83	1.2	4719	68.6
La Calcara	3	1152	0.0043	0.39	3.0	3747	98.93
P21	7	-	0.0097	0.26	2.5	175	95.15
BP	12	96	0.85	0.85	3.2	1645	97.08
Fum F	13	1300	2.18	4.72	3.9	12	90.56
Fum F	-	813	1.14	4.36	2.1	20	100.6
Fum F	-	823	0.0434	0.37	3.3	9	95.84

* 1 ppm = 10⁻⁴ %

Gas samples were collected as duplicates or triplicates allow double measurements and ensure uncontaminated gas samples. The three not highlighted samples, collected in “La Calcara” and “Fumarolic Field” indicate either a contamination with atmospheric air evidenced by high nitrogen and oxygen concentrations or boiling and degassing of seawater. These probes were not used for further noble gas isotope investigations.

GC results indicate an interaction between original deep gases and oceanic water, at a relative low temperature from 30 up to 100°C, at an atmospheric equilibrium (Caliro at al., 2004). They assume that the dominant gas fraction is affected by the mixing between ‘deep’ gaseous and dissolved atmospheric end-fractions which can be explained with the contents of nitrogen, oxygen and argon. Increasing argon concentrations declare an increasing influence of air saturated water (argon concentrations in gas, see Section 4.2.3.2). The comparison with gas analyses arranged before the 2002 event (Italiano & Nuccio, 1991) shows an increase in carbon dioxide which suggest a rise in the input of magmatic fluids into the hydrothermal system (Caliro at al., 2004). Caracausi et al. (2005) stated for Panarea gas samples that the composition is a mixture between deep gases which are associated with

volcanic-hydrothermal contents. Effective indicators for magma degassing are the consideration of CO₂/CH₄-ratios which is described in previous assignments from Caliro et al. (2004) and Chiodini (2009).

4.2.3 Isotopic composition of the fluids

In Table A 8 all water and gas samples are listed which were analyzed at the UFZ (total of 30 water samples, total of 53 solid samples produced out of gas and water as well as 3 biomass samples). The results from all measurements at the UFZ in April 2011 are shown in Table A 9. Additionally, 11 water samples (measured at the UFZ, as well) and 6 gas samples were analyzed at the INGV. A list from these gas samples can be found in Table A 7.

Laboratory results and interpretation of hydrogen, oxygen, carbon and sulfur isotopes analyses are presented in the following. A percentage calculation of a 3-component-mixture system and a statistical comparison of the results from both labs was done for the (D/O)-measurements.

4.2.3.1 Hydrogen and oxygen isotopic composition

The isotopic composition of water samples concerning $\delta^{18}\text{O}_{\text{VSMOW}}$ ($\delta^{18}\text{O}$) and $\delta^2\text{H}_{\text{VSMOW}}$ (δD) vary between 0.4 and 3.0 ‰ for $\delta^{18}\text{O}$ and -7.6 and 9.4 ‰ for δD regarding the UFZ measurements in 2011. The results determined at the INGV in 2010 alternate between -0.4 and 3.1 ‰ for $\delta^{18}\text{O}$ and -6 and 9 ‰ for δD . The recordings are in conformity with previous recordings taken between 2007 and 2009. All measuring values from 2007 to 2011 are plotted in (corresponding values listed in Table A 15). Water samples which were measured in both labs are plotted bold.

Possible sources of the water (deep component/magmatic water, andesitic magmatic water plus local meteoric water and Mediterranean Sea water) based on conceptual models and theories in the past are illustrated in Figure 4-17. It also contains reference lines (World Meteoric Water Line (WMWL), Mediterranean Meteoric Water Line (MMWL) and Local

Meteoric Water Line (LMWL)). The isotopic ranges and equations of the regression lines and potential water sources are shown in Table 4-6. All theoretical sources of water are based on measurements of fumaroles from Vulcano Island. It should be mentioned that Vulcano belongs to the TL fault system (Section 2.1) whereby isotopic variations to the NE-SW fault system of Panarea could be possible.

Table 4-6: Used reference lines and potential water sources which are shown in Figure 4-16.

Meteoric Water Lines (MWL)	Mediterranean Meteoric Water Line (MMWL) (Gat and Carmi, 1970)	$\delta D = 8 \cdot \delta^{18}O + 22$
	World Meteoric Water Line (WMWL) (Craig, 1961)	$\delta D = 8 \cdot \delta^{18}O + 10$
	Local Meteoric Water Line (LMWL) (for south Italy after IAEA, 2011)	$\delta D = 6.9548 \cdot \delta^{18}O + 4.5796$
Potential water sources	Deep component (Capasso et al., 1997)	$\delta^{18}O_{VSMOW} [‰] = 6 \text{ to } 8$ $\delta D_{VSMOW} [‰] = 10 \text{ to } 15$
	Magmatic water (Bolognesi & D'Amore, 1993)	$\delta^{18}O_{VSMOW} [‰] = 7 \text{ to } 8$ $\delta D_{VSMOW} [‰] = -5 \text{ to } 15$
	“Andesitic” magmatic water (Giggenbach (1992) and Chiodini et al. (1995))	$\delta^{18}O_{VSMOW} [‰] = 3 \text{ to } 6.5$ $\delta D_{VSMOW} [‰] = -10 \text{ to } -20$
	Mediterranean Sea water (Grassa et al., 2006)	$\delta^{18}O_{VSMOW} [‰] = 1$ $\delta D_{VSMOW} [‰] = 10$
	Local meteoric water (Liotta et al., 2008)	$\delta^{18}O_{VSMOW} [‰] = 4.7$ $\delta D_{VSMOW} [‰] = 25$

The existing theories of the origin of the upwelling fluids which are shown in Table 4-6 are explained briefly in the following. Bolognesi & D'Amore (1993) proposed that the hydrothermal system is fed by magmatic waters which are mixed with meteoric water or a geothermal component. Another theory from Grassa et al. (2006) suggests a mixing between meteoric water and different groundwaters including heavy-isotope rich seawater. In the thesis from Hanetzog (2011) (D/O)-signatures of water are recorded which were sampled in wells on Lipari showing a $\delta^{18}O_{VSMOW}$ value of -6.62 ‰ and δD_{VSMOW} of -40 ‰. Another water source could be a brine of marine origin with meteoric water (Capasso et al., 1992). Capasso et al. (1997) supposed a deep component which is possibly mixed with meteoric waters or

meteoric waters. Combinations of $\delta^{18}\text{O}$ -shifted seawaters respectively hydrothermal components as well as magmatic components which are based on andesitic magmatic waters (Giggenbach, 1992) are suspected by Chiodini et al. (1995 and 2006). (D/O)-measurements taken between 2007 and 2011 (Figure 4-16), range in a wide spread. The best approximation to a MWL is observable for the Local Meteoric Water Line (LMWL) as well as the World Meteoric Water Line (WMWL). Most of the (D/O)-values range between these lines which can be reasoned by equilibrium processes between thermal water and rocks (Capasso et al. (1997), Grassa et al. (2006), Chiodini et al. (2000)). Many measuring points plot close to the isotopic signature of Mediterranean Sea water with a light shifting to heavier $\delta^{18}\text{O}_{\text{VSMOW}}$ signatures (for example "Bottaro West", "Area 26", "Point 21"). These samples contain probably just less amounts of geothermal, magmatic respectively andesitic water. Samples from "Black Point" as well as "Bottaro Nord" show a wide variance. The location "La Calcara" shows isotopic heavier water related to the $\delta^{18}\text{O}$ values. It can be assumed that the part of magmatic water respectively deep component is higher compared to other collected samples. The isotopic signature of the diving spots "Hot Lake" respectively "Fumarolic Field" as well as some measurements from "Black Point" show depleted δD -values compared to the isotopic signature of Mediterranean Sea water. The approach to isotopic signatures of magmatic water respectively deep component and andesitic magmatic waters are greater for the locations "Hot Lake", "La Calcara" as well as "Black Point".

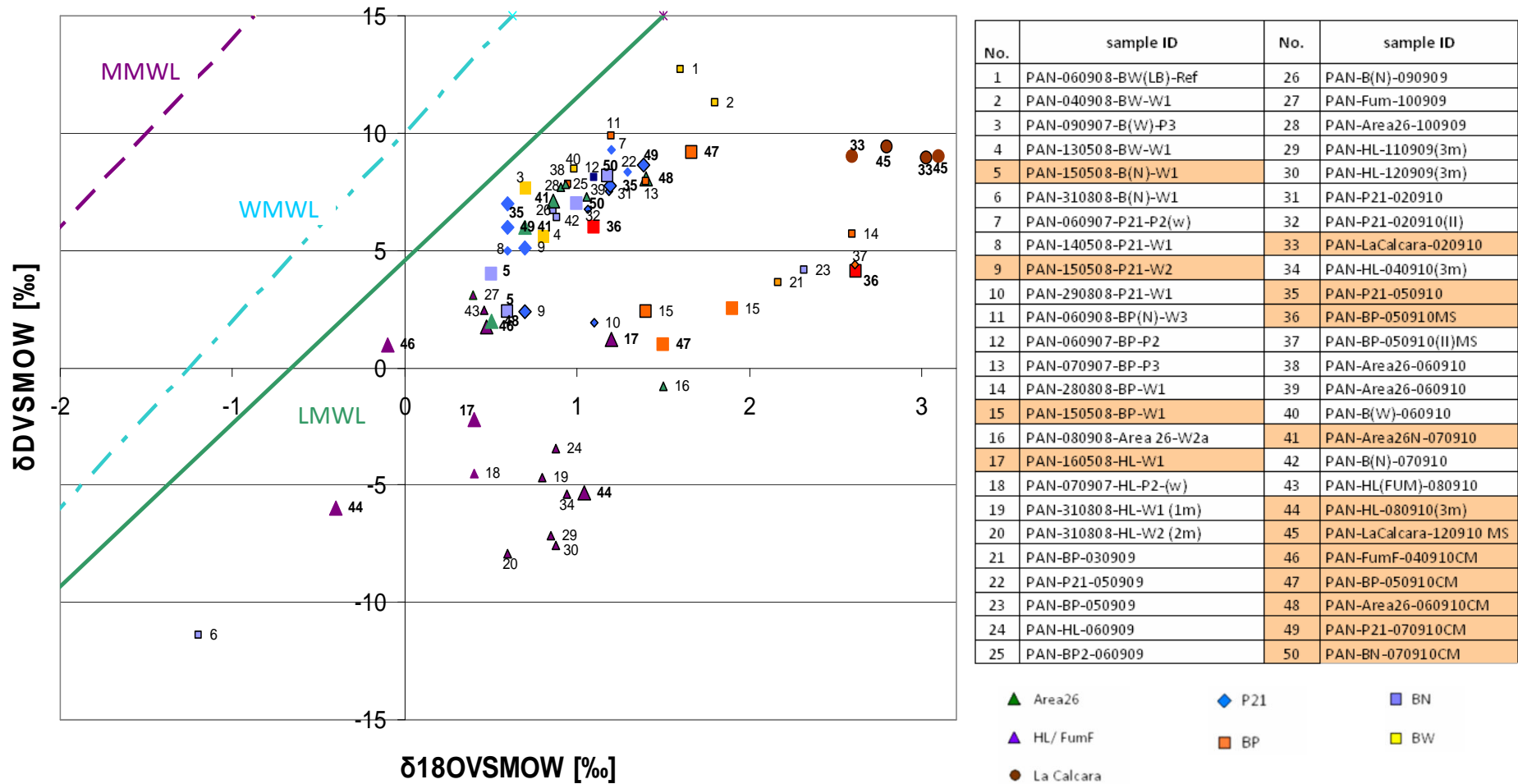


Figure 4-16: Detailed visualization of the $\delta\text{D}/\delta^{18}\text{O}$ composition in sampled water from 2007, 2008 and 2010 which were analyzed at the UFZ and INGV. It illustrates the isotopic signature for each diving location as well as a comparison of 15 measurements between the labs (bigger plotted measuring values, highlighted in the legend). All UFZ measurement points are marked with a black border whereby the INGV reading points are not bordered.

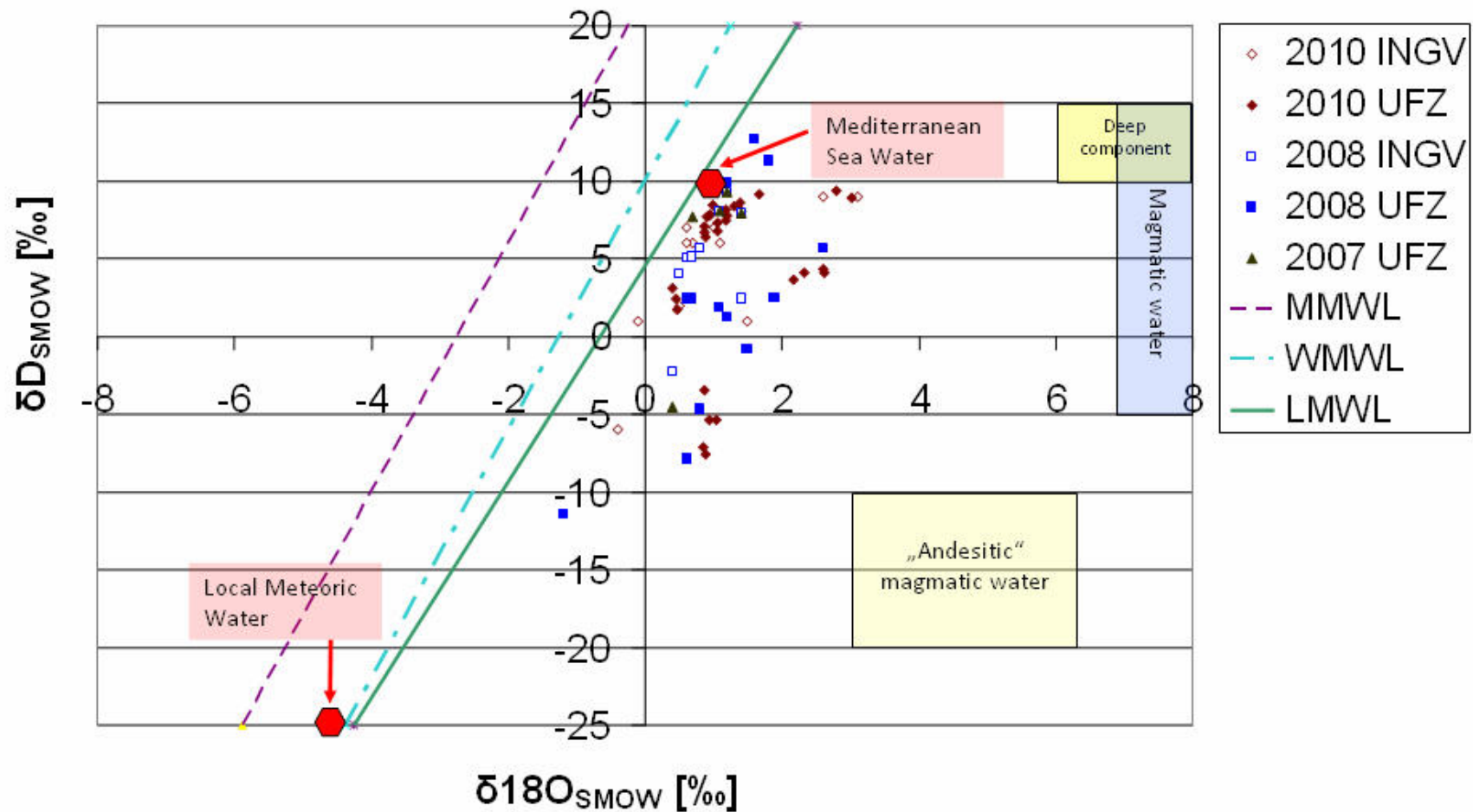


Figure 4-17: Isotopic composition $\delta D/\delta^{18}O$ of sampled water in 2007, 2008 and 2010 which were analyzed in two laboratories (UFZ and INGV). Additionally, several interpretations of possible water sources based on measurements of fumarolic streams from Vulcano Island (Deep component after Capasso et al. (1997), Magmatic and geothermal component after Bolognesi & D'Amore (1993), "Andesitic" magmatic water after Giggenbach (1992) & Chiodini et al. (1995)) as well as the local meteoric water (precipitation from western Sicily after Liotta et al., 2008) and the shifted value for Mediterranean Sea water after Grassa et al. (2006).

➤ 3-components-mixing-system

A 3-components-mixing-system compose of “Local Meteoric water”, “Mediterranean Sea water” and “Magmatic water” is supposed in the following. Voting for these possible sources is based on scientific findings in the past. Figure 4-18 shows that mostly all points can be described with these three water sources. The corresponding coordinates of the reference liquids are based on literature values (Table 4-6). In further interpretations, it has to be recognized that (D/O)-data for Meteoric water and Local meteoric water possess a range of values (ellipsoids shown in Figure 4-18).

- Local meteoric water:* $\delta^{18}\text{O}_{\text{VSMOW}}$ of 4.7 ‰ and $\delta\text{D}_{\text{VSMOW}}$ of 25 ‰
- Mediterranean Sea water:* $\delta^{18}\text{O}_{\text{VSMOW}}$ of 1 ‰ and $\delta\text{D}_{\text{VSMOW}}$ of 10 ‰
- Magmatic water:* $\delta^{18}\text{O}_{\text{VSMOW}}$ of 7.5 ‰ and $\delta\text{D}_{\text{VSMOW}}$ of 5 ‰

For “Magmatic water” a mean value is defined. The subsequently calculations give the percentage proportion from the 3 components for each water sample. The achievements are shown in ternary plots (Figure 4-19). The calculated results of the percentage proportions are shown in Table A 16 (for UFZ data) and Table A 17 (for INGV data).

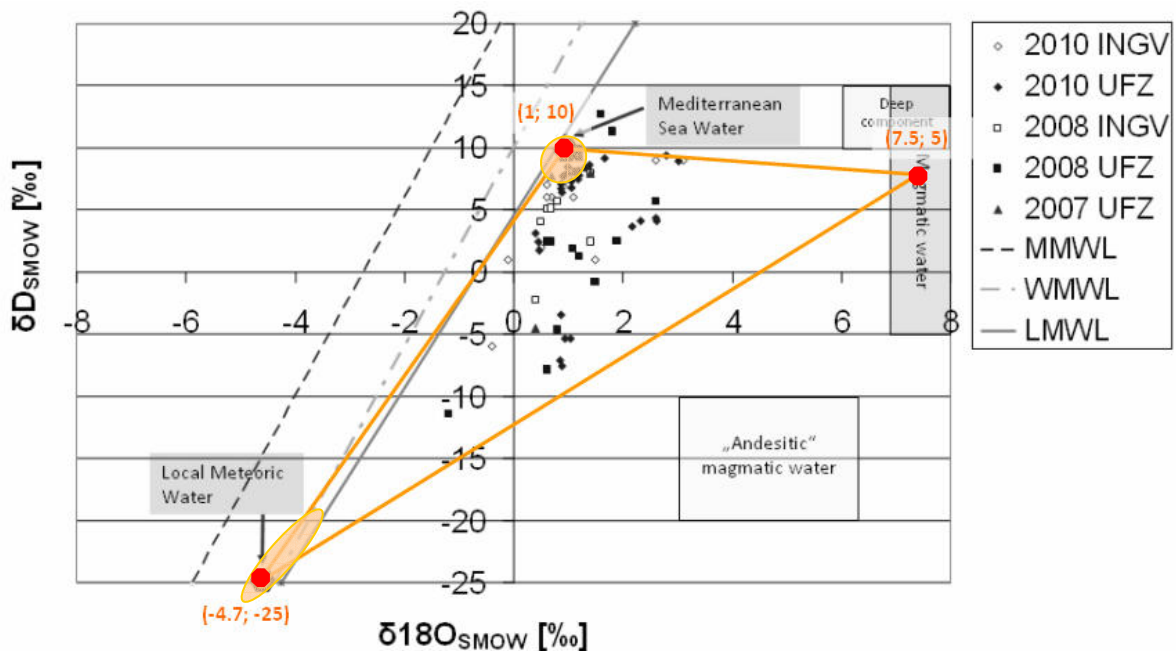


Figure 4-18: Accepted sections to calculate a 3-component-mixture. 6 measuring points are located outside of the triangle and can not be used for the evaluation (probes from “La Calcara” and “Bottaro West”). All the other points can be described by percentual proportions of each water source.

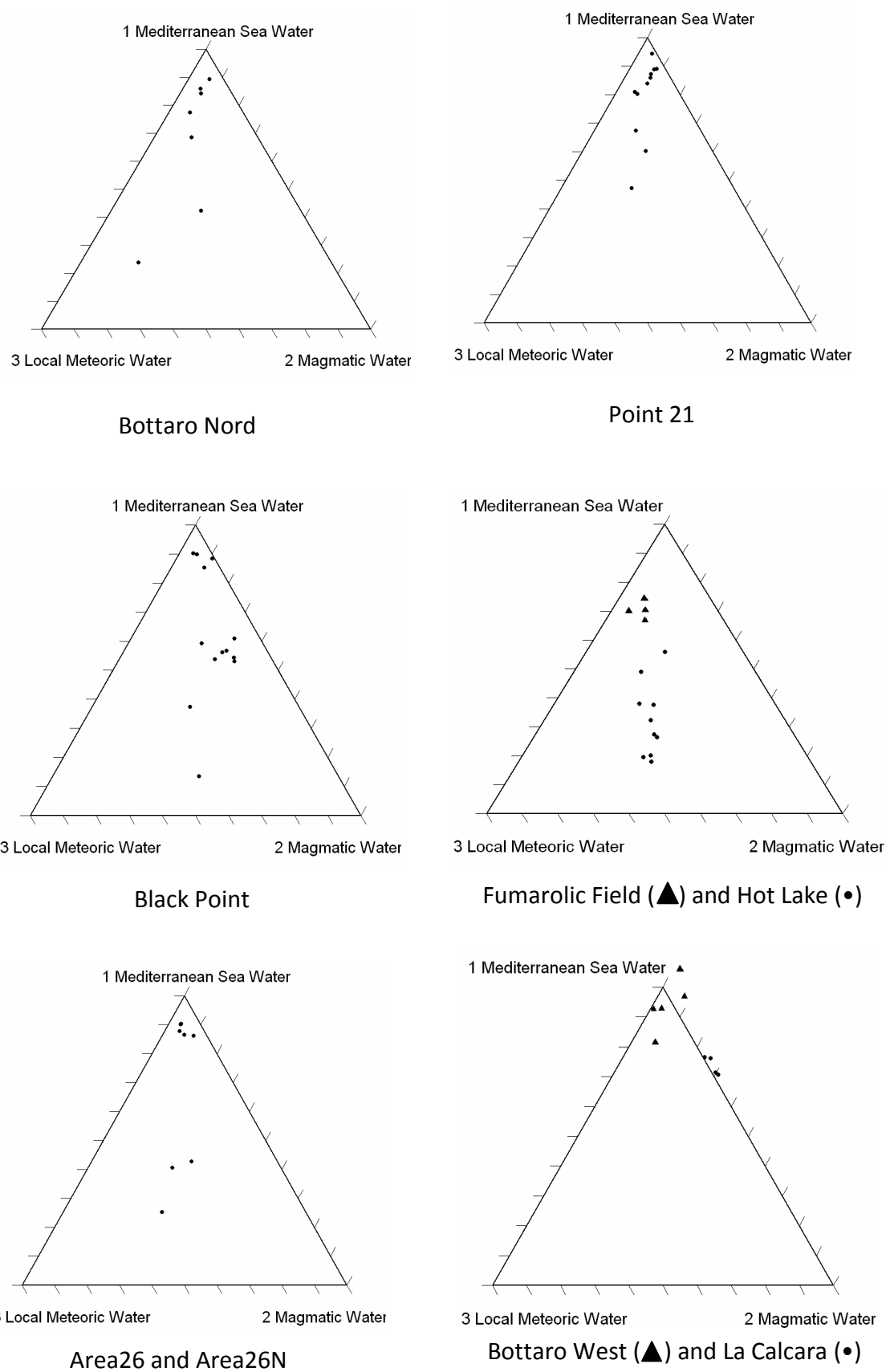


Figure 4-19: Ternary triangular-plot displayed for all diving locations. Water from “La Calcara” and “Bottaro West” plot outside the triangle.

Ternary plots for certain sampling sites are shown in Figure 4-19. Water samples from the locations “Bottaro Nord” and “Bottaro West” display a dominant content of Mediterranean Sea water of around 80 to 95 %. The other two components (Magmatic and Local Meteoric water) play a minor role. Two probes from “Bottaro West” plot outside the triangle. Samples from “Point 21” and “Area 26” also mostly consist of Mediterranean Sea water. But some samples show a water content of Local Meteoric and Magmatic water of about 20 %. The sampling location “Black Point” reveals two different water mixtures. One is dominated by Mediterranean Sea water with approximately 90 %. The other type consists of 50 to 60 % of Mediterranean Sea water, 35 % Magmatic water and 10 to 20 % of Local Meteoric water. In this diving location a source of external water might exist (recharged by a magmatic or meteoric water source). Other probes just represent the isotopic signature of Mediterranean Sea water.

The water mixture found in “Hot Lake” and “Fumarolic Field” indicate different sources, as well. Water samples from the “Fumarolic Field” consist to 70 % of meteoric water; “Hot Lake” is composed to 40 % of Meteoric water, approximately 35 % of magmatic water and just 25 % of Mediterranean Sea water. High water up welling rates can be assumed at “Hot Lake”. “Fumarolic Field” samples just a few 10 meters away does not show these intense external water emissions.

Two water samples from “La Calcara” have a magmatic water content of 25 to 30 %. The data points are lying outside the ternary plot, but this likely due to analytical uncertainties.

Table 4-7 shows 15 water samples (4 water samples from 2008 and 11 water samples from 2011) which were analyzed in both laboratories. The measurement differences between oxygen and hydrogen isotopes are plotted in Figure 4-20. Following conclusions are based on the parallel measurements shown in the table below.

With a few exceptions the isotopic signature of $\delta^{18}\text{O}_{\text{VSMOW}}$ between the UFZ and the INGV laboratory show no high discrepancies. $\delta^{18}\text{O}_{\text{VSMOW}}$ measurements done at the UFZ range between 0.5 and 3.0 ‰ whereas recordings determined at the INGV range between -0.4 and 3.1 ‰. The maxima discrepancy is determined with 1.5 ‰ (sample: BP-050910MS).

Isotopic signatures of $\delta\text{D}_{\text{VSMOW}}$ vary between -5.3 and 9.4 ‰ for UFZ data and -6 and 9 for INGV recordings. The highest deviation was 8.2 ‰ for a sample from “Black Point” (BP-050910CM).

Table 4-7: Selected results of the isotopic composition D/O in water which were determined at the INGV and UFZ (samples from 2008 and 2010).

Location-ID	INGV		UFZ		Δ (UFZ-INGV)	
	$\delta^{18}\text{O}_{\text{VSMOW}}$ [‰]	$\delta\text{D}_{\text{VSMOW}}$ [‰]	$\delta^{18}\text{O}_{\text{VSMOW}}$ [‰]	$\delta\text{D}_{\text{VSMOW}}$ [‰]	$\Delta \delta^{18}\text{O}_{\text{VSMOW}}$ (UFZ-INGV) [‰]	$\Delta \delta\text{D}_{\text{VSMOW}}$ (UFZ-INGV) [‰]
PAN-150508-B(N)-W1	0.5	4	0.6	2.4	0.1	-1.6
PAN-150508-P21-W2	0.7	5.1	0.7	2.4	0.0	-2.7
PAN-150508-BP-W1	1.4	2.4	1.9	2.5	0.5	0.1
PAN-160508-HL-W1	0.4	-2.2	1.2	1.2	0.8	3.4
PAN-LaCalcara-020910	2.6	9	3.0	8.9	0.4	-0.1
PAN-P21-050910	0.6	7	1.2	7.8	0.6	0.8
PAN-BP-050910MS	1.1	6	2.6	4.1	1.5	-1.9
PAN-Area26N-070910	0.7	6	0.9	7.1	0.2	1.1
PAN-HL-080910(3m)	-0.4	-6	1.0	-5.3	1.4	0.7
PAN-LaCalcara-120910 MS	3.1	9	2.8	9.4	-0.3	0.4
PAN-FumF-040910CM	-0.1	1	0.5	1.8	0.6	0.8
PAN-BP-050910CM	1.5	1	1.7	9.2	0.2	8.2
PAN-Area26-060910CM	0.5	2	1.4	8.0	0.9	6.0
PAN-P21-070910CM	0.6	6	1.4	8.6	0.8	2.6
PAN-BN-070910CM	1	7	1.2	8.2	0.2	1.2

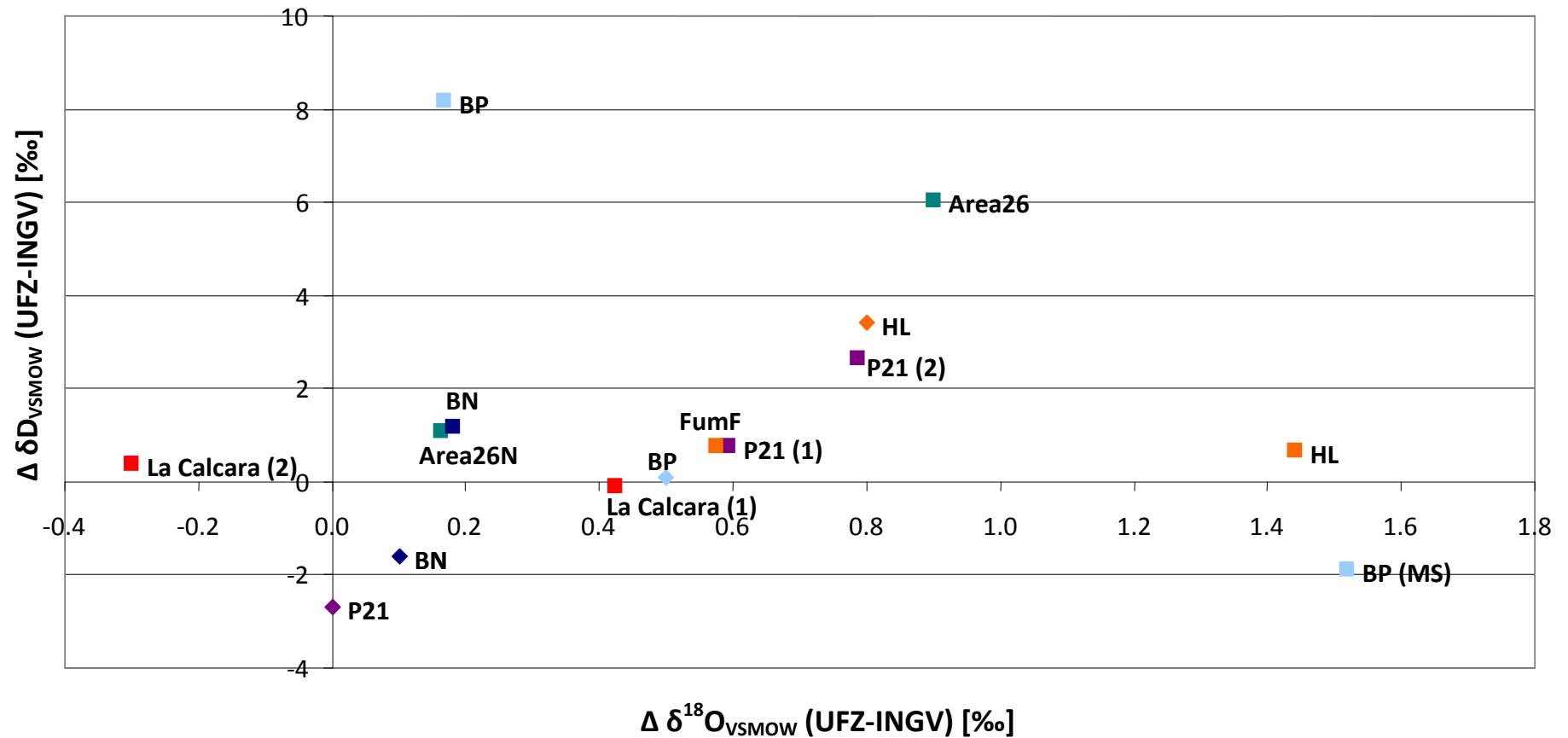


Figure 4-20: Comparison of (D/O) - measurements arranged at the INGV and UFZ by visualisation of measuring differences (Table 4-7). Diamond-shaped rhombic points are measurements arranged in 2008. The rectangular points are measurements derived from examinations in 2010/2011. The maximum shifts of $\Delta \delta\text{D}_{\text{VSMOW}}(\text{UFZ-INGV})$ and $\Delta \delta^{18}\text{O}_{\text{VSMOW}}(\text{UFZ-INGV})$ are 8.2 ‰ and (comparatively low) 1.5 ‰, respectively.

The laboratory comparison illustrated in Figure 4-20 show that $\delta^{18}\text{O}_{\text{VSMOW}}$ determined at the UFZ are in general higher than the same probes analyzed at the INGV. The average discrepancy is 0.5 ‰. The deviation for $\Delta\delta\text{D}_{\text{VSMOW}}$ is higher (average 1.3 ‰). UFZ recording illustrate a higher δD compared to measurements performed at the INGV.

Results of a Single ANalysis of VAriance (ANOVA) are presented in the following. This statistical method tests if the variations of the mean values are randomized or methodically. The total variance of the measurement values s_{corr}^2 is composed of the statistical spread within laboratories (s_{R}^2) as well as between the laboratories (s_{Lab}^2) shown in equation [4.11].

$$s_{\text{corr}}^2 = s_{\text{Lab}}^2 + s_{\text{R}}^2 \quad [4.11]$$

Thereby the different variances are calculated with the following equations [4.12] to [4.15].

$$s_{\text{corr}}^2 = \sum_{j=1}^{n_j} \sum_{i=1}^q (x_{ij} - \bar{x}_{\text{total}})^2 \quad [4.12]$$

$$\bar{x}_{\text{total}} = \frac{1}{n} \sum_{j=1}^q \sum_{i=1}^{n_j} x_{ij} \quad [4.13]$$

$$s_{\text{Lab}}^2 = \sum_{i=1}^q \sum_{j=1}^{n_j} (x_{ij} - \bar{x}_j)^2 \quad [4.14]$$

$$s_{\text{R}}^2 = \sum_{j=1}^q n_j (\bar{x}_j - \bar{x}_{\text{gesamt}})^2 \quad [4.15]$$

whereas: q = Amount of laboratories, here: 2
 n_j = Amount of parallel determination per laboratory j
 x_{ij} = Measurement value of the repeated recording i in laboratory j
 \bar{x}_j = mean value of the serial from laboratory j
 n = number of total measurements

Acceptation of the null hypothesis is based on the F-test which is expressed in equation [4.16].

$$F = \frac{\frac{s_{\text{Lab}}^2}{(q-1)}}{\frac{s_{\text{R}}^2}{(n-q)}} \quad [4.16]$$

The F-value can be compared with the F_{crit} -value which is written in the Fisher table respectively F-distribution. These value depends on α which is set to of 0.05. If the value F is higher than F_{crit} then the F-Test is significant which means the measurements differences are not randomized but systematically.

These method was used for the comparison of the (D/O)-values measured at the UFZ and INGV (Table 4-7). Table A 10 and Table A 12 present the $\delta^{18}\text{O}$ and δD values with the corresponding mean values and variances. The results at the INGV represent an average from 3 single determinations. Unfortunately the discrete recorded values are not available whereby the variances are set zero. Table A 11 and Table A 13 illustrate the sources of variation, the degree of freedom, the single variances s_{Lab}^2 and s_R^2 as well as the resulting F-values and corresponding F_{crit} -values. A conclusion about the significance by compare the F and F_{crit} - values was also performed.

The single factor analysis illustrates that half of the measuring values vary within a statistical spread. Other values show a significant difference to each other which indicate a discrepancy that is not randomized.

Duplicate measurements of samples from “La Calcara”, “Fumarolic Field”, and “Area26N” show for both tests ($\delta^{18}\text{O}$, $\delta^2\text{H}$) a F-value which is lower than the F_{crit} value. Occurring measuring differences between the labs are within the limit of variation. Probes from “Black Point”, “Point 21” and “Area 26” illustrate a variation of the measuring values which are not randomized (F-values higher than corresponding F_{crit} -values). These data are significantly different to each other.

The differences in the results can be explained with the different methods used (Section 3.5). In the laboratories at the UFZ samples were distilled before the isotopic analysis. Containing saline components were separated from the sample within a temperature up to 600 °C. The measuring principle for $\delta^2\text{H}$ which is used at the INGV is based on pyrolysis. A separation of ions occurs before the actual thermochemical decomposition but during a much lower temperature of approximately 60 °C. This significant lower temperature separates probably less ions whereby more dissolved ingredients can influence the measurement. Thus crystal waters may influence the isotopic measurements significantly. But this is an assumption and needs further investigation.

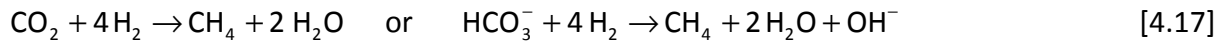
Another explanation can be the different time span between the analyses. The water samples were analysed at the INGV just 2 weeks after collection. The measurement of the water samples at the UFZ took place 6 months after the collection. The samples were not stored continuously in the fridge.

4.2.3.2 Carbon isotopic composition

The $\delta^{13}\text{C}_{\text{DIC}}$ values of 30 water samples taken in 2009 and 2010 and measured at the UFZ in 2011 range between -12.1 and 22.5 ‰ (PDB). All measurements are reported in Table A 14. It also contains measurements performed in 2008 at the UFZ and INGV. In Figure 4-21 mean values $\delta^{13}\text{C}_{\text{DIC}}$ are presented from all diving locations based on almost all previous made determinations including 2008. The standard deviation varies between a maximum value of 10.4 ‰ for “Area 26” and 2.9 ‰ for location “La Calcara”. Only 4 measurements were performed at the INGV in 2008. One value (*PAN-BP-150508*) deviates extremely from measurements performed at the UFZ with -17.65 ‰ (PDB). Reasons for this are probably not appropriate storage and high temperatures during the transport, mentioned by Sieland (2009). The other 3 readings conform to UFZ measurements performed in 2011 and incorporate in the calculations which resulting the diagram in Figure 4-21.

Figure 4-21 shows isotopic compositions from different carbon sources in the environment: volcanic gases (approximately -5 to -8 ‰ (PDB)) and Mediterranean volcanic gases (approximately -3 to 0 ‰ (PDB)).

A reason that may cause an increase of $\delta^{13}\text{C}$ in the residual fraction and might explain the positive trend of our measured carbon isotopic compositions is methanogenesis, a microbial process leading to the formation of methane. This process results in an enrichment of heavy isotopes in the residual methane fraction because microorganisms prefer the lighter ^{12}C isotopes caused by lower energy “costs” associated with breaking the molecular bonds (kinetic fractionation) (Clark & Fritz, 1997). Methanogenesis is a form of anaerobic respiration which can occur in two different pathways, utilising either carbon dioxide or acetic acid as electron acceptors. The first way is important for saline and marine systems where methane is mostly created by CO_2 reduction (Whiticar, 1999) resulting by sulphate-reducing bacteria. The corresponding equation [4.17] is following below.



The microbial decomposition as a kinetic fractionation effect can be characterized with the Rayleigh distillation equation. Further information can be found in Rayleigh (1896) and Hoefs (1997). The corresponding equation [4.18] is shown in the following after Hoefs (1997).

$$\left(\frac{R_t}{R_0} \right) = \left(\frac{c_t}{c_0} \right)^{\frac{1}{\alpha-1}} \quad [4.18]$$

whereas: R_t = Ratio of the isotope (here: $^{12}\text{C}/^{13}\text{C}$) in the reactant
 R_0 = Initial ratio ($^{12}\text{C}/^{13}\text{C}$)
 c_t = Concentration of the more abundant isotope (^{12}C)
 c_0 = Initial concentration (^{12}C)
 α = Isotope fractionation factor

Microbial CO_2 reduction resulting an decreasing in c_t respectively R_t in the residual fraction whereby the $\delta^{13}\text{C}$ values are increasing (Section 1.2.2, equation [1.2]). Possibly occurring Rayleigh enrichment during CO_2 reduction is indicated in Figure 4-21.

But, the contents of methane in emitted gases range between just a few ppm in “Bottaro North” up to more than 3700 ppm (equal to 0.37 %) for “La Calcara” (Table 4-5, Section 4.2.2). These small amounts of exhausting methane, however, make the assumption of an existing methanogenesis questionable. Measured temperatures (Chapter 4.1) with maxima values in “La Calcara” of about 135 °C (depth of 370 mm) present a hostile environment for bacteria. The process of bacterial methanogenesis is not possible in regions with temperature over approximately 85 °C (*Thermus thermophilus* HB27, Kosuge et al., 2000). Thus another source might exist to cause an increasing in heavier carbon isotopic compositions of around 20 ‰ (PDB).

During the Miocene, the region of the Mediterranean Sea was enhanced by the so called Messinian salinity crisis (MSC) (Hsü et al., 1973). This evaporitic event was caused by the isolation of the Mediterranean Sea from the Atlantic Ocean. Large amounts of Messinian evaporites were matured in a series of sub-basins confined by local barriers, within an expanded pre-Messinian basin (Cavazza and Wezel, 2003). During this time it can be assumed that methanogenesis processes could occur. Generated methane could fumigate whereby heavier carbon isotopes could be enriched in the basement residual fraction (e.g. Carbonates). But this is only speculation and needs verification. The isotopic variances of

MSC evaporates range in a wide spread. D'Alessandro et al. (2007) declared $\delta^{13}\text{C}$ value in travertine deposits of the SW flank of Mt. Etna between 1 and 5 ‰ (PDB) whereby McKenzie and Ricchiuto (1978) assume a carbon isotopic signature in the Ionian Basin of 1.8 up to 13.8 ‰ (PDB). This prior methanogenesis might be the reason in the detection of high $\delta^{13}\text{C}$ values but the low concentrations in methane. But $\delta^{13}\text{C}$ signatures of more than 20 ‰ (PDB) could not be found in the literature.

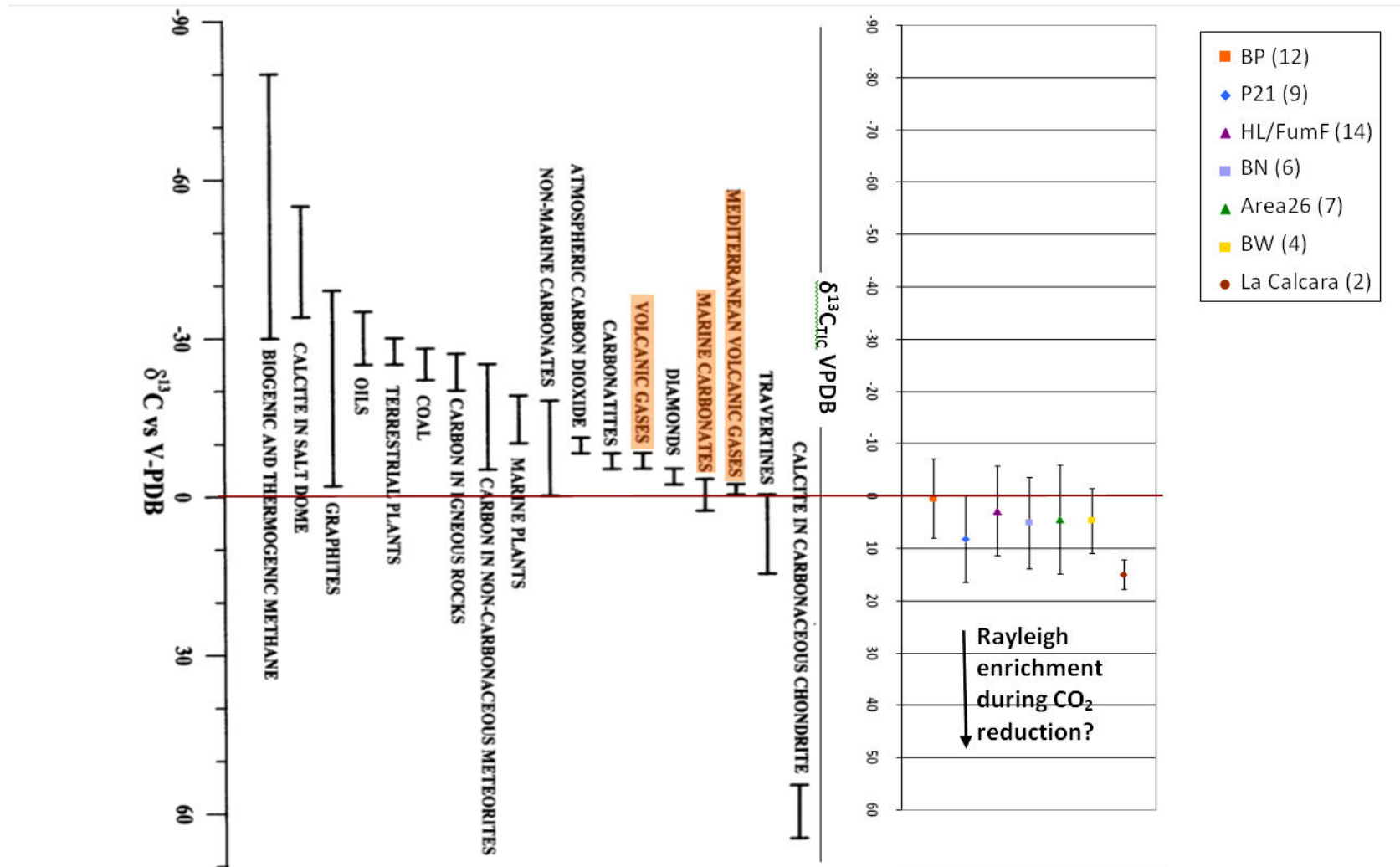


Figure 4-21: Water samples from 2008, 2009 and 2010 analyzed for $\delta^{13}C_{DIC}$ at the INGV and the UFZ. Mean values and standard deviation for each diving location is illustrated separately. The quantity of measurements is given in brackets in the legend. All Panarea samples and the corresponding values are saved in Table A 14. Reference isotopic compositions are plotted on the left side. Data are from Fornaseri (1984), Faure (1986), Hoefs (1987) Favara et al. (1999), Inguaggiato et al. (2000) and Favara & Inguaggiato (2000).

4.2.4 Isotopic composition of the gas

4.2.4.1 Carbon isotopic composition

6 gas samples were investigated for $\delta^{13}\text{C}_{\text{CO}_2}$ could be arranged at the INGV in 2010 whereat 3 of them additionally, could be measured for $\delta^{13}\text{C}_{\text{CH}_4}$ composition. The other gas samples showed too low methane concentrations (less than 440 ppm, Table 4-5 in Section 4.2.2) which is under the sensitivity of the instrument. The results are shown in Table 4-8. $\delta^{13}\text{C}_{\text{CH}_4}$ contents show a minima of -25.6 ‰ and a maxima value of -16.8 ‰ (VPDB). The carbon isotopes in CO_2 range between -3 and 1.9 ‰ (VPDB). Additionally, $\delta^{13}\text{C}_{\text{DIC}}$ contents from gas were measured in 2007 and 2011 at the UFZ (from precipitates). Results are also tabulated in Table 4-8. The carbon isotopes in DIC varied between -6.0 and -2.2 ‰ versus VPDB. Measured $\delta^{13}\text{C}$ in methane were also determined in 2006 at the UFZ for 4 fumaroles in “Point 21” (Table 4-8). The values range between 10.5 and 18.1 ‰ (VPDB). Results are totally different to the recordings in 2010.

Table 4-8: Results of the analyzed gas samples for stable isotopes ($\delta^{13}\text{C}_{\text{CH}_4}$, $\delta^{13}\text{C}_{\text{CO}_2}$, $\delta^{13}\text{C}_{\text{DIC}}$) at the INGV and UFZ in 2010 and 2011.

Location	INGV		UFZ	
	$\delta^{13}\text{C}_{\text{CH}_4}$ [‰] VPDB	$\delta^{13}\text{C}_{\text{CO}_2}$ [‰] VPDB	$\delta^{13}\text{C}_{\text{CH}_4}$ [‰] VPDB	$\delta^{13}\text{C}_{\text{DIC}}$ [‰] VPDB
Area26-060910 (CM)	-16.8	-3		
BP-050910 (CM)	-25.6	-1.8		
La Calcara-020910 (CM)	-17.4	1.9		
P21-070910 (CM)		-2.6		
HL (Fum F)-040910 (CM)		0.4		
BN-070910 (CM)		-2.5		
P21-030909				-3.3
P21-050909				-2.5
BP-060909				-5.8
BN-090909				-2.2
HL (FumF)-100909				-3.3
Area26-120909				-4.2
BW_310807				-3.8
BN_040907				-4.2
BP_060907				-6.0
P21_Claudia_090906			10.50	
P21_Patricia_090906			15.20	
P21_Melanie_100906			18.10	
P21_Wanda_100906			18.10	

Mook (2000) reports $\delta^{13}\text{C}_{\text{CO}_2}$ for ground water between -25 to 14 ‰ (PDB) and a range of -20 to 13 ‰ (PDB) for fresh water carbonates. Carbon isotope signatures in CO_2 gas ranging between -1.06 and -3.2 ‰ (PDB) indicate decarbonisation processes of marine carbonates (Italiano and Nuccio, 1991). Another possible source is described by Capasso et al. (1997). They assess the input of magmatic gases which causing a $\delta^{13}\text{C}_{\text{CO}_2}$ signature between -5 and -8 ‰ (PDB). The measured $\delta^{13}\text{C}_{\text{CO}_2}$ indicate slightly heavier values.

In general the $\delta^{13}\text{C}_{\text{CH}_4}$ signatures can be originated from three different sources: biogenic, geothermal or methane from the mantle. Previous research in isotopic compositions of carbon and methane is rare. Depending on the chemical properties it can be declared that carbon is more reactive compared to methane. So it can be assumed that the isotopic composition of carbon is relative independent in temperature whereby the carbon isotopic signature in methane depends on temperature variations.

The isotopic composition from biogenic sources lies between -110 to 50 ‰ (PDB) after Whiticar (1999). Barker & Fritz (1981) and Grossmann et al. (2002) specified the $\delta^{13}\text{C}_{\text{CH}_4}$ signature for methane oxidation with compositions between -27 to -24 ‰ (PDB). This can be applied for the sample “Black Point” which shows a $\delta^{13}\text{C}$ in methane of -25.6 ‰ (PDB). The other two samples show slightly heavier $\delta^{13}\text{C}_{\text{CH}_4}$ contents. Methane from the mantle or deep crust is generally enriched in $\delta^{13}\text{C}_{\text{CH}_4}$ ranging between -20 to -15 ‰ (PDB) caused by an exchange at high temperatures with carbon from the mantle (Welhan, 1987). Enrichment in the δD isotopes can also be determined which express high-temperature equilibrium with water (Clark & Fritz, 1997). It is difficult to identify a precise source because the isotopic signatures for different sources are mostly equal to each other. So, the additionally gauging of hydrogen isotopes in methane can be a useful tool for characterization of the origin of the gases.

4.2.4.2 Noble isotopic composition: helium, neon, argon

Table 4-9 and Table 4-10 show the results of helium, neon, and argon isotope analyses in gas samples, measured at the INGV in 2010. In total 14 measurements from 13 gas sampling tubes (double determination for one “Black Point” sample) were performed. Hence the first 5 not contaminated samples were used to determine the content of argon isotopes.

Helium and neon concentration vary between 5.1-12.1 ppm and 0.070-0.355 ppm respectively. The helium isotopic composition is depicted as R/R_a , where R is the $^3\text{He}/^4\text{He}$ ratio in the sample and R_a is the same ratio in the atmosphere. R_a is equal to $1.39 \cdot 10^{-6}$ (Caliro et al., 2004). The determined R/R_a values range between 4.11 and 4.39. The measured argon concentrations range between 70 and 158 ppm whereby the sample from “Bottaro North” (grey highlighted) can be assumed as contaminated. Therefore it is not included in the summary. The isotopic signature $^{40}\text{Ar}/^{36}\text{Ar}$ varies between 303 and 310.

Table 4-9: Data on isotopic composition from helium and neon of collected gas samples. Highlighted samples show no typical thermal R/R_a values whereby a contamination with atmospheric air can be assumed (not attend in summary).

Sample	Type of tube	He [ppm]	Ne [ppm]	He/Ne	R/R_a	ERROR [%]
P21	INGV	5.1	0.168	30.4	4.12	0.052
Fum F	INGV	6.3	0.070	90.13	4.11	0.031
BN	TUBAF	8.1	0.277	29.1	4.29	0.035
La Calcara	INGV	3.8	0.355	10.74	4.39	0.048
BP	INGV	12.1	0.169	71.9	4.39	0.049
BP	INGV	23.5	0.289	81.4	5.30	0.059
	INGV	23.9	0.306	78.3	5.06	0.056
La Calcara	INGV	1.0	0.618	1.56	3.05	0.063
Area26	INGV	5.9	2.950	2.0	3.26	0.036
BN	TU	7.9	0.557	14.2	3.82	0.035
FumF	TU	13.1	1.427	9.20	4.14	0.036
BP	TU	23.3	1.481	15.7	4.26	0.047
La Calcara	TU	11.7	5.862	2.00	1.30	0.015
Area 26	INGV	7.2	9.630	0.75	1.51	0.023

* 1 ppm = 10^{-4} %

Table 4-10: Data on chemical and isotopic composition from argon of gas samples. Highlighted sample shows a contamination with atmospheric air.

Sample	Type of tube	^{40}Ar [ppm]	$^{40}\text{Ar}/^{36}\text{Ar}$	ERROR [%]	$^{40}\text{Ar}^*$
P21	INGV	52.9	310	0.06	1.9
Fum F	INGV	158	303	0.05	2.1
BN	TUBAF	1129	299.8	0.04	
La Calcara	INGV	70	307.5	0.09	2
BP	INGV	119.7	310	0.07	3.8

The natural concentration of helium in the atmosphere is ascertained with 0.000524 % (5.24 ppm), neon with 0.001818 % (18.18 ppm) and argon with 0.934 % (9340 ppm) after Ozima & Podosik (2002). Table 4-9 shows all helium and neon determination whereby the 8 grey highlighted samples indicate a contamination with atmospheric air. Most of these samples which are marked italic show high neon concentrations. Some defiled samples also display an atypical R/R_a -values or extremely high abnormal helium concentrations. Measurements from “Black Point” samples displayed extremely high helium concentrations (more than 23 ppm) which are not normal for Panarea probes. The reason is unknown.

The calculation of He/Ne-ratios is a useful value to identify a contamination because high neon concentrations occur in the atmosphere while fumarole gases contain low concentrations (Italiano & Nuccio (1991), Inguaggiato & Rizzo (2004), Caliro et al. (2004), Caracausi et al. (2005), Martelli et al. (2008)). He/Ne-ratio in air is approximately 0.28 (based on air saturated water measurements from Inguaggiato & Rizzo, 2004).

The helium isotopic composition is depicted as R/R_a . R/R_a -ratios in different reservoirs on earth (for example MORB or crust) are displayed in Table 4-11.

Table 4-11: Important noble isotopic signatures in different reservoirs (SCLM - Subcontinental Lithospheric Mantle, OIB – Ocean Island Basalts) which are of interest for this thesis. The ratios are declared after ^aClark et al. (1976), ^bMamyrin & Tolstikhin (1984), ^cAllègre et al. (1987, 1995), ^dGautheron & Moreira (2002), ^eBreddam & Kurz (2001), ^fOzima & Podosek (2002), ^gMarty & Humbert (1997), ^hDunai & Baur (1995), ⁱTrieloff et al. (2000).

Isotopic ratio	Atmosphere	Continental crust	MORB	SCLM	OIB
$^3\text{He}/^4\text{He}$	^a $1.39 \cdot 10^{-6}$ [1 R_a]	^b $0.02 - 0.04 \cdot 10^{-6}$ [~ 0.02 R_a]	^c $11.4 \cdot 10^{-6}$ [~ 8.2 R_a]	^d $8.5 \cdot 10^{-6}$ [~ 6.1 R_a]	^e $\leq 60 \cdot 10^{-6}$ [$\leq 43 R_a$]
$^{40}\text{Ar}/^{36}\text{Ar}$	^f 295.5	^c $\leq 170\ 000$	^g $\leq 42\ 000$	^h $\leq 17\ 000$	ⁱ $\leq 8\ 300$

Noble isotopic ratios for $^3\text{He}/^4\text{He}$ and $^{40}\text{Ar}/^{36}\text{Ar}$ in different reservoirs are (Table 4-11) display characteristic signatures for each origin. High differences between the R/R_a from the crust and the MORB (characteristic for mantle gas) allow the determination between both layers as possible source of the collected gas. The R/R_a -value for atmospheric air is by definition 1 which is between the signature for crust and MORB.

Samples from Panarea show an R/R_a -value between 4.11 and 4.39 (Table 4-9). It can be assumed that collected gases are a mixture between gas from the crust and also from mantle regions. Caliro et al. (2004) suggest a primary magmatic origin of the gases. These

values correspond with previous measurements of thermal water samples collected on Stromboli that range between 4.06 and 4.20 (Inguaggiato & Rizzo, 2004). Panarea and Stromboli belong to the same fault system (Section 2.1) whereby an isotopic relation can be assumed. It is difficult to use argon isotopic ratios to infer in different source regions like MORB, crust and atmosphere because of the high ranges within these locations. Measured isotopic ratios of argon (Table 4-10) show slightly higher signatures than the characteristic value for atmosphere with $^{40}\text{Ar}/^{36}\text{Ar}$ of 295.5 (Table 4-11).

4.2.5 Sulphur isotopes in fluids and gas

The isotopic composition of sulphate and sulphite were measured from water sampled in 2009 and 2010 at the UFZ. $\delta^{34}\text{S}$ values from sulphite in gas samples were determined as well. Additionally, 3 bio samples were investigated for elemental sulphur isotopes. All laboratory results of the sulphur isotope determinations done at the UFZ in 2011 are presented in Table A 18. Achievements from measurements in 2008 can be found in Sieland (2009). Results from $\delta^{34}\text{S}$ recordings in sulphate and sulphide accomplished with samples from 2006 and 2007 are given in Table A 19.

➤ Isotopic composition of dissolved sulphate in the water

The $\delta^{34}\text{S}$ in sulphate determined in 2008 and 2011 range between 19.8 and 23.0 ‰ (VCDT) whereas the $\delta^{18}\text{O}$ in SO_4 varies between 7.9 and 12.6 ‰ (VSMOW). Measurements arranged in 2007 show $\delta^{34}\text{S}$ signature between 20.5 and 22.4 ‰ (VCDT). All results are charted in Figure 4-22. Unfortunately $\delta^{18}\text{O}$ was not determined. The variations of sulphur and oxygen isotopes are in general low which can be taken as an evidence for the same origin of the samples. All $\delta^{34}\text{S}$ values are slightly shifted to heavier ^{34}S in the residual fraction compared to the mean isotopic composition of dissolved marine sulphate after Fritz & Fontes (1989) presenting a $\delta^{34}\text{S}$ value for marine sulphate of 20.0 ± 0.25 ‰ and a corresponding $\delta^{18}\text{O}$ in SO_4 of 9.45 ± 0.15 ‰. Rees et al. (1978) report a $\delta^{34}\text{S}$ signature for seawater of 21‰ (VCDT). Especially samples analysed in 2011 are slightly shifted to higher $\delta^{34}\text{S}$ contents. It can be assumed that a biogenic reduction of the sulphate caused this offset.

Variability in $\delta^{18}\text{O}$ -values of sulphate can be caused by hydrothermal H_2S gas in contact with dissolved oxygen in aerobic water. It oxidized to sulphate in an extremely fast reaction of the first order and affects the isotopic $\delta^{18}\text{O}$ signature (Fritz & Fontes, 1989).

It can be assumed that the isotopic signature of oxygen dissolved in the water is created from sulphides and the original sulphates dissolved in the hydrothermal water.

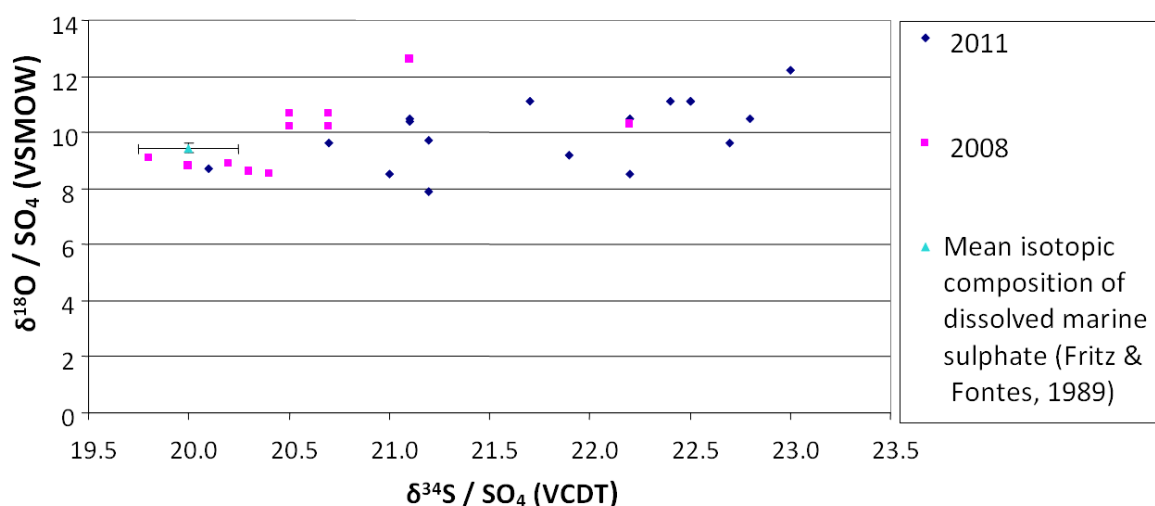


Figure 4-22: Isotopic composition $\delta^{34}\text{S}$ and $\delta^{18}\text{O}$ of sulphate in water samples.

➤ Isotopic composition of sulphides in water and gas

$\delta^{34}\text{S}$ values are displayed in Figure 4-23 and Table 4-12 showing the mean value and standard diversity of measurements from samples collected in 2006 to 2011.

Table 4-12: Calculated mean values and standard deviations for each diving location. Corresponding samples were collected from 2006 to 2011. The number of probes is displayed in brackets.

Location	Mean $\delta^{34}\text{S}$ [‰VCDT]	STDEV
BP (5)	3.67	0.70
HL/FumF (8)	2.08	0.66
BN (4)	0.63	0.76
P21 (5)	0.16	0.95
Area26 (4)	-0.48	1.73
BW (2)	2.54	0.36
La Calcara (1)	0.65	0.00

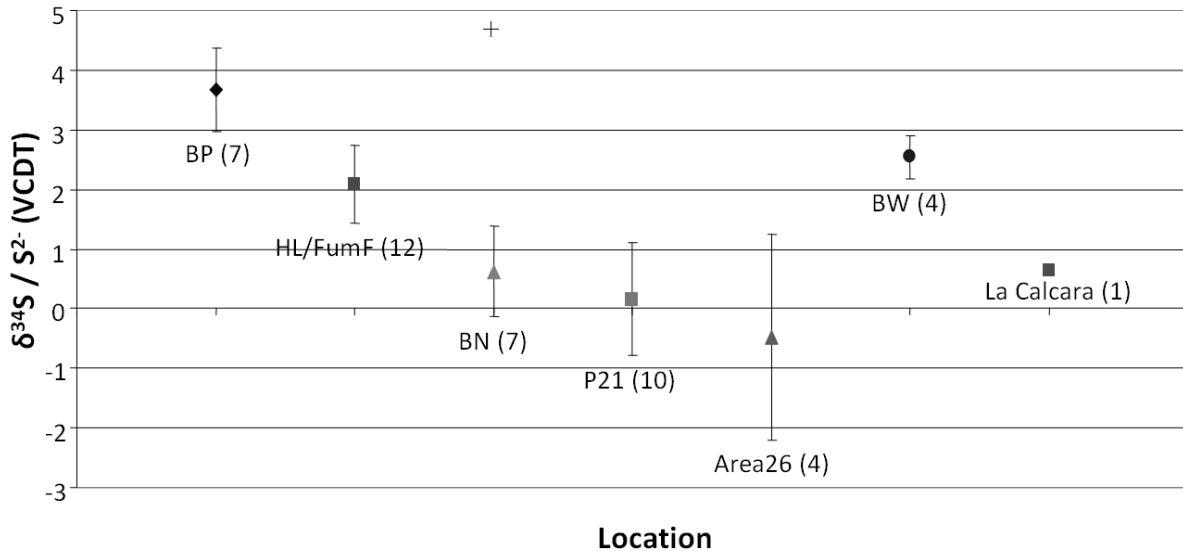


Figure 4-23: Isotopic composition $\delta^{34}\text{S}$ of sulphite in gas and water samples collected in 2006, 2007, 2009 and 2010 analyzed at the UFZ. Each diving location is shown separately, number of samples is displayed in brackets. For the location “Bottaro North” an outlier is displayed which is not considered in the calculated mean value.

Measurements from 2008 revealed $\delta^{34}\text{S}$ values of sulphide in water samples for “Black Point” with $3.19 \pm 0.02 \text{ ‰}$ (VCDT), from “Bottaro North” with $1.37 \pm 0.16 \text{ ‰}$ (VCDT) and from “Hot Lake” probes amounts of $3.01 \pm 0.07 \text{ ‰}$ respectively $2.26 \pm 0.08 \text{ ‰}$ (VCDT) according to Sieland (2009). These values correlate with the results from 2011 shown in Figure 4-23. $\delta^{34}\text{S}$ of sulphide in “Black Point” and “Bottaro West” present positive values of 3 ‰ (VCDT) whereas “Point 21”, “Area 26” and “La Calcara” has $\delta^{34}\text{S}$ values around -2 to 1 ‰ (VCDT). The highest spreading show 4 samples collected in “Bottaro North” which varies between -0.7 and 4.8 ‰ (VCDT).

The $\delta^{34}\text{S}$ isotopic signature of magmatic gases and MORB sulphur are reported with 0 ‰ (VCDT) after Sakai et al. (1984) and Cortecchi et al. (2005). The same isotopic ratio caused by rock leaching was determined by Rouxel et al. (2004). Previous perceptions from Ueda & Sakai (1984), Alt et al. (1993) propose a $\delta^{34}\text{S}$ about 10 ‰ (VCDT) for island arc magmatic rocks. $\delta^{34}\text{S}$ of sulphides in back-arc basins is determined between -0.2 to 7.7 ‰ (VCDT) by Yang & Scott (2006). These references agree with the isotopic $\delta^{34}\text{S}$ -ratios occurring in Panarea samples. It can also be assumed that processes like oxidation of the sulphides caused by dissolved molecular oxygen or micro organisms influence the isotopic signatures.

➤ Isotopic composition of bio samples

The isotopic ratio $\delta^{34}\text{S}$ from 3 bio samples was investigated at the UFZ by measuring the chromium reducible sulphur (CRS) which determines the reduced inorganic sulphur species (sulphides and sulphur) excluding sulphates and organic sulphur. The results range between -3.6 and -2.4 ‰ (VCDT). In September 2006 bacteria probes from “Point 21”, “Bottaro North” and “Hot Lake” were investigated. All results are shown in Table 4-13.

Table 4-13: Measured bacteria mats for sulphur isotopes.

Location	$\delta^{34}\text{S}_{\text{sulphide}}$ [‰VCDT]
PAN-P21-08092010_BIO	-3.6
PAN-P21-08092010_BIO2	-2.4
elemental Sulfur 2010	-3.3
Bottaro_0906	-0.9
PANS3 P21_110906	-1.7
PANS2 BN_110906	-2.3
PANS1 P21_110906	-2.4

These values are in good agreement with data from Peters et al. (2011) reporting $\delta^{34}\text{S}_{\text{CRS}}$ from Panarea sediments in the range between -11.3 and -1.8 ‰ (VCDT). They assume that the sulphur is a mixture between hydrothermal and biogenic sulphide whereby the biogenic component is more dominant (Peters et al., 2011). Occurring micro organisms oxidize sulphide to sulphate and hydrogen by accumulating seawater. The isotopic signature is shifting to heavier isotopic ratios in the residual fraction.

5 FINAL DISCUSSION AND CONCLUSION

➤ Thermodynamic measurements

The first goal of this work was to create results with respect to temperature gradient, thermal conductivity and heat flux quantifications with the modified and new sensors. The prototypes worked well under water and under these tough conditions (high temperatures and salinity); first records were taken successfully and parameters of locations with soft ground were obtained. Some errors during the field measurements were caused by the high heterogeneity of the geothermal system. "Hot spots" (maximum temperature > 130 °C, "La Calcara") were identified. The majority of them are characterized by upwelling hydrothermal water and gas next to "cool" spots (around 21 °C, close to seawater temperature). To take precise readings with the different devices, temperature gradient and heat flux measurements have to be performed at the same spot. Especially in deeper diving locations such as "Area 26", it was difficult to complete the measurements because of the limited diving time. Sometimes, ground time was just a few minutes. Otherwise, additional decompression time has to be scheduled. Water turbulence initiated by divers moving around is another problem. Putting the sensors in place also changes the temperature regime (during the recess into the sediment, for example). These sources of error can be minimized by an attentive working method and an adequate time frame for the adaption of the measuring instruments to the natural conditions.

For further field measurements with these sensors it is recommended to remeasure along a monitoring network with exactly identified sites. Replicated determinations and observation will result in more reliable readings. Further statistical analysis can provide an assumption of the records' accuracy. Interesting but challenging diving locations are "La Calcara" and "Hot Lake" because of their high sediment surface temperatures (maximum temperature of 135 °C in a depth of 500 mm at "La Calcara", Figure 4-6). The sediment depth at these same locations is sufficiently thick for a complete insertion of the probe. Additionally, the thermometry of the sediment surface temperature has to be accomplished to obtain more precise data for calculating the case of "natural convection" (Section 4.1.1). Measurements conducted with the heat flux plate integrate the influence of convection and conduction. In prospective field work the heat flux at "hot spots" should be quantified using two setups: one reading is to be done only with the heat flux plate and a second reading with the heat

flux plate surrounded by a cover (size app. 1 x 1 m) to evaluate the impact of the upwelling geothermal fluid on the readings.

➤ Isotopic measurements

The second aim was to compare stable and noble isotopic determinations of collected gas and water samples. Differences were found especially between ($\delta\text{D}/\delta^{18}\text{O}$)-analyses (Section 4.2.2.1) performed parallel in two laboratories: the results of δD from INGV are in general 1.3 ‰ lower than those of UFZ. The variances of $\delta^{18}\text{O}$ differ only by 0.5 ‰. The used methods and instruments diverge and this might be the explanation for the differences. In any case, it is hard to assign a favoured technique. The time span between sampling and actual measuring varies from 2 and 3 weeks (INGV), respectively, to 6 months (UFZ) which is a reasonable argument as well for the observed deviances.

The diving location “La Calcara” is not only interesting for thermodynamic measurements. Heavy $\delta^{13}\text{C}$ values (Figure 4-21) in water samples were found. Such heavy $\delta^{13}\text{C}$ values of more than 20 ‰ are not reported in the literature so far. It is speculated that the heavy ^{13}C values are due to Messinian crisis evaporates. Samples from this diving spot also show (O/D)-contents which assume high concentrations of magmatic water (around 30 %, see Figure 4-19). The analysis of $\delta^{13}\text{C}_{\text{CH}_4}$ in gas samples does not allow an unambiguous determination of the origin of the methane. The characteristic $\delta^{13}\text{C}_{\text{CH}_4}$ signatures of potential sources overlap. To provide more precise indications the investigation of $\delta^2\text{H}_{\text{CH}_4}$ is recommended.

Determined sulphur and oxygen isotopes of sulphate in water and gas show a general low variation which confirms the same origin of the samples. All $\delta^{34}\text{S}$ values exceed the ones after Fritz & Fontes (1989) by 1 to 3 ‰ declaring a $\delta^{34}\text{S}$ for dissolved marine sulphate of 20.0 ± 0.25 ‰ and a corresponding $\delta^{18}\text{O}$ of 9.45 ± 0.15 ‰.

The isotopic signature of $\delta^{34}\text{S}$ in sulphide from back-arc basins determined by Yang & Scott (2006) varies between -0.2 and 7.7 ‰ (VCDT) which is confirmed by the isotopic $\delta^{34}\text{S}$ -ratios measured in Panarea samples, ranging from -0.48 (“Area 26”) to 3.67 (“Black Point”).

Another interesting tool to gather information about the migration and origin of the gases is the determination of noble gases, like helium and argon. Within this thesis it could be

verified that the isotopic signature of helium (R/R_a between 4.11 and 4.39) is an evidence of a mixed gas ascending from the crust and the mantle (Section 4.2.3.2).

The idea to establish a measuring network for thermodynamic recordings is also interesting for isotopic analysis. Water and gas sampling could be arranged within this observational network assuming that hydrothermal emissions occur within this graticule.

REFERENCES

- ALLÈGRE, C. J., STAUDACHER, T., SARDA, P. (1987): Rare gas systematics: formation of the atmosphere, evolution and structure of the earth's mantle. *Earth and Planetary Science Letters*, 81, 127–150.
- ALLÈGRE, C. J., MOREIRA, M., STAUDACHER, T. (1995): $^3\text{He}/^4\text{He}$ dispersion and mantle convection. *Geophysical Research Letters*, 22, 2.325–2.328.
- ALT, J.C., SHANKS III, J.C., JACKSON, M.C. (1993): Cycling of sulfur in subduction zones: the geochemistry of sulfur in the Mariana Island Arc and back-arc trough. *Earth and Planetary Science Letters*, 119, 477–494.
- ANZIDEI, M. (2000): Rapid bathymetric surveys in marine volcanic areas: a case study in Panarea area. *Physics and Chemistry of the Earth*, 25, 77–80.
- BALLENTINE, C.J., BURNARD, P.G. (2002): Production, release and transport of noble gases in the continental crust. In: Porcelli, D., Ballentine, C.J., and Weiler, R. (Eds.): Reviews in mineralogy and geochemistry—Noble gases in geochemistry and cosmochemistry. Volume 47: Washington, D.C., *Mineralogical Society of America*, 481–538.
- BARKER, J.F., FRITZ, P. (1981): Carbon isotope fractionation during microbial methane oxidation. *Nature*, 293, 289–291.
- BARBERI, F., GANDINO, A., GIONCADA, A., LA TORRE, P., SBRANA, A., ZENUCCHINI, C. (1994): The deep structure of the Eolian arc (Filicudi-Panarea-Vulcano sector) in light of gravity, magnetic and volcanological data. *Journal of Volcanology and Geothermal Research*, 61, 189–206.
- BECCALUVA, L., ROSSI, P. L., SERRI, G. (1982): Neogene to recent volcanism of the Southern Tyrrhenian-Sicilian area: Implications for the geodynamic evolution of the Calabrian Arc, *Earth Evolution Sciences*, 3, 222–238.
- BECCALUVA, L., GABBIANELLI, G., LUCCHINI, F., ROSSI, P. L., SAVELLI, C. (1985): Petrology and K/Ar ages of volcanic dredged from the Eolian seamounts: Implications for geodynamic evolution of the Southern Tyrrhenian basin, *Earth and Planetary Science Letters*, 74, 187–208.
- BOLOGNESI, L., D'AMORE, F. (1993): Isotopic variation of the hydrothermal system on Vulcano Island, Italy. *Geochimica et Cosmochimica Acta*, 57, 2069–2082.
- BONACCORSO, A. (2002): Ground deformation of the southern sector of the Aeolian Islands volcanic arc from geodetic data, *Tectonophysics*, 351, 181–192.
- BREDDAM, K., KURZ, M. D. (2001): Helium isotope signatures of Icelandic alkaline lavas. *Eos, Transactions, American Geophysical Union*, 82, FM 1.315.

- BROWN, E., COLLING, A., PARK, D., PHILLIPS, J., ROTHERY, D., WRIGHT, J. (1995): Seawater: Its Composition, Properties and Behaviour, *Kidlington, Pergamon*, 2nd edition, 168.
- BULLARD, E.C. (1939): Heat Flow in South Africa, *Proc. R. Soc. London A*, 173, 474-502.
- CALANCHI, N., CAPACCIONI, B., MARTINI, M., TASSI, F., VALENTINI, L. (1995): Submarine gas-emission from Panarea Island Aeolian Archipelago: distribution of inorganic and organic compounds and inferences about source conditions. *Acta Vulcanologica*, 7, 43–48.
- CALANCHI, N., TRANNE, C.A., LUCCHINI, F., ROSSI, P.L., VILLA, I.M. (1999): Explanatory notes to the geological map (1:10.000) of Panarea and Basiluzzo islands (Aeolian arc. Italy), *Acta Vulcanologica*, 11 (2), 223– 243.
- CALANCHI, N., A. PECCERILLO, C. A. TRANNE, F. LUCCINI, P. L. ROSSI, P. KEMPTON, M. BARBIERI (2002): Petrology and geochemistry of volcanic rocks from the island of Panarea: Implications for mantle evolution beneath the Aeolian island arc (Southern Tyrrhenian Sea), *Journal of Volcanology and Geothermal Research*, 115, 367–395.
- CALIRO, S., CARACAUSI, A., CHIODINI, G., DITTA, M., ITALIANO, F., LONGO, M., MINOPOLI, C., NUCCIO, P. M., PAONITA, A., RIZZO, A. (2004): Evidence of a recent input of magmatic gases into the quiescent volcanic edifice of Panarea, Aeolian Islands, Italy. *Geophysical Research Letters*, 31, -.
- Canet, C., PROL-LEDESMA, R. M., PROENZA, J. A., RUBIO-RAMOS, M. A., FORREST, M. J., TORRES-VERA, M. A., RODRÍGUEZ-DÍAZ, A. A. (2005): Mn–Ba–Hg mineralization at shallow submarine hydrothermal vents in Bahía Concepción, Baja California Sur, Mexico. *Chemical Geology*, 224, 96–112.
- CAPACCIONI, B., TASSI, F., VASELLI, D., TEDESCO, D., ROSSI, P.L. (2005): The November 2002 degassing event at Panarea Island (Italy): the results of a 5 months geochemical monitoring program. *Annales Geophysicae*, 48, 755–765.
- CAPACCIONI, B., TASSI, F., VASELLI, D., TEDESCO, D., POREDA, R. (2007): Submarine gas burst at Panarea Island (Southern Italy) on 3 November 2002: a magmatic versus hydrothermal episode. *Journal of Geophysical Research-Solid Earth*, 112, 1-15.
- CAPASSO, G., DONGARRA, G., FAVARA, R., HAUSER, S. & VALENZA, M. (1992): Isotope Composition of Rain Water, Well Water and Fumarole Steam on the Island of Vulcano, and Their Implications for Volcanic Surveillance. *Journal of Volcanology and Geothermal Research*, 49, 147-155.
- CAPASSO, G., FAVARA, R., INGUAGGIATO, S. (1997): Chemical features and isotopic composition of gaseous manifestations on Vulcano Island, Aeolian Islands, Italy: An interpretative model of fluid circulation. *Geochimica et Cosmochimica Acta*, 61, 3425-3440.

- CAPASSO, G., FAVARA, R., GRASSA, F., INGUAGGIATO, S., LONGO, M. (2005): Online technique for preparing and measuring stable carbon isotope of total dissolved inorganic carbon in water samples ($\delta^{13}\text{C}$ (TDIC)). *Annals of Geophysics*, 48, 159-166.
- CARACAUSSI, A., DITTA, M., ITALIANO, F., LONGO, M., NUCCIO, P.M., PAONITA, A., RIZZO, A. (2005): Changes in fluid geochemistry and physico-chemical conditions of geothermal systems caused by magmatic input: The recent abrupt outgassing off the island of Panarea (Aeolian Islands, Italy). *Geochimica et Cosmochimica Acta*, 69 (12), 3045-3059.
- CARLSLAW, H.S., JAEGER, J.C. (1959): Conduction of heat in solids. *Oxford University Press*, USA, 2nd edition, 510 pp.
- CAS, R., GIORDANO, G., ESPOSITO, A., BALSAMO, F. (2007): Hydrothermal breccia textures and processes: Lisca Bianca Islet, Panarea, Aeolian Islands, Italy. *Breccia Symposium – Economic Geology Research Unit*, James Cook University, Townsville, Australia.
- CAVAZZA, W., WEZEL, F.C. (2003): The Mediterranean region – a geological primer. *Episodes*, 26, 160–168.
- CHIODINI, G. (2009): CO_2/CH_4 ratio in fumaroles a powerful tool to detect magma degassing episodes at quiescent volcanoes *Geophysical Research Letters*, 36, L02302.
- CHIODINI, G., CALIRO, S., CARAMANNA, G., GRANIERI, D., MINOPOLI, C., MORETTI, R., PEROTTA, L., VENTURA, G. (2006): Geochemistry of the submarine gaseous emissions of Panarea (Aeolian Islands, Southern Italy): Magmatic vs. hydrothermal origin and implications for volcanic surveillance. *Pure and Applied Geophysics*, 163, 759-780.
- CHIODINI, G., ALLARD, P., CALIRO, S., PARELLO, F. (2000): O-18 exchange between steam and carbon dioxide in volcanic and hydrothermal gases: Implications for the source of water. *Geochimica Et Cosmochimica Acta*, 64, 2479-2488.
- CHIODINI, G., CIONI, R., MARINI, L., PANICHI, C. (1995): Origin of the fumarolic fluids of Vulcano Island, Italy and implication for volcanic surveillance. *Bulletin of Volcanology*, 57, 99–110.
- CHUHAN, F.A., KJELDSTAD, A., BJØRLYKKE, K., HØEG, K. (2002): Porosity loss in sand by grain crushing – experimental evidence and relevance to reservoir quality. *Marine and Petroleum Geology*, 19, 39-53.
- CLARK, I.D., FRITZ, P. (1997): Environmental isotopes in Hydrogeology. Lewis Publishers, Boca Raton, New York.
- CLARK, W. B., JENKINS, W. J., TOP, Z. (1976): Determination of tritium by mass spectrometric measurement of ^3He . *The International Journal of Applied Radiation and Isotopes*, 27, 515 – 522.

- CLAUSER, C. (1992): Permeability of crystalline rocks, *EOS Trans. American Geophysical Union*, 73(21), 233-237.
- CLAUSER, C., HUENGES, E. (1995): Thermal conductivity of rocks and minerals, *Rock Physics and Phase Relations – A Handbook of Physical Constants, AGU Reference Shelf*, 3, 105-126.
- CONTINISIO, R., FERRUCCI, F., GAUDIOSI, G., LO BASCIO, D., VENTURA, G. (1997): Malta Escarpment and Mt. Etna: Early stages of an asymmetric rifting process? Evidences from geophysical and geological data. *Acta Vulcanologica*, 9, 39–47.
- CORTECCI, G., BOSCHETTI, T., MUSSI, M., LAMELI, C. H., MUCCHINO, C., BARBIERI, M. (2005): New chemical and original isotopic data on waters from El Tatio geothermal field, northern Chile. *Geochemical Journal*, 39, 547-571.
- CRAIG, H. (1961): Isotopic variations of meteoric waters. *Science* 133, 1702-1708.
- CRISCI, G. M., DE ROSA, R., ESPERANCA, S., MAZZUOLI, R., SONNINO, M. (1991): Temporal evolution of a three component system: The Island of Lipari (Aeolian Arc, southern Italy). *Bulletin of Volcanology*, 53, 207 – 221.
- D'ALESSANDRO, W., Salvatore GIAMMANCO, S., BELLOMO, S., PARELLO, F. (2007): Geochemistry and mineralogy of travertine deposits of the SW flank of Mt. Etna (Italy): Relationships with past volcanic and degassing activity. *Journal of Volcanology and Geothermal Research*, 165, 64–70.
- DANDO, P. R., STUBEN, D., VARNAVAS, S. P. (1999): Hydrothermalism in the Mediterranean Sea. *Progress in Oceanography*, 44, 333-367.
- DE ASTIS, G., LA VOLPE, L., PECCERILLO, A., CIVETTA, L. (1997a): Volcanological and petrological evolution of Vulcano Island (Aeolian Arc, Southern Tyrrhenian Sea). *Journal of Geophysical Research*, 102, 8021–8050.
- DE ASTIS, G., DELLINO, P., DE ROSA, R., LA VOLPE, L. (1997b): Eruptive and emplacement mechanisms of widespread fine-grained pyroclastic deposits on Vulcano Island (Italy). *Bulletin of Volcanology*, 59, 87–102.
- DE ASTIS, G., VENTURA, G., VILARDO, G. (2003): Geodynamic significance of the Aeolian volcanism (Southern Tyrrhenian Sea, Italy) in light of structural, seismological and geochemical data. *Tectonics*, 22 (4), 1040.
- DE LUCA, G., FILIPPI, L., CACCAMO, D., NERI, G., SCARPA, R. (1997): Crustal structure and seismicity of Southern Tyrrhenian basin. *Physics of the Earth and Planetary Interiors*, 103, 117 – 133.
- DICKEN, A.P. (1995): Radiogenic Isotope Geology. *Cambridge University Press*, New York, p. 452.

DOLFI, D., DE RITA, D., CIMARELLI, C., MOLLO, S., SOLIGO, M., FABBRI, M. (2007): Dome growth rates, eruption frequency and assessment of volcanic hazard: insights from new U/Th dating of the Panarea and Basiluzzo dome lavas and pyroclastics, Aeolian Islands, Italy. *Quaternary International*, 162–163, 182–194.

DUNAI, T.J. & BAUR, H. (1995): Helium, neon and argon systematics of the European subcontinental mantle: Implications for its geochemical evolution. *Geochimica et Cosmochimica Acta*, Oxford, 59(13), 2767–2783.

EPSTEIN, S., MAYEDA, T. (1953): Variation of O18 content of waters from natural sources. *Geochimica et Cosmochimica Acta*, 4, 213–224.

ESPOSITO, A., GIORDANO, G., ANZIDEI, M. (2006): The 2002–2003 submarine gas eruption at Panarea volcano (Aeolian Islands, Italy): Volcanology of the seafloor and implications for the hazard scenario. *Marine Geology*, 227, 119–134.

ESPOSITO, A., ANZIDEI, M., ATZORI, S., DEVOTI, R., GIORDANO, G., PIETRANTONIO, G. (2010): Modeling ground deformations of Panarea volcano hydrothermal/geothermal system (Aeolian Islands, Italy) from GPS data. *Bulletin of Volcanology*, 72, 609–621.

ETHERIDGE, M.A., WALL, V.J., VERON, R.H. (1983): The role of the fluid phase during regional metamorphism and deformation. *Journal of Metamorphic Geology*, 1, 205–226.

FAURE, G. (1986): Principles of Isotope Geology. 2nd edition. Ed. J. Wiley & Sons. New York. P. 590.

FAURE, G. (1986a): The K-Ar method of dating, in *Principles of Isotope Geology*, second edition, John Wiley, New York, 66–92.

FAVALLI, M., KARATSON, D., MAZZUOLI, R., PARESCHI, M. T., VENTURA, G. (2005): Volcanic geomorphology and tectonics of the Aeolian archipelago (Southern Italy) based on integrated DEM data. *Bulletin of Volcanology*, 68, 157–170.

FAVARA, R., GRASSA, F., INGUAGGIATO, S. (1999): Chemical and isotopic features of dissolved gases from thermal springs of Sicily. Proceedings of The Fifth International Symposium on the Geochemistry of the Earth's Surface, GES-5 Reykjavik, Iceland, 495–498.

FAVARA, R., INGUAGGIATO, S. (2000): Proceedings of the IAVCEI General Assembly 2000. Bali, Indonesia, 83.

FAVARA, R., GRASSA, F., INGUAGGIATO, S., PECORAINO, G., CAPASSO, G. (2002): A simple method to determine the $\delta^{13}\text{C}$ content of total dissolved inorganic carbon. *Geofisica Internazionale*, 41 (3), 313–320.

FINETTI, I., DEL BEN, A. (1986): Geophysical study of the Tyrrhenian opening. *Bolletino di Geofisica Teorica ed Applicata*, XXVIII, 110 pp.

FORNASERI, M. (1984): Lezioni di geochimica. Veschi Ed., p. 824.

- FREW, R. D., DENNIS, P. F., HEYWOOD, K. J., MEREDITH, M. P., BOSWELL, S. M. (2000): The oxygen isotope composition of water masses in the northern North Atlantic. *Deep-Sea Research Part I-Oceanographic Research Papers*, 47, 2265-2286.
- FRITZ, P., FONTES, J. C. (Eds.) (1989): *Handbook of Environmental Isotope Geochemistry*, Vol. 3: The Marine Environment. A., Elsevier Science Publishers B.V., Amsterdam.
- GABBIANELLI, G., GILLOT, P.Y., LANZAFAME, G., ROMAGNOLI, C., ROSSI, P.L. (1990): Tectonic and volcanic evolution of Panarea (Aeolian Island, Italy). *Marine Geology*, 92, 312–326.
- GABBIANELLI, G., ROMAGNOLI, C., ROSSI, P.L., CALANCHI, N. (1993): Marine geology of Panarea–Stromboli area, Aeolian Archipelago, South-eastern Tyrrhenian Sea. *Acta Vulcanologica*, 3, 11–20.
- GAMBERI, F., MARANI, P.M., SAVELLI, C. (1997): Tectonic volcanic and hydrothermal features of submarine portion of Aeolian arc (Tyrrhenian Sea). *Marine Geology*, 140, 167–181.
- GAT, J. R., CARMI, I. (1970): Evolution of the isotopic composition of atmospheric waters in the Mediterranean Sea area. *Journal of Geophysical Research*, 75, 3039-3048.
- GAUTHERON, C., MOREIRA, M. (2002): Helium signature of the subcontinental lithospheric mantle. *Earth and Planetary Science Letters*, 199, 39–47.
- GIGGENBACH, W. F. (1992): Isotopic shifts in waters from geothermal and volcanic systems along convergent plate boundaries and their origin. *Earth and Planetary Science Letters*, 113, 495-510.
- GILLOT, P. Y. (1987): Histoire volcanique des Iles Eoliennes: Arc insulaire or complexe orogenique anulaire?. *Dissertation thesis*, Paris University, Paris.
- GRASSA, F., CAPASSO, G., FAVARA, R., INGUAGGIATO, S. (2006): Chemical and isotopic composition of waters and dissolved gases in some thermal springs of Sicily and adjacent volcanic islands, Italy. *Pure and Applied Geophysics*, 163, 781-807.
- GROßMANN, E.L., CIFUENTES, L.A., COZZARELLI, I.M. (2002): Anaerobic methane oxidation in a landfill-leachate plume. *Environmental Science & Technology*, 36(11), 2436-2442.
- GROßMANN, K. (1993): Neue Wege für das Ermitteln der effektiven Schüttgut-Wärmeleitfähigkeit und für die indirekte Gutfeuchtebestimmung. Fortschrittberichte VDI, 3 (314), VDI-Verlag GmbH/Düsseldorf – ISBN 3-18-141403-4.
- GUGLIANDOLO, C., ITALIANO, F., MAUGERI, T. L. (2006): The submarine hydrothermal system of Panarea (Southern Italy): biogeochemical processes at the thermal fluids-sea bottom interface. *Annals of Geophysics*, 49, 783-792.
- HAMEL, M. (2010): Investigation and modelling of the geochemical processes in the hydrothermal system of Panarea, Italy. *Department for Geology (Section Hydrogeology)*, Vol. 25, FOG ISSN 1434-7512.

- HALISCH, M., TIETZE, K. (2005): Aufbau, Test und Einsatz einer TK04-Apparatur zur Messung der Wärmeleitfähigkeit von Gesteinsproben mit der Methode des instationären Wärmestroms. Institut für Geowissenschaftliche Gemeinschaftsaufgaben (GGA-Institut), Hannover. report, p. 51.
- HANETZOG, K. (2011): Isotopic signature of samples waters on Lipari, Italy. *Department of Geology (Section Hydrogeology)*, diploma thesis, TU Bergakademie Freiberg, heretofore unpublished.
- HOEFS, J. (1987): Stable isotopes geochemistry. 3rd edition, Ed. Springer-Verlag, New York, p. 224.
- HOEFS, J. (1997): Stable isotope geochemistry. Springer-Verlag Berlin, p. 201.
- HOPMANS, J.W., DANE, J.H. (1986): Thermal conductivity of two porous media as a function of water content, temperature, and density. *Soil Science*, 142 (4), 187-195.
- HORNIG-KJARSGAARD, I., KELLER, J., KOBERSKI, U., STADLBAUER, E., FRANCALANCI, L., LENHART, R. (1993): Geology, stratigraphy and volcanological evolution of the island of Stromboli, Aeolian arc, Italy. *Acta Vulcanologica*, 3, 21–68.
- HÖLTING, B., COLDEWEY, G. (2005): Hydrogeologie, Einführung in die Allgemeine und Angewandte Hydrogeologie. *ELSEVIER/ Spektrum Akademischer Verlag*, 6. edition, ISBN: 978-3-8274-1526-4.
- HSÜ, K. J., RYAN, W. B. F., CITA, M. B. (1973): Late Miocene desiccation of the Mediterranean. *Nature*, 242, 240–244.
- INGUAGGIATO, S., RIZZO, A. (2004): Dissolved helium isotope ratios in ground-waters: a new technique based on gas–water re-equilibration and its application to Stromboli volcanic system. *Applied Geochemistry*, 19, 665–673.
- INGUAGGIATO, S., PECORAINO, G., D'AMORE, F. (2000): Chemical and isotopical characterisation of fluid manifestations of Isshia Island (Italy). *Journal of Volcanology and Geothermal Research*, 99 (1-4), 151-178.
- ITALIANO, F., NUCCIO, P.M. (1991): Geochemical investigations of submarine volcanic exhalations to the east Panarea, Aeolian Islands, Italy. *Journal of Volcanology and Geothermal Research*, 46, 125–141.
- JESSOP, A. M. (1990): Thermal geophysics. *Elsevier*, Amsterdam, 316 pp.
- JORDAN, H., PILOT, J., SCHÖPE, M., SCHULZE, H. (1979): Edelgasisotope in der Hydrogeologie. Freiburger Forschungsheft C 343, *Deutscher Verlag für Grundstoffindustrie*, Leipzig, 84, p. 19.
- KELLER, J. (1980): The Island of Salina. *Rendiconti della Societa Italiana di Mineralogia e Petrologia*, 36, 489–524.

- KEPPIE, D.F., CURRIE, C.A., WARREN, C. (2009): Subduction erosion modes: Comparing finite element numerical models. *Earth and Planetary Science Letters*, 287, 241–254.
- KIPFER, R. (1991): Primordiale Edelgase als Tracer für Fluide aus dem Erdmantel. *Dissertation thesis*, ETH No. 9463, ETH Zürich.
- KORENAGA, J., KELEMEN, P.B., (1998): Melt migration through the oceanic lower crust: a constraint from melt percolation modeling with finite solid diffusion. *Earth and Planetary Science Letters*, 156(1–2), 1–11.
- KOSCHKE, P., HÜTTL, W., RINN, C. (2009): Ahlborn ALMEMO® Handbook Mess- und Regelungstechnik GmbH, 8. überarbeitete Auflage, Holzkirchen, Germany
- KOSUGE, T., GAO, D., HOSHINO, T. (2000): Analysis of the Methionine Biosynthetic Pathway in the Extremely Thermophilic Eubacterium *Thermus thermophilus*. *Journal of Bioscience and Bioengineering*, 90 (3), 271-279.
- KRISCHER, O (1934): Der Einfluss der Feuchtigkeit, Körnung und Temperatur auf die Wärmeleitfähigkeit körniger Stoffe. (Die Leitfähigkeit des Erdbodens) München, Beiheft zum Gesundheits-Ingenieur, 1, 33.
- KURZ, M.D., JENKINS, W.J., SCHILLING, J.G., HART, S.R. (1982): Helium isotopic variations in the mantle beneath the North Atlantic Ocean. *Earth and Planetary Science Letters*, Amsterdam, 58, 1-14.
- LANZAFAME, G., BOUSQUET, J. C. (1997): The Maltese escarpment and its extension from Mt. Etna to Aeolian Islands (Sicily): Importance and evolution of a lithospheric discontinuity. *Acta Vulcanologica*, 9, 121–135.
- LEIDIG, M., BARTH, G. (2009): Underwater Temperature Measurement – the underestimated Basis for various Scientific Projects – an Example for Panarea, Italy, 1. *International Workshop on Research in Shallow Marine and Fresh Water Systems, May, 14-16*, Technical University Bergakademie Freiberg, Institute for Geology, 119-124.
- LILLIE, R. J. (1999): Whole Earth Geophysics : An Introductory Textbook for Geologists and Geophysicists. *Prentice Hall, Inc., Englewood Cliffs, New Jersey*, 361.
- LIOTTA, M., FAVARA, R., VALENZA, M. (2006): Isotopic composition of the precipitations in the central Mediterranean: Origin marks and orographic precipitation effects. *Journal of Geophysical Research*, 111, 1-12.
- LUCCHI, F., TRANNE, C.A., CALANCHI, N., KELLER, J., ROSSI, P.L. (2003): Geological map of Panarea and minor islets (Aeolian Islands). University of Bologna, University of Freiburg and INGV, L.A.C. Firenze.
- LOCARDI, E., NAPPI, G. (1979): Tettonica e vulcanismo recente nell'isola di Lipari (implicazioni geodinamiche), *Bolletino della Società Geologica Italiana*, 98, 447–456.

- MAMYRIN, B. A. & TOLSTIKHIN, I. N. (1984): Helium Isotopes in Nature. Elsevier, Amsterdam, p. 273.
- MANETTI, P., PASQUARÉ, G., A. TIBALDI, A., TSEGAYE, A. (1989): Geologia dell'isola di Alicudi (Arcipelago delle Eolie), *Bollettino del Gruppo Nazionale per la Vulcanologia (GNV)*, 2, 903-915.
- MANETTI, P., PASQUARÉ, G., TIBALDI, A. E., TSEGAYE, A. (1995): Geology, structure and evolution of Alicudi island, Aeolian Volcanic Arc, Italy. *Acta Vulcanologica*, 7, 7–12.
- MARANI, M. P., TRUA, T. (2002): Thermal constriction and slab tearing at the origin of a superinflated spreading ridge: Marsili volcano (Tyrrhenian Sea). *Journal of Geophysical Research*, 107(B9), 2188.
- MARTELLI, M., CARACAUSI, A., PAONITA, A., RIZZO, A. (2008): Geochemical variations of air-free crater fumaroles at Mt Etna: New inferences for forecasting shallow volcanic activity. *Geophysical Research Letters*, 35, L21302.
- MARTY, B., HUMBERT, F. (1997): Nitrogen and argon isotopes in oceanic basalts. *Earth and Planetary Science Letters*, 152, 101–112.
- MAZZUOLI, R., TORTORICI, L., Ventura, G. (1995): Oblique rifting in Salina, Lipari and Vulcano Islands (Aeolian Islands, Southern Tyrrhenian Sea, Italy), *Terra Nova*, 7, 444–452.
- McKENZIE, J.A., RICCIUTO, T.E. (1978): Stable Isotopic Investigation of Carbonate Samples Related to the Messinian Salinity Crisis from DSDP Leg 42A, Mediterranean Sea. *Deep Sea Drilling Project Initial Reports*, 42 (1), 650-655.
- MERKEL, B. & PLANER-FRIEDRICH, B. (2002): Grundwasserchemie - Praxisorientierter Leitfaden zur numerischen Modellierung von Beschaffenheit, Kontamination und Sanierung aquatischer Systeme, Berlin, Springer-Verlag.
- MILLERO, F. J. (2006): Chemical Oceanography - Third Edition, Boca Raton, Taylor & Francis Group.
- MOOK, W.G. (Ed.) (2000): UNESCO/IAEA Serials on Environmental Isotopes in the Hydrological Cycle, Principles and Applications. Volume I, Centre for Isotope Research Groningen, SC-2000/WS/58.
- MOORE, W. S., USSLER III, W., Paull, C. K. (2008): Short-lived radium isotopes in the Hawaiian margin: evidence for large fluid fluxes through the Puna Ridge, *Marine Chemistry* 109 (3–4), 421–430.
- NERI, G., CACCAMO, D., COCINA, O., MONTALTO, A. (1991): Shallow earthquake features in the Southern Tyrrhenian region: Geostructural and tectonic implications. *Bollettino di Geofisica Teorica ed Applicata*, XXXIII, 47–60.

- NERI, G., CACCAMO, D., COCINA, O., MONTALTO, A. (1996): Geodynamic implications of earthquake data in the Southern Tyrrhenian Sea, *Tectonophysics*, 258, 233–249.
- NISHIMURA, C., FORSYTH, D.W. (1989): The anisotropic structure of the upper mantle in the Pacific Ocean, *Geophysical Journal International*, 96, 203–229.
- NUCCIO, P.M., PAONITA, A., RIZZO, A., ROSCIGLIONE, A. (2008): Elemental and isotope covariation of noble gases in mineral phases from Etnean volcanics erupted during 2001–2005, and genetic relation with peripheral gas discharges. *Earth and Planetary Science Letters*, 272, 683–690.
- OZIMA, M., PODOSEK, F. A. (2002): Noble Gas Geochemistry. Cambridge University Press, New York, 286.
- PICHLER, H. (1989): Italienische Vulkangebiete V, Mte. Vulture, Äolische Inseln II (Salina, Filicudi, Alicudi, Panarea), Mit. Iblei, Capo Passero, Ustica, Pantelleria und Linosa. *Sammlung geologischer Führer* 83: Gebrüder Borntraeger, Berlin Stuttgart.
- PARSONS, B., SCLATER, J.G. (1977): An analysis of the variation of ocean floor bathymetry and heat flow with age. *Journal of Geophysical Research*, 82 (5), 803–827.
- PEPE, F., BERTOTTI, G., CELLA, F., MARSELLA, E. (2000): Rifted margins formation in the Southern Tyrrhenian Sea: A high-resolution seismic profile across the north Sicily continental margin. *Tectonics*, 19, 241–257.
- PETERS, M., STRAUSS, H., PETERSEN, S., KUMMER, N.-A., THOMAZO, C. (2011): Hydrothermalism in the Tyrrhenian Sea: Inorganic and microbial sulfur cycling as revealed by geochemical and multiple sulfur isotope data. *Chemical Geology*, 280, 217–231.
- PETERSON, S., MONECKE, T. (2009): FS METEOR, Cruise Report M73/2: Shallow drilling of hydrothermal sites in the Tyrrhenian Sea (PALINDRILL), Genoa – Heraklion 14.08.2007 – 30.08.2007, 30, 10-14 & 43.
- PICHLER, H. (1980): The island of Lipari. *Rendiconti della Societa Italiana di Mineralogia e Petrologia*, 36, 415–440.
- POLLACK, H.N., HURTER, S.J., JOHNSON, J.R. (1993): Heat flow from the Earth's interior: Analysis of the global data set. *Reviews of Geophysics*, 31(3), 267-280.
- PILZ, P. (2008): Ein neues magmatisch-tektonisches Modell zur Asthenosphärendynamik im Bereich der zentralandinen Subduktionszone Südamerikas. *Dissertation thesis*, University Potsdam.
- PRIBNOW, D. F. C., KINOSHITA, M., STEIN, C. A. (2000): Thermal Data Collection and Heat Flow Recalculations for Ocean Drilling Program Legs 101-180. Institut für Geowissenschaftliche Gemeinschaftsarbeiten (GGA), Project DFG Pr471/2, p. 9.

- RAYLEIGH, J.W.S. (1896): Theoretical considerations respecting the separation of gases by diffusion and similar processes. *Philosophical Magazine*, 42, 493.
- REES, C.E. (1973): A steady-state model for sulphur isotope fractionation in bacterial reduction processes. *Geochimica et Cosmochimica Acta*, 37, 1141–1162.
- REES, C.E., JENKINS, W.J., MONSTER, J. (1978): The sulphur isotopic composition of ocean water sulphate. *Geochimica et Cosmochimica Acta*, 42, 337–381.
- ROHLAND, K. (2007): Investigation in submarine water and gas chemistry at Panarea, Aeolian Islands, Italy. *Department for Geology (Section Hydrogeology)*, diploma thesis, TU Bergakademie Freiberg.
- RANALLI, G., (1987): Rheology of the Earth. Allen & Unwin Inc., 8 Winchester Place, Winchester, Mass 01890, USA.
- ROSSI, P. L., CALANCHI, N., GABBIANELLI, G., LANZAFAME, G. (1987): Nuovi dati strutturali su Salina e sull'area sottomarina circostante. *Bollettino del Gruppo Nazionale per la Vulcanologia (GNV)*, 599–611.
- ROUXEL, O., FOUQUET, Y., LUDDEN, J. N. (2004): Subsurface processes at the Lucky Strike hydrothermal field, Mid-Atlantic Ridge: Evidence from sulfur, selenium, and iron isotopes. *Geochimica Et Cosmochimica Acta*, 68, 2295-2311.
- SAKAI, H., DES MARAIS, D.J., UEDA, A., MOORE, J.G. (1984): Concentrations and isotope ratios of carbon, nitrogen and sulfur in ocean-floor basalts. *Geochimica et Cosmochimica Acta*, 48, 2433–2441.
- SANTO, A. P., CLARK, A. H. (1994): Volcanological evolution of Aeolian Arc (Italy): Inferences from $^{40}\text{Ar}/^{39}\text{Ar}$ ages of Filicudi rocks, paper presented at IAVCEI Congress. *International Association of Volcanology and Chemistry of the Earth's Interior*, Ankara.
- SIELAND, R. (2009): Chemical and isotopic investigations of submarine fluid discharges from Panarea, Aeolian Islands, Italy. *Department of Geology (Section Hydrogeology)*, diploma thesis, TU Bergakademie Freiberg, Vol. 21, FOG ISSN 1434-7512.
- SHEN, Y., FORSYTH, D.W. (1995): Geochemical constraints on initial and final depths of melting beneath mid-ocean ridges. *Journal of Geophysical Research*, 100, 2211–2238.
- SMITS, K. M., SAKAKI, T., LIMSUWAT, A., ILLANGASEKARE, T.H. (2010): Thermal Conductivity of Sands under Varying Moisture and Porosity in Drainage–Wetting Cycles. *Vadose Zone Journal*, 9 (1), 1-9.
- SOLOVIEV, S. L., KUZIN, I. P., KOVACEV, S. A., FERRI, M., GUERRA, I., LUONGA, G. (1990): Microearthquakes in the Tyrrhenian Sea as revealed by joint land and seabottom seismograph. *Marine Geology*, 94, 131–146.

- SPADINI, G., BERTOTTI, G., CLOETINGH, S. (1995): Tectono-stratigraphic modelling of the Sardinian margin of the Tyrrhenian Sea. *Tectonophysics*, 252, 269-284.
- STEIN, C.A. in: AHRENS, T.J. (Ed) (1995): Global Earth Physics – A Handbook of Physical Constants, AGU Reference Shelf 1. *American Geophysical Union*, Washington D.C., 144-158.
- STEIN, C.A., STEIN, S. (1992): A model for the global variation in oceanic depth and heat flow with lithospheric age. *Nature*, 359, 123–129.
- STEINBRÜCKNER, D. (2009): Quantification of submarine degassing of Panarea Volcano in the Aeolian archipelago, Italy. *Department of Geology (Section Hydrogeology)*, diploma thesis, TU Bergakademie Freiberg.
- SUNDBERG, J. (1988): Thermal Properties of Soils and Rocks. *Swedish Geotechnical Institute*, report no.35, Linköping, ISSN 0348-0755.
- TEAGLE, D.A.H., ALT, J.C., UMINO, S., MIYASHITA, S., BANERJEE, N.R., WILSON, D.S., and Expedition 309/312 Scientists (2006): Proc. IODP, 309/312: Washington DC, *Integrated Ocean Drilling Program Management International*, Inc.
- TIBALDI, A. (2001): Multiple sector collapses at Stromboli volcano, Italy: How they work. *Bulletin of Volcanology*, 63, 112–125.
- TINTI, S., MANUCCI, A., PAGNONI, G., ARMIGLIATO, A., ZANIBONI, R. (2005): The 30 December 2002 landslide-induced tsunamis in Stromboli: sequence of the events reconstructed from the eyewitness accounts, *Natural Hazards and Earth System Sciences*, 5, 763-775.
- TOMMASI, A., GODARD, M., COROMINA, G., DAUTRIA, J.M., BARSCZUS, H. (2004): Seismic anisotropy and compositionally induced velocity anomalies in the lithosphere above mantle plumes: a petrological and microstructural study of mantle xenoliths from French Polynesia. *Earth and Planetary Science Letters*, 227, 539–556.
- TORGERSEN, T. (1990): Crustal-scale fluid transport: magnitude and mechanisms, EOS Trans. *American Geophysical Union*, 71(1), 1 & 4 & 13.
- TRIELOFF, M., KUNZ, J., CLAGUE, D. A., HARRISON, D., ALLÈGRE, C. J. (2000): The nature of pristine noble gases in mantle plumes. *Science*, 291, 2269a.
- UEDA, A., SAKAI, H. (1984): Sulfur isotope study of Quaternary volcanic rocks from the Japanese island arc. *Geochimica et Cosmochimica Acta*, 48, 1837–1848.
- URBANIK, S. (2011): Influence on thermal conductivity from porous materials based on different moisture contents, *Seminal paper (unpublished)*, Institute of Thermal Engineering and Thermodynamics (IWTT), Technical University Bergakademie Freiberg

- VIETH, A. (2003): Anwendung stabiler Isotope zur Beschreibung des mikrobiellen Abbaus organischer Schadstoffe in kontaminierten Aquiferen. *Dissertation thesis*, Christian-Albrechts-University Kiel.
- VENTURA, G. (1995): Relationships between tectonics and volcanism in the central and eastern sectors of the Aeolian Islands, in Proceedings of the National Congress, 957–965, *Gruppo Nazionale di Geofisica Terra Solida - Consiglio Nazionale delle Ricerche*, Rome.
- VENTURA, G., VILARDO, G. (1999): Seismic-based estimate of hydraulic parameters at Vesuvius volcano. *Geophysical Research Letters*, 26, 887–890.
- VILLINGER, H., EARL E. DAVIS, E. E. (1987): A New Reduction Algorithm for Marine Heat Flow Measurements. *Journal of Geophysical Research*, 92 (B12), 12846-12856.
- VITORELLO, I., POLLACK, H. (1980): On the variation of continental heat flow with age and the thermal evolution of continents. *Journal of Geophysical Research*, 85, 983–995.
- VOLPI, V., DEL BEN, A., MARTINI, F., FINETTI, I. (1997): Elaborazione ed Interpretazione della Linea CROP-MARE 2A5 nel Bacino di Gioia (Tirreno Sud-Orientale), paper presented at 16th National Congress. *Gruppo Nazionale di Geofisica Terra Solida - Consiglio Nazionale delle Ricerche*, Rome.
- WELHAN, J.A. (1987): Characteristics of abiogenic methane in rocks. In: P Fritz and S.K Frapce (Eds): *Saline Water and Gases in Crystallized Rocks*. Geological Association Canada Special Paper 33, 225–233.
- WIENS, D.A., KELLEY, K.A., PLANK, T. (2006): Mantle temperature variations beneath back-arc spreading centers inferred from seismology, petrology, and bathymetry. *Earth and Planetary Science Letters*, 248, 30–42.
- WHITICAR, M.J. (1999): Carbon and hydrogen isotope systematics of bacterial formation and oxidation of methane. *Chemical Geology*, 161 (1-3), 291-314.
- WULF, R. (2009): Wärmeleitfähigkeit von hitzebeständigen und feuerfesten Dämmstoffen - Untersuchungen zu Ursachen für unterschiedliche Messergebnisse bei Verwendung verschiedener Messverfahren, *Dissertation thesis*, Technical University Bergakademie Freiberg.
- YANG, K., SCOTT, S. D. (2006): Magmatic Fluids as a Source of Metals in Seafloor Hydrothermal Systems: evidence from melt inclusions and vesicles: in, D.M. Christie, C.R. Fisher and S-M Lee, editors, Back Arc Spreading Systems: Geological, Biological, Chemical and Physical Interactions: *American Geophysical Union, Geophysical Monograph*, 166, 163-184.

Standards and Codes

VDI-Wärmeatlas Code 4640- sheet 2 (2001): Thermische Nutzung des Untergrundes, Erdgekoppelte Wärmepumpenanlagen, VDI-Verlag Düsseldorf.

DIN EN 993-14: Prüfverfahren für dichte geformte feuerfeste Erzeugnisse - Teil 14: Bestimmung der Wärmeleitfähigkeit nach dem Heißdraht-(Kreuz-)Verfahren; Deutsche Fassung EN 993-14:1998.

APPENDIX

Appendix A – Tables

Table A 1:	Average abundance of elements in standard seawater after Brown et al. (1995).	117
Table A 2:	Coordinates of the locations in different notations. Translation of the origin geographical coordinates with the program MapSource, version 2.02. Verification was made with a corresponding tool in Google Earth. (DegDec – decimal degree; DMS – degrees, minutes, seconds)	118
Table A 3:	Injected amounts of gas sample for helium and neon isotope analyses	118
Table A 4:	Selection of different coordinate and reference systems which are common in Italy.	119
Table A 5:	Results of the on-site parameters determined during the excursion in September 2010. With the help of the measured Eh values were calculated the corrected amount based on a temperature of 25 °C and related to the standard hydrogen potential. rH is a pH independent indicator for the redox power of a system (Section 3.3). The species (S^{2-} , NO_2^- , NH_4^+) are corrected with equations shown in Table A13.	120
Table A 6:	Correction equation for the measured photometric values of nitrite, ammonia, and sulphide. These values are based on calculation from Rohland (2007).	121
Table A 7:	List of gas samples analysed at the INGV in Palermo in September 2010. It shows the date of sampling as well as the type and amount of available gas sampling tubes (GST) with septum (from TUBAF) and without a septum (from INGV)	121
Table A 8:	Water and gas samples from 2009 and 2010 which were analysed at the UFZ in April 2011.	122
Table A 9:	Results from laboratory measurements in April 2011 at the UFZ. It was analyzed water, solid samples made of water and gas as well as bio probes. All samples were collected during the excursion to Panarea in 2009 and 2010.	124
Table A 10:	All data from the $\delta^{18}O$ -measurments of both laboratories (UFZ and INGV) made in 2010. Data from the UFZ are already corrected after the reference waters (MAST and PES).	126
Table A 11:	Summarized ANOVA results of the measured $\delta^{18}O$ -values in both laboratories. The amount for F_{crit} is looked up in the Fisher table respectively F-distribution, for $\alpha = 0.05$.	127
Table A 12:	All data from the δ^2H -measurments of both laboratories (UFZ and INGV) made in 2010. Data from the UFZ are already corrected after the reference waters (MAST and PES).	128
Table A 13:	Summarized ANOVA results of the measured δ^2H -values in both laboratories. The amount for F_{crit} is looked up in the Fisher table respectively F-distribution, for $\alpha = 0.05$.	129
Table A 14:	All water samples from 2008, 2009 and 2010 which were measured at the INGV and UFZ for $\delta^{13}C_{DIC}$.	130
Table A 15:	(D/O)-measurements at the INGV and UFZ arranged between 2007 and 2011.	131
Table A 16:	Calculated 3-componenten-mixture-system for measured (O/D)-values at the UFZ including Mediterranean water, magmatic water and local meteoric water. Results are arranged in diving spots.	133

Table A 17: Calculated 3-componenten-mixture-system for measured (O/D)-values at the INGV including Mediterranean water, magmatic water and local meteoric water. Results are arranged in diving spots.	134
Table A 18: Results of the $\delta^{34}\text{S}$ determination of water (highlighted blue), gas (highlighted yellow) and bio samples (highlighted brown) measured at the UFZ in 2011.	135
Table A 19: Results of the $\delta^{34}\text{S}$ determination of water (highlighted blue) and gas (highlighted yellow) Samples from 2006 and 2007, measured at the UFZ.....	136

Appendix B – Figures

- Figure B 1: Map showing the known heat flows in the Mediterranean, Black and Red Seas published from the International Heat Flow Commission (IHFC), University of North Dakota. Data are presented in a colour coded format using the visible light spectrum so that warm colours (reds) indicate high heat flow and cool colours (violet) indicate low heat flow. The spectral range for each data map is 0 to 200 mW/m² in intervals of 10 mW/m². Heat flow greater than 200 mW/m² are assigned the warmest colour..... 137
- Figure B 2: Thermal conductivity in quartz sand for different porosities and different water contents (research after Krischer, 1934). 138
- Figure B 3: Separately illustration of the anions Br⁻, Cl⁻, SO₄²⁻ and F⁻ for each diving location. The calculated mean values and corresponding standard diversity are displayed. The content of normal seawater after Brown et al. (1995) are shown for a better comparison..... 139
- Figure B 4: Separately illustration of the cations Mn²⁺, Ca²⁺, Mg²⁺, K⁺ for each diving location. The calculated mean values and corresponding standard diversity are displayed. The content of normal seawater after Brown et al. (1995) are shown for a better comparison..... 140

Table A 1: Average abundance of elements in standard seawater after Brown et al. (1995).

element	concentration [mg/l]	molar mass [g/mol]	concentration [mmol/l]	element	concentration [mg/l]	molar mass [g/mol]	concentration [mmol/l]
Ag	2.00E-06	107.87	1.85E-08	N	11.5	14.007	0.82
Al	4.00E-04	26.98	1.48E-05	Na	1.08E+04	22.99	468.46
Ar	0.43	39.95	1.08E-02	Nb	1.00E-05	92.91	1.08E-07
As	2.00E-03	74.92	2.67E-05	Nd	3.00E-06	144.24	2.08E-08
Au	2.00E-08	196.97	1.02E-10	Ne	1.20E-04	20.18	5.95E-06
B	4.4	10.81	4.07E-01	Ni	4.80E-04	58.7	8.18E-06
Ba	2.00E-02	137.33	1.46E-04	O	6	15.999	3.75E-01
Be	2.00E-07	9.01	2.22E-08	P	6.00E-02	30.97	1.94E-03
Bi	2.00E-08	208.98	9.57E-11	Pa	5.00E-11	231.04	2.16E-13
Br	67	79.9	0.84	Pb	2.00E-06	207.2	9.65E-09
C	28	12.01	2.33	Pd	5.00E-08	106.4	4.70E-10
Ca	4.12E+02	40.08	10.28	Po	5.00E-16	209	2.39E-18
Cd	1.00E-04	112.41	8.90E-07	Pr	6.00E-07	140.91	4.26E-09
Ce	2.00E-06	140.12	1.43E-08	Ra	7.00E-11	226	3.10E-13
Cl	1.95E+04	35.45	550.07	Rb	0.12	85.47	1.40E-03
Co	3.00E-06	58.93	5.09E-08	Re	4.00E-06	186.21	2.15E-08
Cr	3.00E-04	51.996	5.77E-06	Rn	6.00E-16	222	2.70E-18
Cs	4.00E-04	132.91	3.01E-06	S	9.05E+02	32.06	28.23
Cu	1.00E-04	63.55	1.57E-06	Sb	2.00E-04	121.75	1.64E-06
Dy	9.00E-07	162.5	5.54E-09	Sc	6.00E-07	44.96	1.33E-08
Er	8.00E-07	167.26	4.78E-09	Se	2.00E-04	78.96	2.53E-06
Eu	2.00E-07	151.96	1.32E-09	Si	2	28.09	7.12E-02
F	1.3	18.998	6.84E-02	Sm	6.00E-07	150.35	3.99E-09
Fe	5.50E-05	55.85	9.85E-07	Sn	6.00E-07	118.69	5.06E-09
Ga	2.00E-06	69.72	2.87E-08	Sr	8	87.62	9.13E-02
Gd	7.00E-07	157.25	4.45E-09	Ta	2.00E-06	180.95	1.11E-08
Ge	5.00E-06	72.59	6.89E-08	Tb	1.00E-07	158.92	6.29E-10
He	6.80E-06	1.008	6.75E-06	Te	1.00E-08	127.6	7.84E-11
Hf	7.00E-05	178.49	3.92E-07	Th	1.00E-05	232.04	4.31E-08
Hg	1.00E-06	200.59	4.99E-09	Ti	1.00E-03	47.9	2.09E-05
Ho	3.00E-07	164.93	1.82E-09	Tl	1.00E-05	204.37	4.89E-08
I	6.00E-02	126.9	4.73E-04	Tm	2.00E-07	168.93	1.18E-09
In	2.00E-07	114.82	1.74E-09	U	3.20E-03	238.03	1.34E-05
K	3.80E+02	39.1	9.72	V	2.00E-03	50.94	3.93E-05
Kr	2.00E-04	83.8	2.39E-06	W	1.00E-04	183.85	5.44E-07
La	3.00E-06	138.91	2.16E-08	Xe	5.00E-05	131.3	3.81E-07
Li	0.18	6.94	2.59E-02	Y	1.00E-06	88.91	1.12E-08
Lu	2.00E-07	174.97	1.14E-09	Yb	8.00E-07	173.04	4.62E-09
Mg	1.29E+03	24.31	53.06	Zn	5.00E-04	65.38	7.65E-06
Mn	3.00E-05	54.94	5.46E-07	Zr	3.00E-05	91.22	3.29E-07
Mo	1.00E-02	95.94	1.04E-04				

Table A 2: Coordinates of the locations in different notations. Translation of the origin geographical coordinates with the program MapSource, version 2.02. Verification was made with a corresponding tool in Google Earth. (DegDec – decimal degree; DMS – degrees, minutes, seconds)

Location	UTM WGS 84 Zone 33S		Geographical coordinates			
	Easting [m]	Northing [m]	DegDec in [x°]		DMS in [x°x'x.x"]	
			Easting [°]	Northing [°]	Easting	Northing
Bottaro West*	509525.190	4276525.677	15.10944	38.63722	38°38'14.4"	15°06'34.1"
Bottaro North*	509573.357	4276679.852	15.11000	38.63861	38°38'19.2"	15°06'36.4"
Point 21*	509283.292	4276648.686	15.10667	38.63833	38°38'18.1"	15°06'24.4"
Hot Lake*	509548.998	4276833.940	15.10972	38.64000	38°38'24.5"	15°06'35.0"
Fumaroles Field*	509573.173	4276833.969	15.11000	38.64000	38°38'24.1"	15°06'35.8"
BlackPoint*	509114.100	4276617.668	15.10472	38.63806	38°38'16.7"	15°06'17.1"
Area 26**	509162.309	4276741.017	15.10528	38.63917	38°38'21.2"	15°06'18.5"
Mole***	506803.236	4276605.871	15.07817	38.63797		
Leuchtfeuer***	506799.011	4276457.176	15.07812	38.63663		
Hotel***	506660.360	4276778.855	15.07653	38.63953		
Area 26***	509152.063	4276736.936	15.10516	38.63913		
Point 21***	509248.736	4276677.127	15.10627	38.63859		
La Calcara***	506714.612	4277464.660	15.07716	38.64571		
Black Point***	509129.663	4276538.285	15.10490	38.63734		
Secca de Lisca Nera***	509556.550	4276179.259	15.10980	38.63410		
Mini Hot Lake***	509132.936	4276720.270	15.10494	38.63898		
Spot 2***	509180.843	4276684.816	15.10549	38.63866		
Spot 3***	509186.036	4276710.344	15.10555	38.63889		
Spot 4***	509160.679	4276813.512	15.10526	38.63982		
Mini Black Point***	509155.512	4276765.791	15.10520	38.63939		

* modified from (Rohland, 2007)

** modified from (WISTAU, 2008)

*** modified from (WISTAU,2010)

Table A 3: Injected amounts of gas sample for helium and neon isotope analyses.

Sampling location	Injected amount in [mbar]
BP	95
La Calcara	133
P21	100
Area 26	100
BN	100
FumF	400

Table A 4: Selection of different coordinate and reference systems which are common in Italy.

Coordinate systems	Reference systems
Italian Gauss-Boaga Zone West coordinates	ETRS89 (Europa), geocentric, GRS80
Italian Gauss-Boaga Zone Ost coordinates	ROMA40 (IT), Monte Mario, Hayford/Int.
UTM coordinates (northern hemisphere)	ROMA40 (IT peninsula < ± 4 m), M. Mario, Hayford/Int.
Geographic coordinates (Roma) [degree, min, sec]	ROMA40 (IT Sardinia < ± 4 m), M. Mario, Hayford/Int.
Geographic coordinates (Roma) [degree]	ROMA40 (IT Sicily < ± 4 m), M. Mario, Hayford/Int.
Geographic coordinates (Greenwich) [degree, min, sec]	ED50 (Europe), Potsdam, Hayford/Int.
	ED50 (IT, Sardinia), Potsdam, Hayford/Int.
	ED50 (IT, Sicily), Potsdam, Hayford/Int.
	WGS84 (worldwide GPS), geocentric, WGS84
	WGS72 (worldwide), geocentric, WGS72

Table A 5: Results of the on-site parameters determined during the excursion in September 2010. With the help of the measured Eh values were calculated the corrected amount based on a temperature of 25 °C and related to the standard hydrogen potential. r_H is a pH independent indicator for the redox power of a system (Section 3.3). The species (S²⁻, NO₂⁻, NH₄⁺) are corrected with equations shown in Table A13.

Location	Date of sampling	subdivision	pH	EC [mS/cm]	E _h [mV]	E _h corrected [mV]	r _H	O ₂ [mg/l]	T [°C]	S ²⁻ _{corr} [mg/l]	NO ₂ ⁻ _{corr} [mg/l]	NH ₄ ⁺ _{corr} [mg/l]
Calcara (CM)	02.09.10		4.60	61.4	0	-1	9.20	4.70	28.1			11.2
BN (CM)	07.09.10		5.30	55.3	-236	-237	8.31	7.00	26.7			1.4
P21 (CM)	07.09.10		4.80	54.3	-209	-210	7.57	6.30	26.8			1.3
Fum F (CM)	04.09.10		4.60	70.9	-223	-223	7.04	5.60	27.9			14.8
BP (CM)	05.09.10		5.00	55.0	-155	-155	8.50	7.80	26.8			3.3
Area26 (CM)	06.09.10		4.50	55.4	-245	-246	6.63	5.40	28.0			3.7
La Calcara (MS)	02.09.10		4.85	58.7	-19	-19	9.51	1.54	26.9			
P21 (MS)	02.09.10	I	4.67	55.2	-249	-249	6.93	0.39	26.4	30.21	0.021	0.5
		II	4.84	53.5	-250	-250	7.26	1.56	25.9	overrange		
		CO2 Sensor	6.85			0	13.70	7.84	25.3	0.09	0.027	0.0
HL (MS)	04.09.10	3 m Lanze	4.50	98.4	-261	-261	6.47	0.62	29.1	59.37	0.051	26.9
P21 (MS)	05.09.10		4.83	54.1	-250	-250	7.24	1.47	28.1	38.54	0.005	4.6
BP (MS)	05.09.10		2.40	75.8	42	42	5.20	4.96	26.8	0.14	0.048	26.9
Area26 (MS)	06.09.10	I	4.91	56.2	-243	-244	7.46	1.82	28.0	0.15	0.013	6.1
		II (N)	4.65	55.8	-230	-231	7.06	0.83	30.9	0.18	0.009	5.1
BW (MS)	06.09.10		5.01	56.9	-209	-209	8.00	4.10	25.1	24.48	0.016	5.6
Area26 (MS)	07.09.10	(N)	4.74	55.8	-261	-261	6.96	0.59	27.5	0.15	0.032	2.6
BN (MS)	07.09.10		5.30	57.1	-272	-272	7.97	2.54	26.7	0.11	0.021	4.6
HL (MS)	08.09.10	3 m Lanze	4.44	97.5	-252	-252	6.44	1.70	27.9	25.00	0.021	32.5
		Fum F	4.74	68.8	-249	-249	7.07	4.13	27.4	0.12	0.032	14.7

Table A 6: Correction equation for the measured photometric values of nitrite, ammonia, and sulphide. These values are based on calculation from Rohland (2007).

Species	Correction equation	R ²
NO ₂ ⁻	y = 1.1468 x + 0.0037	0.9989
NH ₄ ⁺	y = 1.0148 x + 0.0204	0.9778
S ²⁻	y = 1.0415 x + 0.0079	0.9993

Table A 7: List of gas samples analysed at the INGV in Palermo in September 2010. It shows the date of sampling as well as the type and amount of available gas sampling tubes (GST) with septum (from TUBAF) and without a septum (from INGV).

Location	Date	type of GST (INGV/TUBAF)	GC	He/Ne	Ar	δ ¹³ C _{CH4}	δC _{CO2}
Area 26**	06.09.2010	2 vs. 0	x			x	x
BN**	07.09.2010	0 vs. 2	x	x	x	x	x
La Calcara***	02.09.2010	2 vs. 1	x	x	x	x	x
P21**	07.09.2010	1 vs. 1	x	x	x	x	x
BP***	05.09.2010	2 vs. 1	x	x	x	x	x
FumF***	04.09.2010	2 vs. 0	x	x	x	x	x

Table A 8: Water and gas samples from 2009 and 2010 which were analysed at the UFZ in April 2011.

	No.	Proben-ID	Proben.ID UFZ	date	location	LF [mS/cm]	pH	S2- [mg/L]	H, O, C- Isotope	ZnS from S2-	BaSO4 from SO4	ZnS from H2S	BaCO3 from CO2
Water 2009	1	PAN-BP-030909		03/09/2009	BP	56.7	2.46	0.19	X				
	2	PAN-P21-050909		05/09/2009	P21	51.6	5.03	15.50	X				
	3	PAN-BP-050909	714-ILH-47-10	05/09/2009	BP	68.8	2.43	-	X	X	X		
	4	PAN-HL-060909	715-ILH-47-10	06/09/2009	HL	83.4	5.07	0.08	X	X	X		
	5	PAN-BP2-060909	716-ILH-47-10	06/09/2009	BP2	47.5	5.01	5.00	X	X	X		
	6	PAN-B(N)-090909	717-ILH-47-10	09/09/2009	BN	52.4	5.50	0.07	X	X	X		
	7	PAN-Fum-100909	718-ILH-47-10	10/09/2009	FumF	61.6	4.86	0.04	X	X	X		
	8	PAN-Area26-100909		10/09/2009	Area 26	48.8	5.23	-	X				
	9	PAN-HL-110909(3m)		11/09/2009	HL	95.5	5.31	0.11	X				
	10	PAN-HL-120909(3m)	719-ILH-47-10	12/09/2009	HL	94.0	4.67	17.50	X	X	X		
Water 2010	11	PAN-P21-020910	720-ILH-47-10	02/09/2010	P21	55.2	4.67	29.00	X	X	X		
	12	PAN-P21-020910(II)		02/09/2010	P21	53.5	4.84	overrange	X				
	13	PAN-LaCalcara-020910		02/09/2010	LaCalcara	58.7	4.85	-	X				
	14	PAN-HL-040910(3m)	721-ILH-47-10	04/09/2010	HL	98.4	4.50	57.00	X	X	X		
	15	PAN-P21-050910	722-ILH-47-10	05/09/2010	P21	54.1	4.83	37.00	X	X	X		
	16	PAN-BP-050910	723-ILH-47-10	05/09/2010	BP	75.8	2.40	0.13	X	X	X		
	17	PAN-BP-050910(II)		05/09/2010	BP	-	-	-	X				
	18	PAN-Area26-060910		06/09/2010	Area 26 (I)	56.2	4.91	0.14	X				
	19	PAN-Area26-060910	724-ILH-47-10	06/09/2010	Area 26 (II)	55.8	4.65	0.17	X	X	X		
	20	PAN-B(W)-060910	725-ILH-47-10	06/09/2010	BW	56.9	5.01	23.50	X	X	X		
	21	PAN-Area26N-070910	726-ILH-47-10	07/09/2010	Area 26 N	55.8	4.74	0.14	X	X	X		
	22	PAN-B(N)-070910	727-ILH-47-10	07/09/2010	BN	57.1	5.30	0.10	X	X	X		
	23	PAN-HL(FUM)-080910	728-ILH-47-10	08/09/2010	FumF	68.8	4.74	0.11	X	X	X		
	24	PAN-HL-080910(3m)	729-ILH-47-10	08/09/2010	HL	97.5	4.44	24.00	X	X	X		
	25	PAN-LaCalcara-120910	730-ILH-47-10	12/09/2010	LaCalcara	-	-	-	X	X	X		
	26	PAN-FumF-040910CM		04/09/2010	FumF	70.9	4.60	-	X				
	27	PAN-BP-050910CM		05/09/2010	BP	55000.0	5.00	-	X				
	28	PAN-Area26-060910CM		06/09/2010	Area 26	55400.0	4.50	-	X				
	29	PAN-P21-070910CM		07/09/2010	P21	54.3	4.80	-	X				
	30	PAN-BN-070910CM		07/09/2010	BN	55.3	5.30	-	X				

Table A 8: Water and gas samples from 2009 and 2010 which were analysed at the UFZ in April 2011 (continuation).

Gas 2009	31	PAN-P21-030909	731-ILH-47-10	03/09/2009	P21	X	X
	32	PAN-P21-050909	732-ILH-47-10	05/09/2009	P21	X	X
	33	PAN-BP-060909	733-ILH-47-10	06/09/2009	BP	X	X
	34	PAN-B(N)-090909	734-ILH-47-10	09/09/2009	BN	X	X
	35	PAN-Fum-100909	735-ILH-47-10	10/09/2009	FumF	X	X
	36	PAN-Area26-120909	736-ILH-47-10	12/09/2009	Area 26	X	X
Gas 2010	37	PAN-Area26-14092010	737-ILH-47-10	04/09/2010	Area 26	X	
	38	PAN-B(N)-07092010	738-ILH-47-10	07/09/2010	BN	X	
	39	PAN-B(W)-060910	739-ILH-47-10	06/09/2010	BW	X	
	40	PAN-BP-050910	740-ILH-47-10	05/09/2010	BP	X	
	41	PAN-P21-050910	741-ILH-47-10	05/09/2010	P21	X	
	42	PAN-HL(FUM)-080910	742-ILH-47-10	08/09/2010	FumF	X	
	43	PAN-LaCalcara-120910	743-ILH-47-10	12/09/2010	La Calcara	X	
Others	44	elemental sulfur	744-ILH-47-10	10/09/2010	Area 26		
	45	PAN-P21-08092010_BIO	745-ILH-47-10	08/09/2010	P21		
	46	PAN-P21-08092010_BIO2	746-ILH-47-10	09/09/2010	P21		

Table A 9: Results from laboratory measurements in April 2011 at the UFZ. It was analyzed water, solid samples made of water and gas as well as bio probes. All samples were collected during the excursion to Panarea in 2009 and 2010.

Sample code (local)	Sampling date	$\delta^{18}\text{O}$ [‰ _{VSMOW}]	$\delta^2\text{H}$ [‰ _{VSMOW}]	$\delta^{34}\text{S}_{\text{elemental}}$ [‰ _{VCDT}]	$\delta^{34}\text{S}_{\text{sulphide}}$ [‰ _{VCDT}]	$\delta^{34}\text{S}_{\text{sulphate}}$ [‰ _{VCDT}]	$\delta^{18}\text{O}_{\text{sulphate}}$ [‰ _{VSMOW}]	$\delta^{13}\text{C}_{\text{DIC}}$ [‰ _{VPDB}]	Remarks	sulphur species	d excess [‰ _{VSMOW}]
PAN-Area26-060910	06/09/2010	0.93	7.8		-0.3	21.1	10.5	15.8	Solid from water	AVS	-62.4
PAN-Area26-060910	06/09/2010	1.06	7.3					9.1	Water		-58.3
PAN-Area26-060910CM	06/09/2010	1.40	8.0					-12.1	Water		-64.4
PAN-Area26-100909	10/09/2009	0.91	7.7					-5.8	Water		-61.4
PAN-Area26-120909	12/09/2009				1.8	no sample	no sample	-4.2	Solid from gas	AVS	
PAN-Area26-14092010	04/09/2010				-1.1	no sample	no sample		Solid from gas	AVS	
PAN-Area26N-070910	07/09/2010	0.86	7.1		-2.4	23.0	12.2	16.0	Solid from water	AVS	-56.6
PAN-B(N)-070910	07/09/2010	0.88	6.4		-0.7	22.5	11.1	17.5	Solid from water	AVS	-51.1
PAN-B(N)-07092010	07/09/2010				0.5	no sample	no sample		Solid from gas	AVS	
PAN-BN-070910CM	07/09/2010	1.18	8.2					19.5	Water		-65.5
PAN-B(N)-090909	09/09/2009	0.86	6.7		0.6	22.5	11.1	19.4	Solid from water	AVS	-53.5
PAN-B(N)-090909	09/09/2009				4.8	no sample	no sample	-2.2	Solid from gas	AVS	
PAN-B(W)-060910	06/09/2010	0.98	8.4		3.0	22.2	8.5	13.6	Solid from water	AVS	-67.4
PAN-B(W)-060910	06/09/2010				2.3	no sample	no sample		Solid from gas	AVS	
PAN-BP-030909	03/09/2009	2.16	3.6					-7.3	Water		-29.0
PAN-BP-050909	05/09/2009	2.32	4.1		2.6	21.2	7.9	-6.8	Solid from water	AVS	-33.0
PAN-BP-050910	05/09/2010	2.62	4.1		-	22.8	10.5	-8.4	Solid from water	AVS	-32.8
PAN-BP-050910(II)	05/09/2010	2.61	4.4					-6.7	Water		-35.0
PAN-BP-050910CM	05/09/2010	1.67	9.2					9.0	Water		-73.5
PAN-BP-050910	05/09/2010				3.7	no sample	no sample		Solid from gas	AVS	
PAN-BP-060909	06/09/2009				4.3	no sample	no sample	-5.8	Solid from gas	AVS	
PAN-BP2-060909	06/09/2009	0.95	7.8		3.6	21.2	9.7	15.0	Solid from water	AVS	-62.6
PAN-Fum-100909	10/09/2009	0.39	3.1		1.2	22.7	9.6	-5.6	Solid from water	AVS	-25.0
PAN-Fum-100909	10/09/2009				1.5	no sample	no sample	-3.3	Solid from gas	AVS	
PAN-FumF-040910CM	04/09/2010	0.48	1.8					-5.9	Water		-14.1
PAN-HL(FUM)-080910	08/09/2010	0.46	2.4		1.5	21.9	9.2	15.1	Solid from water	AVS	-19.5
PAN-HL(FUM)-080910	08/09/2010				1.8	no sample	no sample		Solid from gas	AVS	
PAN-HL-040910(3m)	04/09/2010	0.94	-5.4		1.8	21.1	10.4	6.6	Solid from water	AVS	43.2
PAN-HL-060909	06/09/2009	0.87	-3.4		2.3	20.7	9.6	-5.7	Solid from water	AVS	27.5
PAN-HL-080910(3m)	08/09/2010	1.04	-5.3		2.0	22.2	10.5	22.5	Solid from water	AVS	42.7

Table A 9: Results from laboratory measurements in April 2011 at the UFZ. It was analyzed water, solid samples made of water and gas as well as bio probes. All samples were collected during the excursion to Panarea in 2009 and 2010 (continuation).

PAN-HL-110909(3m)	11/09/2009	0.85	-7.2					-8,6 ± 1,4	Water		57.2
PAN-HL-120909(3m)	12/09/2009	0.88	-7.6		3.1	22.4	11.1	-7,5 ± 2,8	Solid from water	AVS	60.4
PAN-LaCalcara-020910	02/09/2010	3.02	8.9					13.0	Water		-71.3
PAN-LaCalcara-120910	12/09/2010	2.80	9.4		-	20.1	8.7	17.1	Solid from water	AVS	-75.1
PAN-LaCalcara-120910	12/09/2010				0.7	no sample	no sample		Solid from gas	AVS	
PAN-P21-020910	02/09/2010	1.19	7.5		-0.4	21.0	8.5	17.6	Solid from water	AVS	-59.9
PAN-P21-020910(II)	02/09/2010	1.06	6.8					17.4	Water		-54.1
PAN-P21-030909	03/09/2009				1.5	no sample	no sample	-3.3	Solid from gas	AVS	
PAN-P21-050909	05/09/2009				-1.0	no sample	no sample	-2.5	Solid from gas	AVS	
PAN-P21-050909	05/09/2009	1.29	8.4					14.9	Water		-66.8
PAN-P21-050910	05/09/2010	1.19	7.8		-0.8	21.7	11.1	-5.1	Solid from water	AVS	-62.2
PAN-P21-050910	05/09/2010				-0.5	no sample	no sample		Solid from gas	AVS	
PAN-P21-070910CM	07/09/2010	1.39	8.6					11.4	Water		-69.1
PAN-P21-08092010_BIO	08/09/2010				-1.1	-3.6	-	-	Solid-bio sample	CRS	
PAN-P21-08092010_BIO2	09/09/2010				-0.9	-2.4	-	-	Solid-bio sample	CRS	
elemental Sulfur	10/09/2010				-4.1	-3.3			Solid-bio sample	CRS	

Table A 10: All data from the $\delta^{18}\text{O}$ -measurements of both laboratories (UFZ and INGV) made in 2010. Data from the UFZ are already corrected after the reference waters (MAST and PES).

sample ID	UFZ $\delta^{18}\text{O}_{\text{VSMOW}}$ [‰]	Average / Variance	INGV $\delta^{18}\text{O}_{\text{VSMOW}}$ [‰]	Average / Variance
PAN-LaCalcara-020910	3.010	3.02 / 0.001	2.50	2.63 / 0.017
	3.051		2.63	
	2.988		2.76	
PAN-P21-050910	1.170	1.19 / 0.000	0.79	0.65 / 0.018
	1.204		0.52	
	1.196		0.64	
PAN-BP-050910MS	2.591	2.61 / 0.001	1.46	1.42 / 0.003
	2.649		1.38	
	2.598			
PAN-Area26N-070910	0.820	0.86 / 0.005	0.69	0.73 / 0.017
	0.943		0.63	
	0.824		0.88	
PAN-HL-080910(3m)	1.029	1.04 / 0.000	-0.30	-0.42 / 0.029
	1.047		-0.54	
	1.047			
PAN-LaCalcara-120910 MS	2.695	2.80 / 0.008	3.06	3.06 / 0.002
	2.873		3.10	
	2.822		3.02	
PAN-FumF-040910CM	0.530	0.47 / 0.006	-0.10	-0.093 / 0.001
			-0.06	
	0.420		-0.12	
PAN-BP-050910CM	1.665	1.66 / 0.000	1.05	1.01 / 0.003
	1.652		0.97	
	1.651			
PAN-Area26-060910CM	1.342	1.34 / 0.002	0.38	0.41 / 0.001
	1.385		0.45	
	1.300		0.41	
PAN-P21-070910CM	1.376	1.38 / 0.000	0.71	0.575 / 0.036
	1.405		0.44	
	1.372			
PAN-BN-070910CM	1.273	1.179 / 0.007	0.89	0.997 / 0.017
	1.136		0.96	
	1.129		1.14	

Table A 11: Summarized ANOVA results of the measured $\delta^{18}\text{O}$ -values in both laboratories. The amount for F_{crit} is looked up in the Fisher table respectively F-distribution, for $\alpha = 0.05$.

Location	Source of Variation	Degree of freedom	Variances	F	F_{crit}
La Calcara (1)	S_{Lab}^2	1	0.224	25.01	7.71
	S_{R}^2	4	0.056		
P21 (1)	S_{Lab}^2	1	0.438	47.00	7.71
	S_{R}^2	4	0.009		
BP (MS)	S_{Lab}^2	1	1.708	986.87	10.13
	S_{R}^2	3	0.002		
Area26N	S_{Lab}^2	1	0.025	2.29	7.71
	S_{R}^2	4	0.011		
HL	S_{Lab}^2	1	2.560	264.78	10.13
	S_{R}^2	3	0.010		
La Calcara (2)	S_{Lab}^2	1	0.104	20.80	7.71
	S_{R}^2	4	0.005		
FumF	S_{Lab}^2	1	0.387	147.47	10.13
	S_{R}^2	3	0.003		
BP	S_{Lab}^2	1	0.500	450.24	10.13
	S_{R}^2	3	0.001		
Area26	S_{Lab}^2	1	1.295	850.02	7.71
	S_{R}^2	4	0.002		
P21 (2)	S_{Lab}^2	1	0.786	63.56	10.13
	S_{R}^2	4	0.012		
BN	S_{Lab}^2	1	0.050	4.30	7.71
	S_{R}^2	4	0.012		

* S_{Lab}^2 = Between the laboratories
 S_{R}^2 = Within the laboratories

Table A 12: All data from the $\delta^2\text{H}$ -measurements of both laboratories (UFZ and INGV) made in 2010. Data from the UFZ are already corrected after the reference waters (MAST and PES).

sample ID	UFZ $\delta^{18}\text{O}_{\text{VSMOW}}$ [‰]	Average / Variance	INGV $\delta^{18}\text{O}_{\text{VSMOW}}$ [‰]	Average / Variance
PAN-LaCalcara-020910	8.629	8.91 / 0.090	0	0 / -
	8.873			
	9.225			
PAN-P21-050910	7.649	7.78 / 0.016	-2	-2 / -
	7.773			
	7.904			
PAN-BP-050910MS	4.299	4.11 / 0.030	-7	-7 / -
	3.961			
	4.058			
PAN-Area26N-070910	6.887	7.07 / 0.068	-3	-3 / -
	6.961			
	7.373			
PAN-HL-080910(3m)	-5.162	-5.34 / 0.025	-14	-14 / -
	-5.386			
	-5.467			
PAN-LaCalcara-120910 MS	9.507	9.39 / 0.017	0	0 / -
	9.406			
	9.251			
PAN-FumF-040910CM	1.954	1.76 / 0.074	-8	-8 / -
	1.568			
PAN-BP-050910CM	9.192	9.19 / 0.021	-3	-3 / -
	9.330			
	9.040			
PAN-Area26-060910CM	8.132	8.05 / 0.014	-7	-7 / -
	7.911			
	8.094			
PAN-P21-070910CM	8.593	8.64 / 0.003	-2	-2 / -
	8.703			
	8.612			
PAN-BN-070910CM	8.043	8.19 / 0.032	-2	-2 / -
	8.390			
	8.136			

Table A 13: Summarized ANOVA results of the measured $\delta^2\text{H}$ -values in both laboratories. The amount for F_{crit} is looked up in the Fisher table respectively F-distribution, for $\alpha = 0.05$.

Location	Source of Variation*	Degree of freedom	Variances	F	F_{crit}
La Calcara (1)	S_{Lab}^2	1	59.525	663.15	18.51
	S_{R}^2	2	0.090		
P21 (1)	S_{Lab}^2	1	71.663	4406.53	18.51
	S_{R}^2	2	0.016		
BP (MS)	S_{Lab}^2	1	92.507	3053.86	18.51
	S_{R}^2	2	0.030		
Area26N	S_{Lab}^2	1	76.108	1112.94	18.51
	S_{R}^2	2	0.068		
HL	S_{Lab}^2	1	56.267	2244.80	18.51
	S_{R}^2	2	0.025		
La Calcara (2)	S_{Lab}^2	1	66.105	3977.49	18.51
	S_{R}^2	2	0.017		
FumF	S_{Lab}^2	1	63.520	853.18	18.51
	S_{R}^2	1	0.074		
BP	S_{Lab}^2	1	111.399	5315.74	18.51
	S_{R}^2	2	0.0210		
Area26	S_{Lab}^2	1	169.778	12211.01	18.51
	S_{R}^2	2	0.014		
P21 (2)	S_{Lab}^2	1	84.847	24636.76	18.51
	S_{R}^2	2	0.003		
BN	S_{Lab}^2	1	77.870	2416.49	18.51
	S_{R}^2	2	0.032		

* S_{Lab}^2 = Between the laboratories
 S_{R}^2 = Within the laboratories

Table A 14: All water samples from 2008, 2009 and 2010 which were measured at the INGV and UFZ for $\delta^{13}\text{C}_{\text{DIC}}$.

Location samples	$\delta^{13}\text{C}_{\text{DIC}}$ [‰] VPDB	Mean $\delta^{13}\text{C}_{\text{DIC}}$ [‰] VPDB	Standard deviation
BP-150508-W1	7.9		
BP-030908-W2	0		
BP-280808-W1	1.3		
BP-030809-EX	0.8		
BP(N)-060908-W3	1.1		
BP-150508	-17.65	-1.0	9.0
BP-030909	-7.3		
BP-050909	-6.8		
BP2-060909	15.0		
BP-050910	-8.4		
BP-050910(II)	-6.7		
BP-050910CM	9.0		
P21-140508-W1	9.1		
P21-150508-W2	8.3		
P21-290808-W1	2.1		
P21-150508	-1.58		
P21-050909	14.9	8.2	8.2
P21-020910	17.6		
P21-020910(II)	17.4		
P21-050910	-5.1		
P21-070910CM	11.4		
HL-160508-W1	0.8		
HL-070908-W3(80cm)	0.7		
HL310808-W2(2m)	1.5		
HL080908-W4(80cm)	4.8		
HL310808-W1(1cm)	1.2		
HL-160508	-1.85		
HL-060909	-5.7	2.8	8.6
HL-110909(3m)	-8,6		
HL-120909(3m)	-7,5		
HL-040910(3m)	6.6		
FumF-100909	-5.6		
FumF-040910CM	-5.9		
FumF-080910	15.1		
HL-080910(3m)	22.5		
BN-150508-W1	11.5		
BN-310808-W1	1.4		
BN-150508	0.31	5.3	8.8
BN-090909	19.4		
BN-070910	17.5		
BN-070910CM	19.5		
Area26-080908-W2b	4.2		
Area26-080908-W2a	4.3		
Area26-100909	-5.8		
Area26-060910	15.8	4.5	10.5
Area26-060910	9.1		
Area26N-070910	16.0		
Area26-060910CM	-12.1		

Table A 14: All water samples from 2008, 2009 and 2010 which were measured at the INGV (highlighted samples) an UFZ for $\delta^{13}\text{C}_{\text{DIC}}$ (continuation).

Location samples	$\delta^{13}\text{C}_{\text{DIC}}$ [‰] VPDB	Mean $\delta^{13}\text{C}_{\text{DIC}}$ [‰] VPDB	Standard deviation
BW(LB)-060908-Ref	0.3		
BW-040908-W1	0.9	4.8	6.1
BW-130508	4.3		
BW-060910	13.6		
LaCalcara-020910	13.0	15.1	2.9
LaCalcara-120910	17.1		

Table A 15: (D/O)-measurements at the INGV and UFZ arranged between 2007 and 2011.

sample ID	UFZ		INGV	
	$\delta^{18}\text{O}_{\text{VSMOW}}$ [‰]	$\delta^2\text{H}_{\text{VSMOW}}$ [‰]	$\delta^{18}\text{O}_{\text{VSMOW}}$ [‰]	$\delta^2\text{H}_{\text{VSMOW}}$ [‰]
PAN-060908-BW(LB)-Ref	1.6	12.7		
PAN-040908-BW-W1	1.8	11.3		
PAN-090907-B(W)-P3			0.7	7.7
PAN-130508-BW-W1			0.8	5.6
PAN-150508-B(N)-W1	0.6	2.4	0.5	4
PAN-310808-B(N)-W1	-1.2	-11.4		
PAN-060907-P21-P2(w)			1.2	9.3
PAN-140508-P21-W1			0.6	5
PAN-150508-P21-W2	0.7	2.4	0.7	5.1
PAN-290808-P21-W1	1.1	1.9		
PAN-060908-BP(N)-W3	1.2	9.9		
PAN-060907-BP-P2			1.1	8.1
PAN-070907-BP-P3			1.4	7.9
PAN-280808-BP-W1	2.6	5.7		
PAN-150508-BP-W1	1.9	2.5	1.4	2.4
PAN-080908-Area 26-W2	1.5	-0.8		
PAN-160508-HL-W1	1.2	1.2	0.4	-2.2
PAN-070907-HL-P2-(w)			0.4	-4.5
PAN-310808-HL-W1 (1m)	0.8	-4.7		
PAN-310808-HL-W2 (2m)	0.6	-7.9		
PAN-BP-030909	2.2	3.6		
PAN-P21-050909	1.3	8.4		
PAN-BP-050909	2.3	4.1		
PAN-HL-060909	0.9	-3.4		
PAN-BP2-060909	1.0	7.8		
PAN-B(N)-090909	0.9	6.7		
PAN-Fum-100909	0.4	3.1		
PAN-Area26-100909	0.9	7.7		
PAN-HL-110909(3m)	0.8	-7.2		
PAN-HL-120909(3m)	0.9	-7.6		
PAN-P21-020910	1.2	7.5		
PAN-P21-020910(II)	1.1	6.8		
PAN-LaCalcara-020910	3.0	8.9	2.68	0
PAN-HL-040910(3m)	0.9	-5.4		

Table A 15: (D/O)-measurements at the INGV and UFZ arranged between 2007 and 2011 (continuation).

sample ID	UFZ		INGV	
	$\delta^{18}\text{O}_{\text{VSMOW}}$ [‰]	$\delta^2\text{H}_{\text{VSMOW}}$ [‰]	$\delta^{18}\text{O}_{\text{VSMOW}}$ [‰]	$\delta^2\text{H}_{\text{VSMOW}}$ [‰]
PAN-P21-050910	1.2	7.8	0.63	-2
PAN-BP-050910MS	2.6	4.1	1.48	-7
PAN-BP-050910(II)MS	2.6			
PAN-Area26-060910	0.9			
PAN-Area26-060910	1.1			
PAN-B(W)-060910	1.0			
PAN-Area26N-070910	0.9	0.79	-3	
PAN-B(N)-070910	0.9			
PAN-HL(FUM)-080910	0.5			
PAN-HL-080910(3m)	1.0	0.37	-14	
PAN-LaCalcara-120910	2.8	3.11	0	
MS				
PAN-FumF-040910CM	0.5	-0.04	-8	
PAN-BP-050910CM	1.7	1.06	-3	
PAN-Area26-060910CM	1.4	0.47	-7	
PAN-P21-070910CM	1.4	0.63	-2	
PAN-BN-070910CM	1.2	1.05	-2	

Table A 16: Calculated 3-componenten-mixture-system for measured (O/D)-values at the UFZ including Mediterranean water, magmatic water and local meteoric water. Results are arranged in diving spots.

Location	UFZ		Medi	Magmatic	Meteor
	$\delta^{18}\text{O}_{\text{VSMOW}}$ [‰]	$\delta^2\text{H}_{\text{VSMOW}}$ [‰]	in [%]	in [%]	in [%]
PAN-150508-B(N)-W1	0.6	2.4	68.5	11.5	20.1
PAN-310808-B(N)-W1	-1.2	-11.4	23.8	17.6	58.6
PAN-B(N)-070910	0.9	6.4	84.1	6.5	9.4
PAN-BN-070910CM	1.2	8.2	89.3	6.5	4.2
PAN-B(N)-090909	0.9	6.7	85.8	5.5	8.7
PAN-150508-P21-W2	0.7	2.4	67.3	12.8	19.9
PAN-290808-P21-W1	1.1	1.9	60.2	19.4	20.4
PAN-P21-050909	1.3	8.4	88.7	7.7	3.6
PAN-P21-050910	1.2	7.8	87.1	7.6	5.3
PAN-P21-020910	1.2	7.5	85.8	8.1	6.0
PAN-P21-070910CM	1.4	8.6	89.0	8.3	2.7
PAN-P21-020910(II)	1.1	6.8	83.9	8.0	8.1
PAN-280808-BP-W1	2.6	5.7	60.8	31.4	7.8
PAN-150508-BP-W1	1.9	2.5	53.7	29.0	17.3
PAN-BP-030909	2.2	3.6	56.0	30.1	13.9
PAN-BP-050909	2.3	4.1	56.6	31.1	12.3
PAN-BP-050909	1.0	7.8	90.2	4.2	5.6
PAN-BP-050910MS	2.6	4.1	52.9	35.3	11.8
PAN-BP-050910(II)MS	2.6	4.4	54.3	34.5	11.1
PAN-BP-050910CM	1.7	9.2	88.3	10.9	0.8
PAN-160508-HL-W1	1.2	1.2	55.7	22.3	22.0
PAN-310808-HL-W1 (1m)	0.8	-4.7	32.3	30.0	37.7
PAN-310808-HL-W2 (2m)	0.6	-7.9	19.4	34.4	46.2
PAN-HL-110909(3m)	0.8	-7.2	20.0	36.1	43.9
PAN-HL-120909(3m)	0.9	-7.6	17.8	37.4	44.8
PAN-HL-080910(3m)	1.0	-5.3	26.4	34.7	38.9
PAN-HL-040910(3m)	0.9	-5.4	27.3	33.4	39.2
PAN-HL-060909	0.9	-3.4	37.4	28.2	34.4
PAN-HL(FUM)-080910	0.5	2.4	70.3	9.4	20.2
PAN-FumF-040910CM	0.5	1.8	66.9	11.2	21.9
PAN-Fum-100909	0.4	3.1	74.3	7.0	18.7
PAN-080908-Area 26-W2a	1.5	-0.8	42.7	30.9	26.4
PAN-Area26-100909	0.9	7.7	90.0	3.9	6.1
PAN-Area26-060910	0.9	7.8	90.3	3.9	5.7
PAN-Area26-060910	1.1	7.3	86.4	6.8	6.8
PAN-Area26-060910CM	1.4	8.0	86.0	9.8	4.2
PAN-Area26N-070910	0.9	7.1	87.7	4.7	7.7
PAN-B(W)-060910	1.0	8.4	92.7	3.3	4.0
PAN-060908-BW(LB)-Ref	1.6	12.7	105.8	2.2	8.0
PAN-040908-BW-W1	1.8	11.3	96.8	8.0	4.9
PAN-LaCalcara-020910	3.0	8.9	71.3	29.8	1.1
PAN-LaCalcara-120910 MS	2.8	9.4	76.0	25.9	2.0

Table A 17: Calculated 3-componenten-mixture-system for measured (O/D)-values at the INGV including Mediterranean water, magmatic water and local meteoric water. Results are arranged in diving spots.

Location	INGV		Medi.	Magmatic	Meteor
	$\delta^{18}\text{O}_{\text{VSMOW}} [\text{‰}]$	$\delta^2\text{H}_{\text{VSMOW}} [\text{‰}]$	in [%]	in [%]	in [%]
PAN-090907-B(W)-P3	0.7	7.7	92.6	1.0	6.4
PAN-130508-BW-W1	0.8	5.6	81.4	7.1	11.6
PAN-150508-B(N)-W1	0.5	4	77.3	6.5	16.2
PAN-BN-070910CM	1.05	-2	42.2	27.4	30.4
PAN-060907-P21-P2(w)	1.2	9.3	94.3	4.3	1.4
PAN-140508-P21-W1	0.6	5	80.9	5.7	13.5
PAN-150508-P21-W2	0.7	5.1	80.2	6.8	13.0
PAN-P21-050910	0.63	-2	47.1	21.7	31.2
PAN-P21-070910CM	0.63	-2	47.1	21.7	31.2
PAN-060907-BP-P2	1.1	8.1	89.8	5.6	4.6
PAN-070907-BP-P3	1.4	7.9	85.3	10.1	4.6
PAN-150508-BP-W1	1.4	2.4	59.1	22.4	18.5
PAN-BP-050910MS	1.48	-7	13.4	44.4	42.2
PAN-BP-050910CM	1.06	-3	37.3	29.8	32.9
PAN-160508-HL-W1	0.4	-2.2	48.9	19.0	32.1
PAN-070907-HL-P2-(w)	0.4	-4.5	37.9	24.1	38.0
PAN-FumF-040910CM	-0.04	-8	26.4	25.9	47.7
PAN-LaCalcara-020910	2.68	9	76.5	24.1	0.6
PAN-LaCalcara-120910 MS	3.11	9	70.6	30.9	1.6
PAN-Area26N-070910	0.79	-3	40.5	26.1	33.4
PAN-Area26-060910CM	0.47	-7	25.2	30.6	44.2

Table A 18: Results of the $\delta^{34}\text{S}$ determination of water (highlighted blue), gas (highlighted yellow) and bio samples (highlighted brown) measured at the UFZ in 2011.

Location	$\delta^{34}\text{S} / \text{SO}_4$ [‰] VCDT	$\delta^{18}\text{O} / \text{SO}_4$ [‰] VSMOW	$\delta^{34}\text{S} / \text{S}^{2-}$ [‰] VCDT	S / elemental S [‰]	STDEV	Method
PAN-BP-050909	21.2	7.9	2.6			AVS
PAN-HL-060909	20.7	9.6	2.3			AVS
PAN-BP2-060909	21.2	9.7	3.6			AVS
PAN-B(N)-090909	22.5	11.1	0.6			AVS
PAN-Fum-100909	22.7	9.6	1.2			AVS
PAN-HL-120909(3m)	22.4	11.1	3.1			AVS
PAN-P21-020910	21.0	8.5	-0.4			AVS
PAN-HL-040910(3m)	21.1	10.4	1.8			AVS
PAN-P21-050910	21.7	11.1	-0.8			AVS
PAN-BP-050910	22.8	10.5	-			AVS
PAN-Area26-060910	21.1	10.5	-0.3			AVS
PAN-B(W)-060910	22.2	8.5	3.0			AVS
PAN-Area26N-070910	23.0	12.2	-2.4			AVS
PAN-B(N)-070910	22.5	11.1	-0.7			AVS
PAN-HL(FUM)-080910	21.9	9.2	1.5			AVS
PAN-HL-080910(3m)	22.2	10.5	2.0			AVS
PAN-LaCalcara- 120910	20.1	8.7	-			AVS
PAN-P21-030909	no sample	no sample	1.5			AVS
PAN-P21-050909	no sample	no sample	-1.0			AVS
PAN-BP-060909	no sample	no sample	4.3			AVS
PAN-B(N)-090909	no sample	no sample	4.8			AVS
PAN-Fum-100909	no sample	no sample	1.5			AVS
PAN-Area26-120909	no sample	no sample	1.8			AVS
PAN-Area26- 14092010	no sample	no sample	-1.1			AVS
PAN-B(N)-07092010	no sample	no sample	0.5			AVS
PAN-B(W)-060910	no sample	no sample	2.3			AVS
PAN-BP-050910	no sample	no sample	3.7			AVS
PAN-P21-050910	no sample	no sample	-0.5			AVS
PAN-HL(FUM)-080910	no sample	no sample	1.8			AVS
PAN-LaCalcara- 120910	no sample	no sample	0.7			AVS
elemental sulphur	-	-	-3.3	-4.1	0.1	CRS
PAN-P21- 08092010_BIO	-	-	-3.6	-1.1	0.2	CRS
PAN-P21- 08092010_BIO2	-	-	-2.4	-0.9	0.1	CRS

Table A 19: Results of the $\delta^{34}\text{S}$ determination of water (highlighted blue) and gas (highlighted yellow) Samples from 2006 and 2007, measured at the UFZ.

Location	$\delta^{34}\text{S} / \text{S}^{2-}$ [‰] VCDT	$\delta^{34}\text{S} / \text{SO}_4$ [‰] VCDT
BP_050507	-	20.50
HL_040507	3.30	22.70
HL_030907	1.96	22.60
BN_030907	0.95	22.50
P21_060907	0.80	21.30
HL_070907	2.52	22.40
BW_080907	2.35	
P21_090906	0.48	
P21_090906	0.01	
P21_100906	-0.21	
P21_100906	1.78	
HL-FumF_070906	2.34	
BN_060906	1.03	
BW_310807	-	
BN_040907	1.49	
BP_060907	4.28	

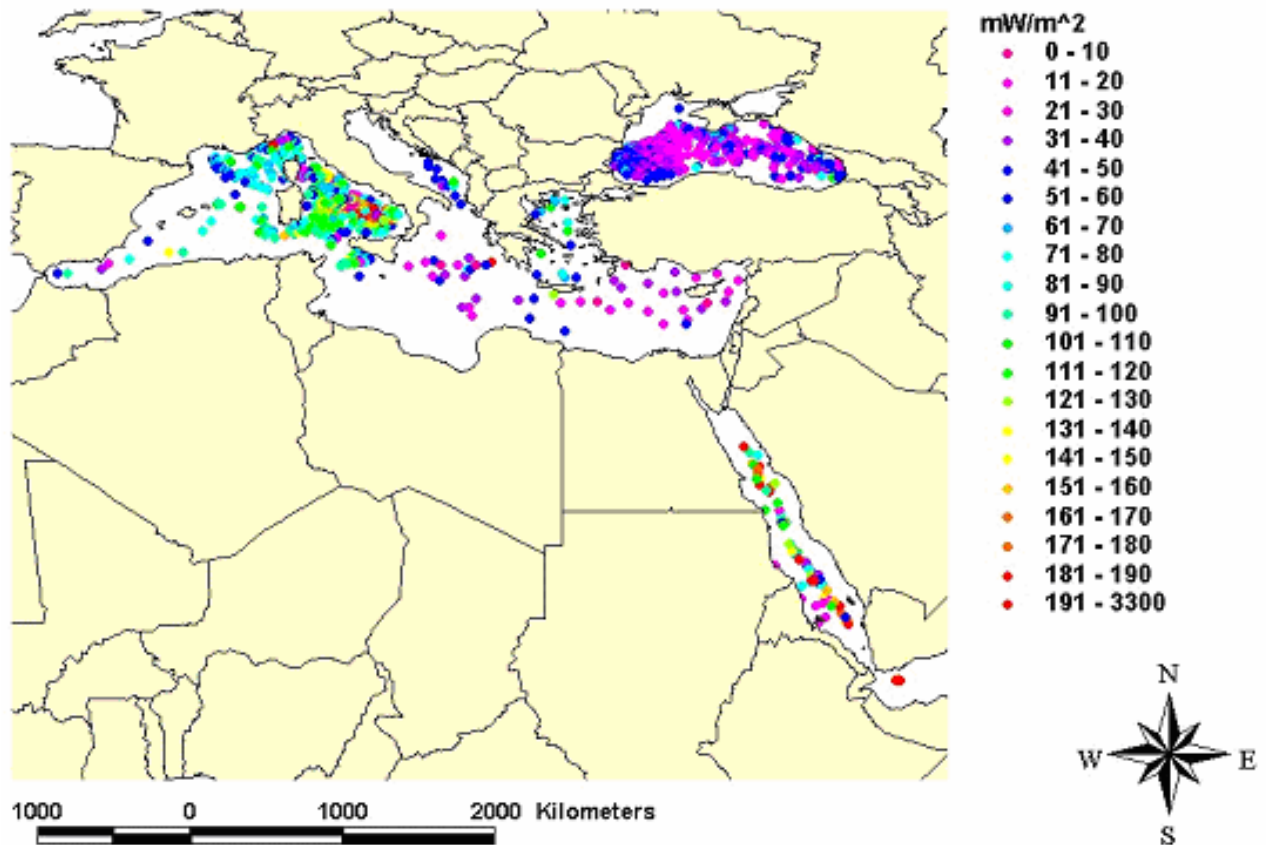


Figure B 1: Map showing the known heat flows in the Mediterranean, Black and Red Seas published from the International Heat Flow Commission (IHFC), University of North Dakota. Data are presented in a colour coded format using the visible light spectrum so that warm colours (reds) indicate high heat flow and cool colours (violet) indicate low heat flow. The spectral range for each data map is 0 to 200 mW/m^2 in intervals of 10 mW/m^2 . Heat flow greater than 200 mW/m^2 are assigned the warmest colour.

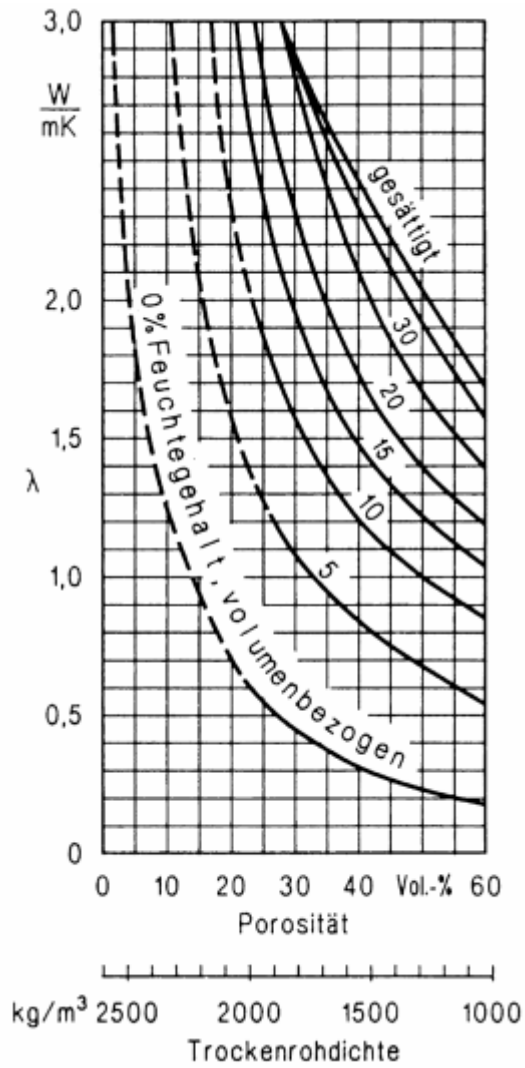


Figure B 2: Thermal conductivity in quartz sand for different porosities and different water contents (research after Krischer, 1934).

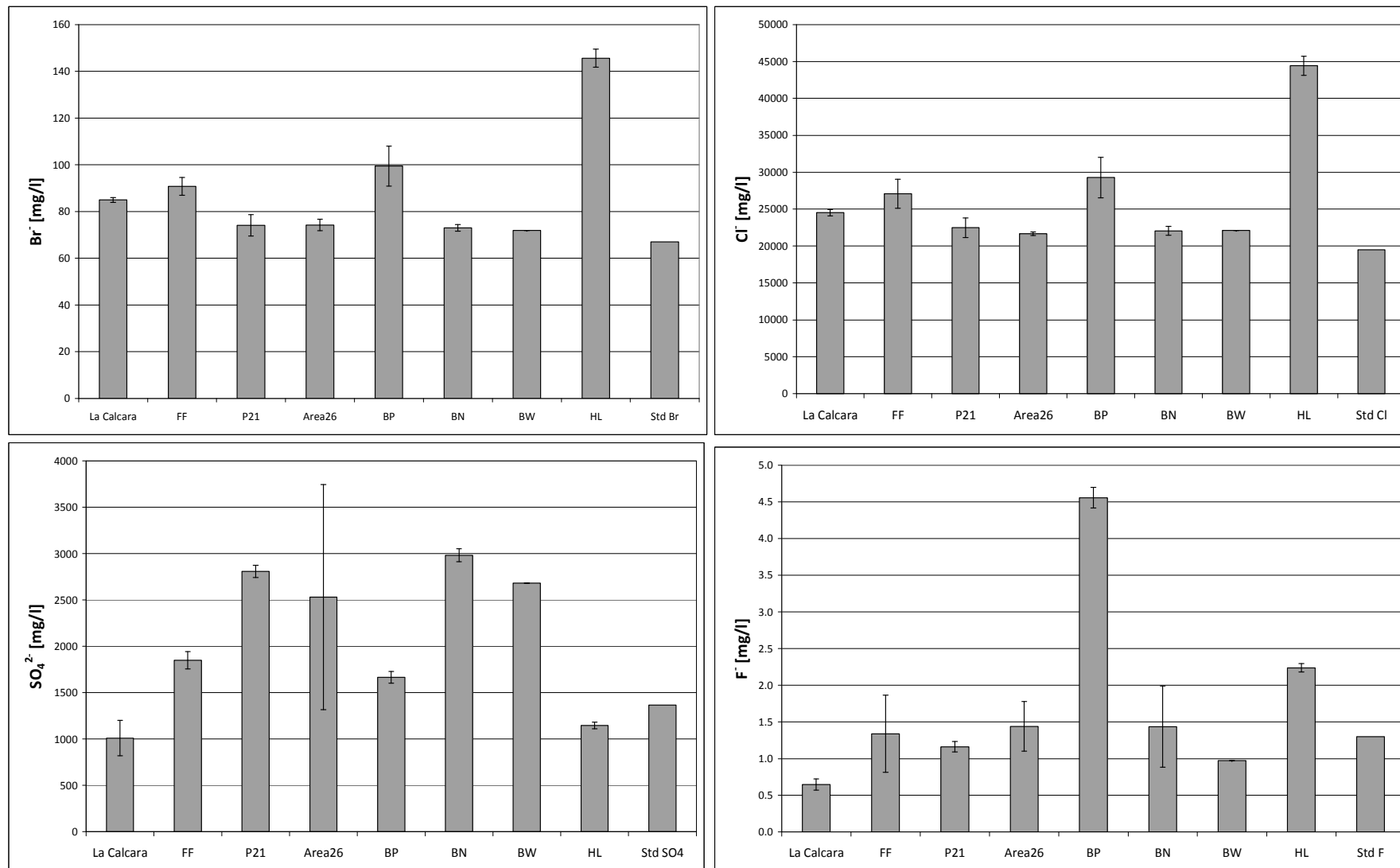


Figure B 3: Separately illustration of the anions Br⁻, Cl⁻, SO₄²⁻ and F⁻ for each diving location. The calculated mean values and corresponding standard diversity are displayed. The content of normal seawater after Brown et al. (1995) are shown for a better comparison.

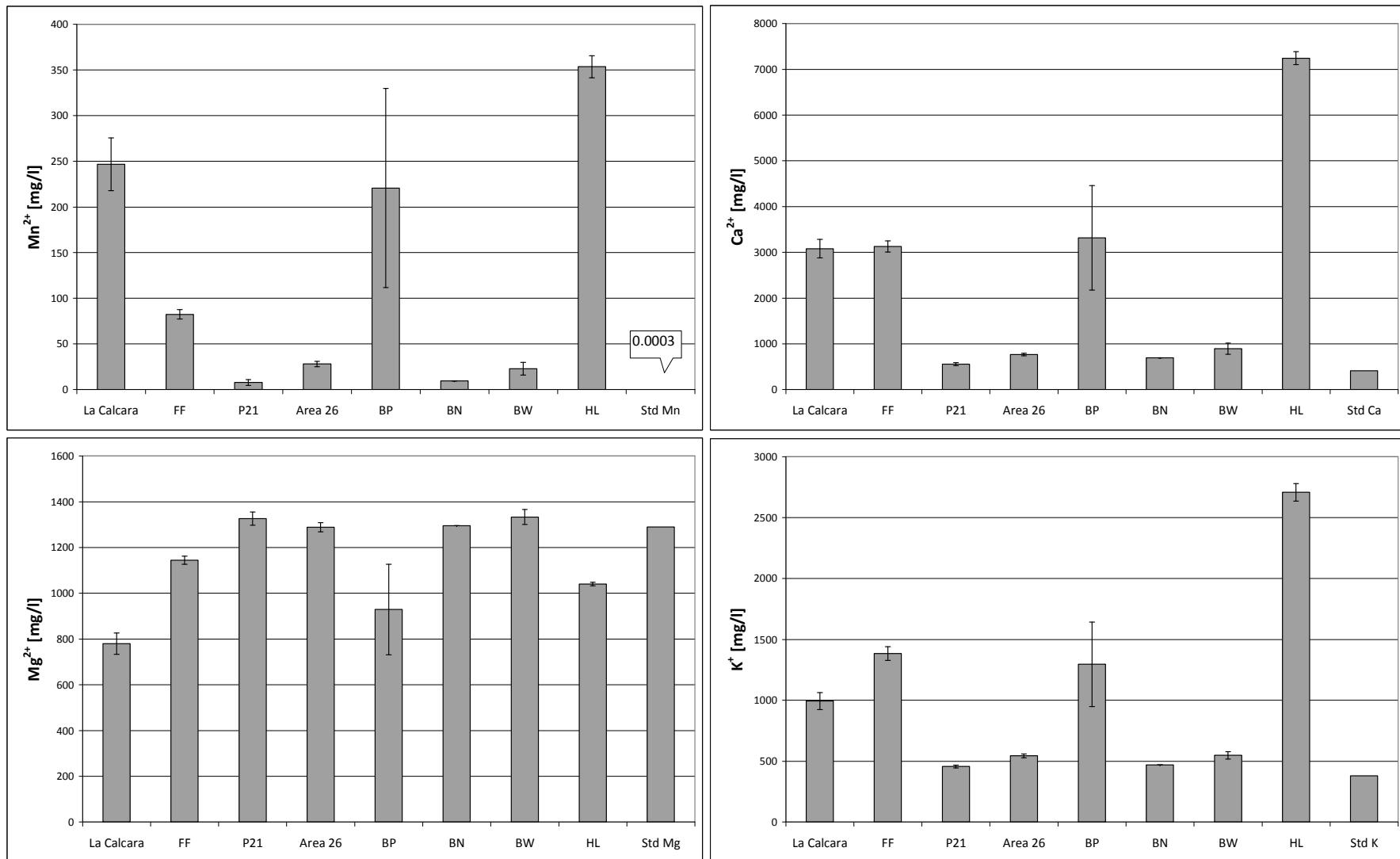


Figure B 4: Separately illustration of the cations Mn²⁺, Ca²⁺, Mg²⁺, K⁺ for each diving location. The calculated mean values and corresponding standard diversity are displayed. The content of normal seawater after Brown et al. (1995) are shown for a better comparison.

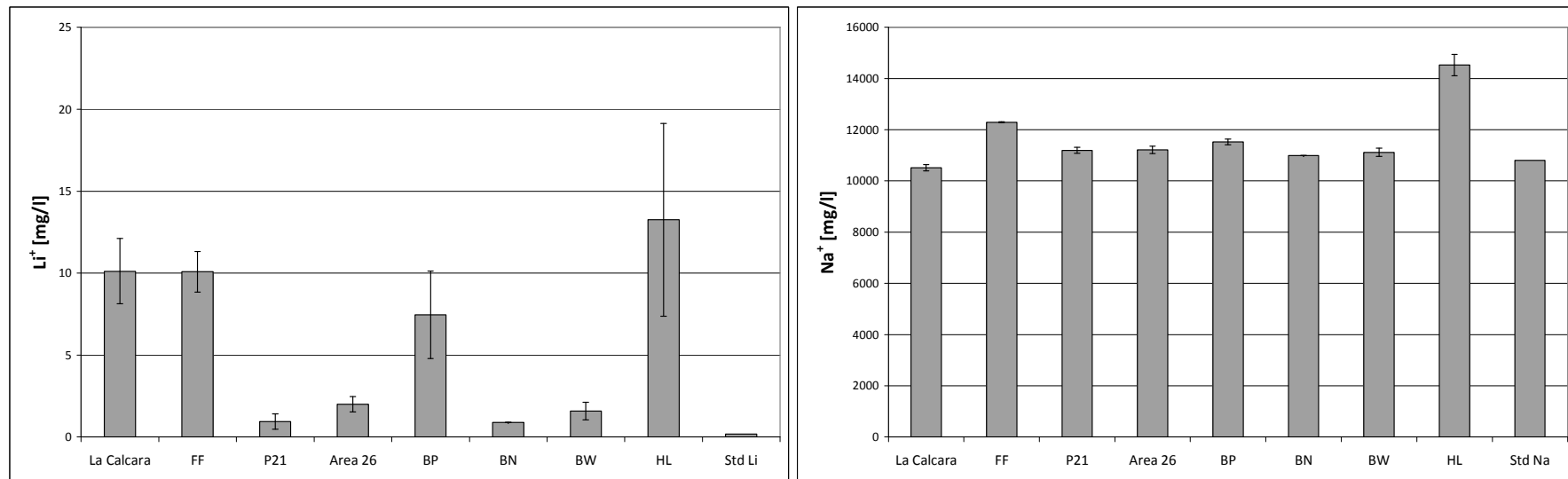


Figure B 4: Continuation: Separately illustration of the cations Na⁺ and Li⁺ for each diving location. The calculated mean values and corresponding standard diversity are displayed. The content of normal seawater after Brown et al. (1995) are shown for a better comparison.